

## ABSTRACT

Title of Dissertation: KINETICS OF THERMAL AGING AND THE ASSOCIATED EMBRITTLEMENT OF CAST DUPLEX STAINLESS STEELS

Sarah Mburu, Doctor of Philosophy, 2018

Dissertation directed by: Professor Sreeramamurthy Ankem  
Department of Materials Science and Engineering

Cast Duplex Stainless Steels (CDSS) have been extensively used as structural components in light water reactor (LWR) power plants as primary coolant pipes and pump casings. These large components are in persistently extreme and damaging environments, including high temperature, high pressure, corrosive exposure, and low dose radiation for extended periods of time. This work focuses on the thermal embrittlement of CDSS that leads to poor mechanical properties and is a concern in the extended-term operation of nuclear power plants. Many past studies have concluded that the miscibility gap in the Fe-Cr phase diagram leads to spinodal decomposition, which is the primary source for thermal embrittlement of the  $\delta$ -ferrite phase in CDSS. The hardening caused by spinodal decomposition hinders plastic deformation and thus leads to brittle fracture. In this work, mechanical testing and microstructural characterization, mainly by Atom Probe Tomography (APT), were performed on short-term (up to 2 years) thermally aged CDSS at accelerated

temperatures to understand the embrittlement process and mechanisms of thermal-aging degradation. Two CDSS materials, CF-3 and CF-8, were thermally aged for 4300 hours (h), 8600 h, 12900 h, and 17200 h at 280 °C, 320 °C, 360 °C, and 400 °C. Both alloys exhibited an increase in hardness and associated reduction in impact energy with increased aging time across all temperatures. The unparalleled insight of the APT technique provided a high resolution analysis of 3-D distributions of atoms to experimentally characterize the morphology of phase separation. It allowed for the analysis of  $M_{23}C_6$  carbides and nanostructured clusters, including the spinodal decomposition of the  $\delta$ -ferrite into networked  $\alpha/\alpha'$  domains and precipitation of G-phase at the  $\alpha/\alpha'$  domain interface. These transformations are shown to be highly dependent on the initial composition and aging temperature. From the wavelength (size) and amplitude (composition fluctuation) measurements, we successfully calculated the activation energies and inferred the progression of dominating diffusion mechanism during spinodal decomposition and G-phase precipitation. This data may potentially be used to predict the reliability of LWR components after many years of service.

KINETICS OF THERMAL AGING AND THE ASSOCIATED EMBRITTLEMENT  
OF CAST DUPLEX STAINLESS STEELS

By

Sarah Mburu

Dissertation submitted to the Faculty of the Graduate School of the  
University of Maryland, College Park, in partial fulfillment  
of the requirements for the degree of  
Doctor of Philosophy  
2018

Advisory Committee:

Professor Sreeramamurthy Ankem, Chair

Professor Abhijit Dasgupta, Dean's Representative

Professor Mohamad Al-Sheikhly

Professor Aristos Christou

Professor Lourdes Salamanca-Riba

© Copyright by  
Sarah Mburu  
2018

## Preface

The present doctoral thesis summarizes the work I have done during my 4.5 years of study as a Ph.D. student in the Department of Materials Science and Engineering at the University of Maryland, College Park. This work was supported by the Department of Energy – Nuclear Energy University Program (DOE-NEUP), Contract no. DE-NE0000724. The Pacific Northwest National Laboratory provided the equipment necessary to conduct the experiments.

Key findings:

- Developed a new method to measure the total diffusion by taking both the increase in size and concentration changes into account
- Measured the activation energy of diffusion and directly correlated it to the diffusion mechanism
- Analyzed the influence of carbide on spinodal decomposition and G-phase precipitation

## Dedication

This dissertation is dedicated to my parents and elementary school teachers. Twenty years ago, they foretold that it will be completed one day.

## Acknowledgements

I express sincere gratitude to my thesis advisor, Prof. Ankem for his support and guidance. I extend my gratitude to Dr. Daniel Perea, from the Pacific Northwest National Laboratory, who sacrificed so much of his time to help me learn how to operate the Focused Ion Beam and Atom Probe Tomography. I acknowledge the support of lab members, namely, Dr. Kolli, Mr. Schwarm, Mr. Draper, Mr. Fritchl, Ms. Tsao, Mr. Patel, and Ms. Fansi in carrying out experiments and discussing the results.

Thanks to my entire family around the world for their unwavering support, especially my parents and siblings, Liz and Ben.

I appreciate the sense of community provided by the programs, members and leaders in PROMISE AGEP, the Center of Minorities in Science and Engineering, and SLOAN PEM writing session.

# Table of Contents

Preface.....	ii
Dedication.....	iii
Acknowledgements.....	iv
Table of Contents.....	v
List of Tables.....	viii
List of Figures.....	ix
List of Abbreviations.....	xiii
Chapter 1: Introduction.....	1
Chapter 2: Background.....	7
2.1 Steel Fabrication.....	7
2.1.1 Processing Route.....	7
2.1.2 Composition.....	8
2.2 Phases.....	9
2.2.1 Austenite and Ferrite phases.....	12
2.2.2 Fe-rich phase ( $\alpha$ ) and Cr-rich phase ( $\alpha'$ ).....	13
2.2.3 G-phase.....	14
2.2.4 $\epsilon$ (Cu) Phase.....	15
2.2.5 R Phase.....	15
2.2.6 Chi ( $\chi$ ) Phase.....	16
2.2.7 Sigma ( $\sigma$ ) Phase.....	16
2.2.8 Laves ( $\eta$ ) Phase.....	16
2.2.9 $\text{Cr}_2\text{N}$ and $\pi$ Phase.....	17
2.2.10 Carbides.....	17
2.3 Thermodynamics and Kinetics of Phase Transformations.....	18
2.3.1 Theory of Phase Separation.....	21
2.3.2 Nucleation, Growth, and Coarsening.....	22
2.4 Literature Review.....	27
2.4.1 Groundbreaking work.....	27
2.4.2 Analyzing Kinetics – time exponents.....	29
2.4.3 Analyzing Kinetics – change in mechanical properties.....	31
2.4.4 Relating Microstructural Changes to Mechanical Properties.....	32
2.4.5 Non-uniform kinetics.....	35
Chapter 3: Experimental Procedures.....	37
3.1 Mechanical Properties.....	38
3.1.1 Vickers Micro-Hardness (HV).....	38
3.1.2 Charpy V-notch Impact Toughness (CVN).....	39
3.2 Characterization Techniques.....	39
3.2.1 Optical Microscopy.....	41
3.2.2 Scanning Electron Microscope (SEM).....	42
3.2.3 Scanning/Transmission Electron Microscope (S/TEM).....	44
3.2.4 Atom Probe Tomography (APT).....	45
Chapter 4: Analytical Procedures.....	51

4.1 Spinodal Decomposition.....	51
4.1.1 Auto-Correlation Function Method (ACF).....	51
4.1.2 Larson-Bar-on-Miller Method (LBM).....	52
4.1.3 In-Lab Method by Sinusoidal Curves.....	54
4.2 G-phase.....	56
3.2.1 Radius ( $\langle R \rangle$ ).....	56
3.2.2 Number Density ( $N_v$ ).....	57
3.2.3 Volume Percentage ( $V_p$ ).....	57
4.3 Kinetic Analysis.....	57
4.3.1 Time Exponents ( $n$ ).....	57
4.3.2 Degree of Decomposition (D.o.D).....	57
4.3.3 Activation Energy.....	58
4.4 Fitting Functions.....	59
Chapter 5: Experimental Data – Results and Discussion.....	60
5.1 Mechanical Properties.....	60
5.1.1 Vickers Microhardness (HV).....	60
5.1.2 Charpy V-notch Impact Toughness (CVN).....	62
5.2 Optical Microscopy.....	66
5.2.1 Volume Fractions.....	66
5.3 Scanning Electron Microscopy (SEM).....	68
5.3.1 Elemental Partitioning.....	68
5.4 Atom Probe Tomography (APT).....	69
5.4.1 Elemental Partitioning Across the Heterophase Interface.....	69
5.4.2 Spinodal Decomposition and G-phase Formation in Ferrite Phase.....	72
5.4.3 Elemental Segregation to the Heterophase Interface.....	74
5.4.4 Carbides and Other Heterophase Precipitates.....	76
Chapter 6: Phase Separation Kinetics – Results and Discussion.....	84
6.1 Spinodal Decomposition.....	84
6.1.1 Composition Fluctuation.....	84
6.1.2 Wavelength and Amplitude.....	87
6.2 G-phase Forming Zones.....	91
6.2.1 Composition.....	91
6.2.2 Radius ( $\langle R \rangle$ ), Number Density ( $N_v$ ), and Volume Percentage ( $V_p$ ).....	95
6.3 Time Exponents.....	99
6.3.1 Spinodal Decomposition.....	99
6.3.2 G-phase Forming Zones.....	100
6.4 Degree of Decomposition (D.o.D).....	101
6.4.1 Spinodal Decomposition.....	101
6.4.2 G-phase Forming Zones.....	101
6.5 Activation Energy.....	102
6.5.1 Spinodal Decomposition.....	102
6.5.2 G-phase Forming Zones.....	106
6.5.3 Validity of Accelerated Temperatures.....	114
6.6 Predicting D.o.D.....	114
6.6.1 Spinodal Decomposition.....	114
6.6.2 G-phase Forming Zones.....	116

6.7 Influence of Carbide .....	118
6.7.1 Spinodal Decomposition.....	118
6.7.2 G-phase Forming Zones .....	121
Chapter 7: Conclusions.....	125
Chapter 8: Suggestions for future work .....	130
Appendices.....	132
Bibliography .....	136

## List of Tables

- Table 1.** Activation energy of metallic species in Fe lattice. Reported from Smithels Metals Reference Book [39].
- Table 2.** Composition of CF-3 and CF-8 alloys
- Table 3.** Ferrite volume fraction measurements by manual point counting, digital counting and Shofer diagram.
- Table 4.** Time exponents of wavelengths and amplitudes by in-lab, ACF, and LBM methods.
- Table 5.** Time exponents of G-phase radius, number density, and volume percent

## List of Figures

- Figure 1.** (a) Fe-Cr phase diagram, (b) Regions of miscibility gap. Adapted from [34].
- Figure 2.** Free Energy diagrams at (a) high and (b) low temperatures indicated in Figure 1. Adapted from [34].
- Figure 3.** (a) Chemical potential of spinodal decomposition; (b) schematic of uphill diffusion. Adapted from [34].
- Figure 4.** Homogenous nucleation. Adapted from [34].
- Figure 5.** The change in size, number density, and volume fraction at different growth regimes
- Figure 6.** Flux of elements in spinodal decomposition domains and G-phase precipitates
- Figure 7.** (a) Diffusion paths in steel; (b) Plot of diffusion as a function of inverse temperature illustrating the slope of the dominating diffusion mechanism with solid lines while contributing factors are in dashed lines. Adapted from [34].
- Figure 8.** Transition of ductile to brittle fracture mode due to thermal aging. Adapted from [77].
- Figure 9.** (a) Time of flight mass spectrometry, (b) ranging of mass spectra. Adapted from [81].
- Figure 10.** *In situ* site-specific specimen preparation technique on the Focused Ion Beam (FIB): (a) After milling, extracted sample with an omniprobe; (b) Attached sample on a post; (c) sharpened sample to sub-100 nm tip.
- Figure 11.** Fe, Cr, and Ni Isoconcentration surfaces to illustrate respective phases.
- Figure 12.** Generating proximity histogram plot from: (a) particles with an isoconcentration delineated by the black circular surface, and (b) interface delineated by the black linear surface
- Figure 13.** 20 ROI's in the ferrite phase (a) top view, (b) side view).
- Figure 14.** Auto-Correlation Function method illustrating how the wavelength is derived from the plot. The plots are derived from CF-3 samples aged at 400 °C to (a) 4300 hours, (b) 8600 h, (c) 12900 h, and (d) 17200 h
- Figure 15.** Langer-Bar-on-Miller (LBM) method illustrating how the amplitude is derived from the plot. The plots are derived from CF-8 samples aged to 17200 hours at (a) 280 °C, (b) 320 °C, (c) 360 °C, and (d) 400 °C
- Figure 16.** (a) APT reconstruction of one ROI that aligns to the Fe, Cr, and Ni curves in (b); (b) Illustrating the in-lab method of simultaneously measuring the spinodal decomposition amplitude and wavelength of sinusoidal waves
- Figure 17.** Demonstrating the concept of Degree of Decomposition (D.o.D) by showing that (a) the wavelength and (b) the amplitude of CF-3 samples are both increasing during thermal aging. (c) An illustration of the spinodal decomposition domain drawn as a cube, where the wavelength is length of the domain and the amplitude is the Cr concentration in the domain.
- Figure 18.** Vickers microhardness (HV) data from all (a) CF-3 and (b) CF-8 samples
- Figure 19.** Normalized HV data to the unaged value showing percent change in HV data for (a) CF-3 samples, (b) CF-8 samples, and (c) ratio of CF-3 to CF-8
- Figure 20.** Charpy impact toughness data from all (a) CF-3 and (b) CF-8 samples

- Figure 21.** Normalized CVN data to the unaged value showing percent change in CVN data for (a) CF-3 samples, (b) CF-8 samples, and (c) ratio of CF-3 to CF-8
- Figure 22.** Fractography of Charpy specimen: (a) Unaged CF-3 and (b) CF-3 sample aged to 4300 h at 400 °C
- Figure 23.** Optical Micrograph of representative CF-3 alloy.
- Figure 24.** SEM-EDS (a) Spectra, and (b) Elemental mapping for the ferrite and austenite phases in the unaged CF-8 sample
- Figure 25.** (a) APT reconstructions and (b) proxigram of unaged CF-3
- Figure 26.** (a) APT reconstructions and (b) proxigram of unaged CF-8
- Figure 27.** APT elemental mapping of (a) CF-3 and (b) CF-8 steels aged for 8600 h at 400 °C
- Figure 28.** APT elemental mapping of (a) CF-3 and (b) CF-8 steels aged for 17200 h at 400 °C
- Figure 29.** (a) SEM image and (b) APT reconstruction of unaged CF-8 sample with carbide. (c) The 1-D composition profile is plotted along the carbide.
- Figure 30.** SEM images of precipitates at the ferrite/austenite interface. (a) A possible sigma/laves phase in CF-3 steel aged for 8600 h at 360 °C; (b) a carbide phase in CF-8 steel aged for 4300 h at 360 °C; (c) a boride phase in CF-8 steel aged for 12900 h at 360 °C; (d) an unknown phase in CF-8 steel aged for 12900 h at 280 °C; (e) a carbide phase in CF-8 steel aged for 17200 h at 280 °C; and (f) an unknown phase in CF-8 steel aged for 17200 h at 360 °C.
- Figure 31.** (a) S/TEM image and (b) chemical mapping of carbide along the ferrite/austenite interface of the CF-8 samples aged to 17200 hours at 400 °C
- Figure 32.** (a) Reconstruction and (b) proxigram of possible  $M_{23}C_6$  carbide in 4300 hour aged CF-8 sample at 360 °C
- Figure 33.** (a) Reconstruction (scale in nm) and (b) proxigram of possible  $M_{23}C_6$  carbide in 12900 hour aged CF-8 sample at 320 °C
- Figure 34.** (a) Reconstruction (scale in nm) and (b) proxigram of possible  $M_{23}C_6$  carbide in 17200 hour aged CF-8 sample at 280 °C
- Figure 35.** (a) Reconstruction (scale in nm) and (b) proxigram of possible  $Cr_2B$  boride in 12900 hour aged CF-8 sample at 360 °C
- Figure 36.** (a) Reconstruction (scale in nm) and (b) proxigram of possible  $Cr_{23}(C,B)_6$  hybrid in 8600 hour aged CF-8 sample at 360 °C
- Figure 37.** (a) Reconstruction (scale in nm) and (b) proxigram of possible Sigma or Laves phase in 8600 hour aged CF-3 sample at 360 °C
- Figure 38.** Chemical composition of  $\alpha'$ -phase and  $\alpha$ -phase domains in CF-3 samples aged for 17,200 hours at (a) 280 °C, (b) 320 °C, (c) 360 °C, and (d) 400 °C.
- Figure 39.** Cr composition in  $\alpha'$ -phase and  $\alpha$ -phase domains in all samples of CF-3 alloy.
- Figure 40.** Cr composition in  $\alpha'$ -phase and  $\alpha$ -phase domains in all samples of CF-8 alloy.
- Figure 41.** Wavelength size distributions of unaged (a) CF-3 and (b) CF-8 alloy. Amplitude size distributions of unaged (c) CF-3 and (d) CF-8 alloy.

- Figure 42.** Increase of wavelength in (a) CF-3 and (b) CF-8 alloy during thermal aging. Increase of amplitude in (c) CF-3 and (d) CF-8 alloy during thermal aging.
- Figure 43.** Comparison of the developed 1-D concentration profile to the other traditional methods in measuring wavelengths and amplitudes. Wavelength values with (a) 1-D method and (b) ACF methods. Amplitude values with (c) 1-D method and (d) LBM methods.
- Figure 44.** Chemical composition of possible G-phase forming zones in CF-3 steel after 17200 hours of thermal aging at (a) 280 °C, (b) 320 °C, (c) 360 °C, and (d) 400 °C.
- Figure 45.** Ni composition in CF-3 steels at all aging conditions.
- Figure 46.** Ni composition in CF-8 steels at all aging conditions.
- Figure 47.** G-phase forming elements composition in CF-3 steels at all aging conditions.
- Figure 48.** Plot of (a) radius:  $\langle R \rangle$ , (b) number density:  $N_v$ , and (c) volume percentage:  $V_p$  of G-phase precipitates in CF-3 steel.
- Figure 49.** Coalescence of Ni-Si-Mn-Cu clusters in CF-3 steel of samples aged for (a) 4300 h at 360 °C, (b) 4300 h at 400 °C, (c) 17200 h at 360 °C, and (d) 17200 h at 400 °C.
- Figure 50.** Coalescence of Ni-Si-Mn-Cu clusters in CF-8 steel of samples aged for (a) 4300 h at 360 °C, (b) 4300 h at 400 °C, (c) 17200 h at 360 °C, and (d) 17200 h at 400 °C.
- Figure 51.** Activation energy of spinodal decomposition derived from only the amplitude component of D.o.D at low operational (blue) and high accelerated (red) temperatures at (a) 4300 h, (b) 8600 h, (c) 12900 h and (d) 17200 h.
- Figure 52.** Activation energy of spinodal decomposition derived from only the wavelength component of D.o.D at low operational (blue) and high accelerated (red) temperatures at (a) 4300 h, (b) 8600 h, (c) 12900 h and (d) 17200 h.
- Figure 53.** Activation energy of spinodal decomposition derived from both amplitude and wavelength components of D.o.D at low operational (blue) and high accelerated (red) temperatures at (a) 4300 h, (b) 8600 h, (c) 12900 h and (d) 17200 h.
- Figure 54.** Activation energy of G-phase precipitation derived from the amplitude component of D.o.D at low operational (blue) and high accelerated (red) temperatures at (a) 4300 h, (b) 8600 h, (c) 12900 h and (d) 17200 h.
- Figure 55.** Activation energy of G-phase precipitation derived from the volume fraction component of D.o.D at low operational (blue) and high accelerated (red) temperatures at (a) 4300 h, (b) 8600 h, (c) 12900 h and (d) 17200 h.
- Figure 56.** Activation energy of G-phase precipitation derived both amplitude and volume fraction components of D.o.D at low operational (blue) and high accelerated (red) temperatures at (a) 4300 h, (b) 8600 h, (c) 12900 h and (d) 17200 h.
- Figure 57.** Activation energy plot of all values in (a) spinodal decomposition and (b) G-phase precipitation.

- Figure 58.** CF-3 samples aged for 17200 hours at 400 °C illustrating: (a) APT reconstruction displaying Ni atoms (green) and G-phase precipitates delineated by 6.5 at. % Ni isoncentration surfaces; (b) 3 nm slice of the same APT reconstruction displaying Cr (magenta) and Ni (green) atoms, indicating G-phase precipitates are located within the interface of spinodal decomposition domains (Fe atoms not shown for clarity).
- Figure 59.** Hyperbolic tangent fitting of D.o.D at all unaged and aged samples of the CF-3 alloy.
- Figure 60.** Activation energy of interpolated spinodal decomposition data that were derived from both amplitude and wavelength components of D.o.D at low operational (blue) and high accelerated (red) temperatures at (a) 5 h, (b) 500 h, (c) 2000 h and (d) 3500 h.
- Figure 61.** G-phase forming zones as delineated by 6.5 at. % Ni in unaged and all 4300 hours aged steels for both (a) CF-3 and (b) CF-8 alloys.
- Figure 62.** Comparing the effect of distance from carbide on spinodal decomposition and G-phase precipitation on the ferrite phase of two CF-8 samples both aged for 4300 hours at 360 °C: (a) far from carbide, (b) near carbide

## List of Abbreviations

3-D	Three dimensional
ACF	Auto-Correlation Function
$A_j^*$	Ratio of normalized amplitude to concentration
$\alpha/\alpha'$	decomposing ferrite phase spinodal domains
a.m.u	atomic mass unit
APFIM	Atom Probe Field Ion Microscopy
APT	Atom Probe Tomography
ASTM	American Society for Testing and Materials
b.c.c	body centered cubic
BF	Bright field
$^{\circ}\text{C}$	degree centigrade
$C_j^{\delta}$	Concentration of element i in ferrite phase
CALPHAD	Computer Coupling of Phase Diagrams and Thermochemistry
CAMECA	Compagnie des Applications Mécaniques et Electroniques au Cinéma et à l'Atomistique
CDSS	Cast Duplex Stainless Steels
CF-3	Centrifugal cast alloy with maximum of 0.03 wt.% C
CF-3M	Centrifugal cast alloy with maximum of 0.03 wt.% C and Mo
CF-8	Centrifugal cast alloy with maximum of 0.08 wt.% C
CF-8M	Centrifugal cast alloy with maximum of 0.08 wt.% C and Mo
$C_{\infty}$	equilibrium solute concentration in matrix
$\chi$	Chi phase
$C_r$	solute concentration of matrix near a particle of radius r
$\text{Cr}_{\text{eq}}/\text{Nieq}$	ratio of Chromium-equivalent to Nickle-equivalent elements
CVN	Charpy V-notch
$\delta$	width of grain boundary / unaged ferrite phase
d	grain size
$D_{\text{app}}$	Apparent Diffusion
$D_b$	bulk diffusion
$\Delta G$	free energy
$\Delta G_{\text{mix}}$	change in free energy of mixing
$\Delta H_{\text{mix}}$	change in enthalpy of mixing
$\Delta S_{\text{mix}}$	change in entropy of mixing
$D_i$	Diffusion of element i
$D_l$	lattice diffusion
DC	Direct current
DBTT	Ductile Brittle Transition Temperature
DF	Dark field
$D_o$	Diffusion coefficient
D.o.D	Degree of Degradation
DTSA-II	Desktop Spectrum Analyzer (DTSA)
EDS	Energy Dispersive Spectrometry

EPMA	Electron Probe Microscopy Analysis
Exp[]	exponential function
$\varepsilon$	Epsilon Cu phase
eV	electron volts
f.c.c	face centered cubic
FIB	Focused Ion Beam
FIM	Field Ion Microscopy
Ft-lbs	foot-pounds
$\text{Ga}^+$	Gallium ions
GB	Grain boundary
$G_i$	free energy of element i
$G_L$	free energy of liquid
$G_o$	standard free energy
$G_S$	free energy of solid
$\gamma$	Interface surface energy / Austenite phase
$\gamma_2$	New second austenite phase
h	hours
HAADF	high-angle annular dark-field
HR	High Resolution
HV500g	Vickers Micro-hardness with 500g load
Isosurface	Isoconcentration surface
IVAS	Integrated Visualization and Analysis Software
JEOL	Japan Electron Optics Laboratory
K	Kelvins
$K_\alpha$	K-alpha emission line
$K_\beta$	K-beta emission line
kgf	kilogram-force
kJ	kilojoules
$K_j^{\delta/\gamma}$	Partitioning ratio
K-S	Kurdjomov-Sachs relationship
$L_\alpha$	L-alpha emission line
LBM	Larson-Bar-on-Miller
LEAP	Local Electrode Atom Probe
$\ln$	Natural log
$\lambda$	wavelength
LSW	Lifshitz S Wagner
LWR	Light Water Reactors
MA	Mean Amplitude
mm	millimeter
$\mu_i$	Standard mean of component i / chemical potential of element i
MW	Mean Wavelength
n	number of electrons / time exponent
N	Newtons
NDZ	Nickle Depletion Zone
$\eta$	Atom Probe efficiency factor / Laves Phase
NIST	National Institute of Standards and Technology

v	velocity
N <sub>v</sub>	number density
OES	Optical Emissions Spectrometry
OR	Orientation Relationship
Q	activation energy
P <sub>a</sub>	amplitude method
Pa	Pascals
π	Pi phase
p(x)	probability
R	R phase
<R>	mean radius
RDF	Radial Distribution Function
RMS	Root Mean Square
ROI	Region of Interest
ρ	density
P/B	Peak-to-Background ratio
Proxigram	Proximity Histogram
R	Gas constant
r	radius
SAED	Selected Area Electron Diffraction
SANS	Small-Angle Neutron Scattering
SDZ	Solute Depletion Zone
SEM	Scanning Electron Microscopy
SI	International Standard units
σ	Sigma phase
σ <sup>2</sup>	Variance
STEM	Scanning Transmission Electron Microscopy
t	time
T	temperature
Tanh	Hyperbolic tangent
TEM	Transmission Electron Microscopy
θ	temperature factor
TOF	Time of flight
TTT	Time Temperature Transition
V <sub>e</sub>	voltage
V <sub>f</sub>	Volume fraction
V <sub>m</sub>	molar volume
V <sub>p</sub>	Volume percentage
VP	Variable Pressure
XFEG	Field emission electron source
X <sub>i</sub>	mole fraction of element i
<X>	3-D RMS diffusion distance
ZAF	atomic number, x-ray absorption, x-ray fluorescence



# Chapter 1: Introduction

Steels are an important class of materials, whose use is indispensable in the 21st century from low-end daily applications in cooking utensils to sophisticated ones in space vehicle. The tonnage of steel production and consumption in major economies is constantly on the rise [1]. Stainless steels have an attractive combination of good corrosion resistance and excellent mechanical properties – higher strength, higher ductility, and better weldability. Duplex stainless steels (DSS) are finding increased applications as structural materials in critical components of nuclear power plants, such as valve bodies, pump casings, primary coolant piping, and some reactor core internal components [1]–[25]. Although stainless steels have been studied for more than a century, there is room for further development to improve performance in harsher environments. The excellent combination of mechanical properties and corrosion resistance of DSS is the result of the presence of duplex phases, body-centered cubic (b.c.c.)  $\delta$ -ferrite and face-centered cubic (f.c.c.)  $\gamma$ -austenite, in the microstructure. The ASTM Specification A-351 for CDSS Grades, such as CF-3 and CF-8, predominantly used in nuclear power industries, has ferrite content in the range of 9-15%.

The current generation of light-water reactors (LWRs) operates at a temperature of  $\sim 288$  °C and pressure of  $\sim 7$  MPa for boiling-water reactor and  $\sim 15$  MPa for pressurized water reactors [26], [27]. Generation IV nuclear reactors will require demanding operational conditions such as elevated temperatures, extended neutron exposures and corrosive environments from the molten-salt fuels. Ferritic steels are lead candidates for Gen IV due to their higher thermal conductivities, lower

thermal expansion coefficients, and superior resistance to swelling. Despite of its many advantages, ferritic steels exhibit low-temperature embrittlement that leads to a substantial increase in the ductile-to-brittle transition temperature ( $\Delta$ DBTT) and loss of impact toughness. Among the many factors that play roles in embrittlement, such as irradiation, fatigue stress, corrosion and thermal, this thesis will only focus on the contribution of low-temperature aging to the microstructural and mechanical evolution induced in the ferrite phase of CF-3 and CF-8 cast DSS.

Materials in nuclear service are subjected to various types of radiation, such as neutron, gamma, beta, and alpha. The latter three types, gamma, beta, and alpha, are classified as ionizing radiation because they only interact with electrons on the outer shells. Ionization radiation disrupts covalent bonding, but not metallic bonding, which has a sea of free flowing electrons. However, neutron radiation displaces atoms, causing substantial structural damage that result in significant embrittlement. The defects created in the crystal irregularity hinder deformation processes [28]–[31].

The iron-chromium binary system has a miscibility gap in the LWR operational temperature range, as shown in Figure 1, where the ferritic phase decomposes into an iron-rich bcc phase ( $\alpha$ ) and a chromium-rich bcc phase ( $\alpha'$ ) [32], [33]. The rate of embrittlement is highest at 475 °C and is referred to as the 475 °C embrittlement. Since massive structural and cooling system components are installed in LWRs, any significant degradation in mechanical properties will raise a serious concern on the integrity of the entire power plant. A rupture of the primary pressure boundary could lead to a severe loss-of-coolant accident and possible exposure of the public to radiation. The replacement cost is high and therefore a thorough scientific

understanding and systematic monitoring of the thermal aging degradation of CDSS is essential for assessing the plant safety. The current design lifetime is 40 years. No conclusive prediction to 60-80 years can be made as currently no data exists beyond the current timeframe.

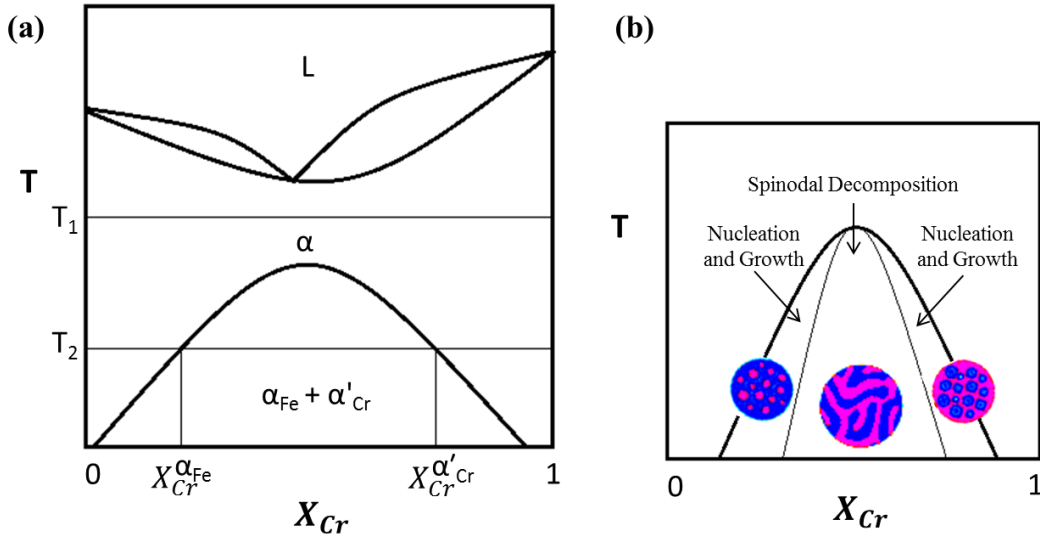


**Figure 1.** (a) Fe-Cr phase diagram, (b) Regions of miscibility gap. Adapted from [34].

Numerous aging experiments in the past [10], [35]–[37] have been performed at or above 400 °C to investigate microstructural evolution and mechanical behaviors and to predict long-term CDSS behaviors. However, such highly-accelerated aging treatment above the operation temperature range is yet to be validated for simulation of the lower temperatures. Since it is impractical to pursue a real time aging experiment for the extended life time of 60 years or more, accelerated aging experiments have been carried out for much shorter periods of about 3 years. The principle in choosing the aging temperature and time is that the embrittling mechanisms at the elevated temperatures do not differ from those found in the service temperature range of 280–320 °C.

Some studies [2], [22], [38] measure the ‘apparent’ activation energy based on mechanical tests that are an average of multiple activation energies corresponding to multiple mechanisms. The activation energy (Q) measured by the change mechanical properties, such as the increase of hardness or the decrease of toughness, do not accurately represent the microstructural progresses in CDSSs, because those macroscopic properties can include both negative and positive effects from the aging processes. For example, larger grain size may soften the material according to Hall-Petch equation, while compositional variations may contribute to strain hardening. In addition, some energy goes into the formation and propagation of the crack, regardless of the microstructural evolution taking place. The activation energies for the diffusion of metallic elements in the ferrite phase are in the range of 210–250 kJ/mol as shown in Table 1 [39]. This Q-range should approximately represent the spinodal decomposition process to form  $\alpha$  and  $\alpha'$  domains.

**Table 1.** Activation energy of metallic species in Fe lattice. Reported from Smithels Metals Reference Book [39].

<b>Element</b>	<b>Q (kJ/mol)</b>
Cr	250-291
Ni	234-314
Mn	219-261
C	147
Cu	272-306

Given the importance of reliability, it is vital to understand the embrittling mechanisms under service conditions. With this logic, the mechanical properties are dependent upon a number of parameters such as the properties of component phases and their interactions. There is a lack of

understanding in regard to some fundamental aspects of diffusion mechanisms. The total volume of the diffusing species should be taken into account from the increasing size and concentration of evolving precipitates. Previous studies [40], [41] have only studied the increase of particle size based on the Lifshitz-Slyozov-Wagner (LSW)

theory of the time exponent to measure growth rate and infer a diffusion mechanism. The LSW theory only applies to dilute concentrations and therefore is not suitable for use in a system with increasing compositional fluctuations. A clear understanding of the diffusion mechanisms will lead into the development of prediction models.

To address the above issues, a systematic investigation has been undertaken in this report. The specific goals are as followed:

1. Provide an overview summary on the current understanding of thermal aging phenomena in order to have a meaningful discussion of past and on-going studies.
2. Carry out an experimental investigation of thermal embrittlement by thermally ageing two CDSS alloys: CF-3 and CF-8 at two operational temperatures 280 °C and 320 °C, and two accelerated temperatures 360 °C and 400 °C at four times 4300 hours, 8600 hours, 12900 hours, and 17200 hours.
3. Carry out mechanical testing of the unaged and all aged samples at room temperature to measure the change in mechanical properties and note the deformation modes from the fracture surfaces.
4. Identify and characterize the fracture surfaces by characterization techniques at multiple length scales, such as optical microscopy, Scanning and Transmission Electron Microscopy (SEM/TEM), and a particular focus on Atom Probe Tomography (APT), in order to study microstructural evolution.

5. Study the kinetics of spinodal decomposition and G-phase precipitation in the vicinity of the ferrite/austenite phase boundary, where fracture is most likely to originate and propagate.
6. Develop new method to quantitatively evaluate the wavelength and amplitude of the phase separation in Fe-Cr alloys based on the data obtained from APT and compare the values to traditional methods, such as the auto-correlation function (ACF) for determining the wavelength and the Langer-Bar-on-Miller (LBM) method for determining the amplitude.
7. Develop a new approach of measuring total volume of diffusing elements by taking both the increase in size and concentration into account. Calculate the activation energies of diffusing elements in order to describe the diffusion mechanism.
8. Investigate the role of alloying elements as an embrittling factor because of their participation in the precipitation of secondary phases and their influence on the embrittlement and hardening compared to the binary alloy.

The structure of the thesis is as follows: A thorough literature review and technical background is presented in Chapter 2; a detailed summary of the experimental procedures is outlined in Chapter 3; the development of new analytical techniques are presented in Chapter 4; the experimental results and discussion are listed methodically in Chapter 5; the kinetic analysis is analyzed critically in Chapter 6; and lastly, Chapter 7-8 list the main results and provide suggestion for future work.

## Chapter 2: Background

In this chapter, the process of steel fabrication and the resulting phase transformations is presented. The thermodynamics and kinetics of these phase transformations are explained in context of scientific theory and literature review.

### 2.1 Steel Fabrication

The continuous advancement of DSS to better grades combined with increasing demand for obtaining better properties has provided fresh impetus for further research on steels. The factors in the fabrications process of DSS are: 2.1.1 Processing Route (cast and wrought) and 2.1.2 Composition.

#### 2.1.1 Processing Route

The degree and kinetics of thermal embrittlement of duplex structures such as CDSS materials are controlled primarily by the amount, size, and distribution of the ferrite phase, and the presence of carbides at the phase boundaries. These material parameters in turn depend on the chemical composition and the manufacturing process. Casting technologies enable the fabrication of large components with proper resistance to environmental attacks.

The effect of manufacturing process on the thermal embrittlement of CDSS materials has been investigated by Massoud et al. [42]. The manufacturing process for castings consists of solidification of the material from a liquid state at around 1500°C (2732°F), followed by a homogenizing heat treatment of the solid at 1050–1150°C (1922–2102°F) and water quenching. CDSS with high Cr contents solidify into a primary  $\delta$ -ferrite phase. During cooling of the solidified material, if the

concentrations of the  $\gamma$ -forming elements such as C, N, Mn, and Ni, are sufficient, a fraction of the  $\delta$ -ferrite transforms to  $\gamma$ -austenite by solid-state  $\delta$  to  $\gamma$  transformation. Furthermore, if the cooling rate between 900 and 600°C (1652 and 1112°F) is slow,  $\delta$ -ferrite can transform to the brittle sigma ( $\sigma$ ) phase, and  $M_{23}C_6$  carbides can also precipitate at the  $\delta/\gamma$  phase boundaries, both of which lead to degradation of the mechanical properties of the material. The homogenizing treatment holding time and the quenching rate affect the beginning of the decomposition of the ferrite and consequently the overall kinetics of aging.

### 2.1.2 Composition

In general, steels are mainly composed of Fe and C, with some other alloying elements as well to meet the specific practical needs. Carbon (C) is an interstitial solid solution strengthener. Its small radius can fit within the large octahedral voids of the FCC lattice, compared to the tetrahedral and octahedral voids of the BCC phase, and thus is a strong austenite former [1]. Chromium (Cr) is the most important alloying element in the CDSS systems. With content of at least 10.5 wt. %, Cr provides the stainless characteristic of steels. The corrosion resistance stems from a dense layer of chromium oxide that forms on the steel surface and protects the underlying steel from further corrosion when exposed to a corrosive environment [1]. Nickel (Ni) is an austenite-stabilizing element, which is added to enable a duplex microstructure. However, Ni plays a role in forming intermetallic compounds, such as G-phase precipitates. Molybdenum (Mo) is added to enhance the resistance against pitting corrosion. It slightly increases mechanical strength and strongly promotes a ferritic microstructure. The Fe-Mo phase diagram also has a miscibility gap [43].

Therefore, Mo may enhance spinodal decomposition of Fe-Cr. In addition, Mo enhances formation of secondary phases, such as laves, sigma, and carbides. Copper (Cu) improves corrosion resistance and promotes the austenite phase. It can be added to decrease work hardening and improve machinability. Manganese (Mn) improves hot ductility and improves machining by acting as a de-oxidant, taking sulfur and oxygen out of the melt. Silicon (Si) increases resistance to oxidation and promotes ferrite. Boron (B) drastically improves the hardenability. Only a small amount of B is needed or else it can cause embrittlement. Phosphorus (P) is a ferrite-stabilizer that increases strength and hardness, but at the expense of ductility and impact toughness.

## 2.2 Phases

A TTT diagram depicts the kinetics of phase transformations by illustrating the range over which various phases may form and the effects of increasing alloy content on the shift of the C-curve. The C-curves in the TTT diagrams are usually annotated with the percent of transformation occurred. For instance, the TTT diagram for eutectoid steel portrays two curves representing where the bainite phase starts and finishes the transformation [44]. However, the TTT diagram with the phases encountered during thermal aging only depicts one curve, which represents an estimation of when the transformation occurs. The formation of different microstructures is highly dependent on the alloying elements and heat treatments. The various phases that may be encountered in steels are listed below and depicted in the Time-Temperature-Transformation (TTT) diagram [45].

The phases above 500 °C in the TTT diagram are sigma ( $\sigma$ ) phase,  $\text{Cr}_2\text{N}$ , Chi ( $\chi$ ) phase,  $\gamma_2$  phase,  $M_{23}C_6$  carbides, and R phase. The phases below 500 °C in the

TTT diagram are  $\pi$  phase,  $\epsilon$ -Cu phase,  $\alpha'$  phase, and G-phase precipitates. The elemental factors that shift the TTT curves are Mo, Si, Cr, and Cu. The compositions and lattice parameters are to be referred with caution as some of these phases may vary with the alloy. High temperature precipitants are almost invariably regarded as being deleterious.

Precipitation in cast stainless steels will be slow at temperatures below 400 °C and is predicted not to reach equilibrium in the design life of LWRs. Equilibrium calculations were carried out for CF-3 and CF-8 using the CALPHAD method [46]. In the calculation, only the major alloy elements, Fe, Cr, Ni, Mo, and Si, and key trace elements, C and N, were considered. The calculation was performed under the assumption that no austenite–ferrite transformation occurs in the aging temperature range of 290 °C to 400 °C. However, significant phase changes occur in the form of precipitation within respective phases. The mole fractions of precipitate phases are given as functions of aging temperature. The equilibrium precipitates in the austenite phase of the CF-3 alloy were: sigma ( $\sigma$ ) phase decreased from 26% to 24% as aging temperature increased; G-phase precipitates decreased from 3% to 0% as aging temperature increased;  $M_{23}C_6$  carbides and  $Cr_2N$  nitrides had constant mole fraction of 0.5% and 1.5%, respectively; and laves ( $\eta$ ) phase had a small amount of 0.1% that decreased with aging temperature. The equilibrium precipitates in the austenite phase of the CF-8 alloy were: sigma ( $\sigma$ ) phase decreased from 24% to 23% as aging temperature increased; G-phase precipitates decreased from 5% to 0.1% as aging temperature increased; and  $M_{23}C_6$  carbides and  $Cr_2N$  nitrides had constant mole fraction of 2% and 1%, respectively. The equilibrium precipitates in the ferrite phase

of the CF-3 alloy were:  $\alpha'$  phase decreased from 23% to 19% as aging temperature increased; G-phase precipitates,  $M_{23}C_6$  carbides, and laves ( $\eta$ ) phase had constant mole fraction of 5%, 0.01%, and 1.5%, respectively;  $Cr_2N$  nitrides precipitated only at highest aging temperature with a mole fraction of 0.1%; and  $\pi$  phase decreased from 1% to 0% as the aging temperature increased. Lastly, the equilibrium precipitates in the ferrite phase of the CF-8 alloy were:  $\alpha'$  phase decreased from 21% to 18% as aging temperature increased; G-phase precipitates,  $M_{23}C_6$  carbides, and laves ( $\eta$ ) phase had constant mole fraction of 7%, 0.5%, and 1%, respectively;  $Cr_2N$  nitrides precipitated only at highest aging temperature with a mole fraction of 0.1%; and  $\pi$  phase decreased from 0.5% to 0% as the aging temperature increased.

The major precipitates,  $\sigma$  and  $\alpha'$  phases, were predominantly formed in the austenite and ferrite phases, respectively, while other minor phases were found in both phases. The equilibrium precipitates in austenite were  $\sigma$ -phase, G-phase, chromium nitride ( $Cr_2N$ ), Laves ( $\eta$ ) phase,  $M_{23}C_6$  carbide, and  $\pi$ -phase, while those in ferrite were  $\alpha'$ -phase (spinodal decomposition product), G-phase, Laves ( $\eta$ ) phase, chromium nitride ( $Cr_2N$ ),  $M_{23}C_6$  carbide, and  $\pi$ -phase. It is worth noting that there are other precipitates that may form in CDSSs but at a very low rate [46]. The complexities in diffusion and deformation mechanisms increase for two or more phase materials. The orientation relationship between the phases contributes to interfacial strain. The requirements for a coherent interface are sharing a common interface plane, alignment of slip planes, and similar lattice parameters.

### 2.2.1 Austenite and Ferrite phases

Recent research efforts have been made in the prediction of the ferrite to austenite phase proportions because the phase balance controls the mechanical properties. A good correlation was found to exist between the ferrite content and composition. Schaeffler and Long-Delong constitution diagrams are used for DSS [47]. Newer versions of expressions have been developed in consideration of more alloying elements. The alloying elements on the phase balance are quantified by using Ni and Cr equivalent numbers for austenite-stabilizers and ferrite-stabilizers, respectively. A weakness of the use of  $Cr_{eq}$  and  $Ni_{eq}$  is the coefficients associated with the alloying elements are constants, where the interactions among the various elements are not factored in. The ferrite content of the casting is estimated from the central line of the Schoefer diagram [ASTM A800]. The composition ratio of chromium equivalent,  $Cr_{eq}$ , to nickel equivalent,  $Ni_{eq}$ , is determined from the following formula:  $(Cr_{eq}/Ni_{eq}) = (Cr + 1.5Si + 1.4Mo + Nb - 4.99)/(Ni + 30C + 0.5Mn + 26(N - 0.02) + 2.77)$ . As the  $Cr_{eq}/Ni_{eq}$  ratio increases from 0.8 to 2.2, the range of ferrite content increases from 0 to 70%.

Higher ferrite content generally leads to a higher tensile strength due to the intrinsic strength of the ferrite phase and its propensity to form precipitates, while the austenite phase usually has higher ductility and fewer precipitates. The austenite is faceted with a Kurdjumov Sachs (K-S) relationship to the ferrite phase, where the close packed planes and directions are aligned  $(111)_{fcc} // (110)_{bcc}$ ,  $[110]_{fcc} // [111]_{bcc}$  [1].

In the austenite matrix phase, thermal aging induces various precipitations but usually causes a negligible effect on the mechanical properties of the phase because

the precipitation kinetics of diffusion is relatively slow in the closed packed structure. In contrast, the formation of Cr-rich  $\alpha'$  phase and Fe-rich  $\alpha$  phase by Spinodal decomposition of the ferrite phase is known to be the primary mechanism for thermal embrittlement in CDSS. The  $\alpha'$ -phase particles can harden the ferrite matrix and reduce the capability of plastic deformation. In a ferritic/austenite duplex structure, the hardened ferrite may fail in brittle mode but the surrounding austenite can provide ductility. However, the ferrite/austenite phase boundary provides an easy path for crack propagation in high-C or high-N steels because of the excessive carbides or other precipitates formed at boundaries.

#### 2.2.2 Fe-rich phase ( $\alpha$ ) and Cr-rich phase ( $\alpha'$ )

Within the miscibility gap of the Fe-Cr phase diagram, Figure 1(a), a thermally activated separation of chromium by short-range diffusion in the Fe-Cr solid solution within the ferrite phase, results in the formation of Fe-rich phase ( $\alpha$ ) and Cr-rich phase ( $\alpha'$ ) domains. The  $\alpha'$ -phase shares the same b.c.c lattice with the original  $\delta$ -ferrite and its counterpart  $\alpha$ -phase with a slight misfit in lattice constant (0.2886 nm for  $\alpha$  and 0.2885 nm for  $\alpha'$ ) and a higher chromium concentration [1]. The morphologies of  $\alpha$  and  $\alpha'$  are temperature and composition dependent. The phase separation may form an interconnected network or isolated regions through either spinodal mechanism or nucleation-and-growth, respectively, Figure 1(b). The strain induced between the developing  $\alpha$  and  $\alpha'$  domains could increase the hardness and decrease the ductility because they can act as Orowan obstacles to impede the movement of dislocations and promote brittle fracture. The degree of embrittlement and, hence, the toughness of the material, is controlled by the amount of brittle

fracture. Consequently, the amount, size, and distribution of the ferrite phase in the duplex structure are significant factors on the extent of embrittlement.

The time-temperature-transformation (TTT) curves show that at temperatures below 500 °C, the precipitation of  $\alpha'$  phase leads to embrittlement, while at temperatures above 550°C, the embrittlement is largely due to formation of sigma phase. The TTT curves also show that  $\alpha'$  phase is not stable at 550°C. Some researchers [48] have annealed the steels at above 500 °C for a short time to dissolve  $\alpha'$  phase and virtually recover the fracture toughness.

In order to overcome or suppress the  $\alpha'$  phase, extensive effort is needed to understand the mechanisms and the influence of multiple factors, such as, heat treatment and alloying composition.

### 2.2.3 G-phase

The G-phase is a nickel silicide that has f.c.c lattice. The standard stoichiometry is  $\text{Ni}_{16}\text{Si}_7\text{Ti}_6$  with possible substitutions of Ni and Ti by Cr, Fe, Mo, and Mn [5], [40], [49]. The composition and lattice parameter of G-phase is variant with the alloy composition. It forms at the ferritic interdomain between Fe-rich phase  $\alpha$  and Cr-rich phase  $\alpha'$ . The interdomain is gradually enriched with G-phase forming elements that are continually ejected from the  $\alpha$  and  $\alpha'$  domains during spinodal decomposition. When the enrichment reaches a critical composition and critical radius, the cluster of the G-phase elements transform to the G-phase precipitate in a two-step process as described by [49]. The G-phase forms a cube-on-cube orientation relationship with the ferrite. The crystal axis directions of the f.c.c G-phase aligns with the b.c.c ferrite,  $\langle 100 \rangle_{\text{fcc}} // \langle 100 \rangle_{\text{bcc}}$ . The contribution of G-phase to hardening in

spinodally decomposed steel is a matter of controversy due to the interplay of their kinetics. Some researchers have proposed that hardening will be mainly contributed by the G-phase at the later stages of thermal ageing after  $\alpha'$ -Cr has contributed to the substantial initial hardening [8]. Other scientists [48] oppose citing results from annealing experiments illustrating that the mechanical properties do not change as the G-phase coarsens. In order to isolate the embrittling effect of G-phase from the spinodal decomposition, Chung et al, in an early study, reannealed spinodally decomposed samples, such that the  $\alpha'$ -Cr completely dissolved, leaving behind the G-phase. The scientists found almost complete recovery of microhardness and toughness despite the presence of G-phase.

#### 2.2.4 $\epsilon$ (Cu) Phase

The  $\epsilon$ (Cu) phase that forms during phase separation will further lower the pitting corrosion resistance. Some researchers have reported that the  $\epsilon$ (Cu) phase acts as a nucleation site for G-phase precipitation [50].

#### 2.2.5 R Phase

The formation of the Mo-rich intermetallic R phase in the ferrite phase of DSS may lead to rapid and serious loss of toughness. R-phase has a trigonal crystal structure, whose closed packed planes and directions align with the ferrite,  $\langle 111 \rangle_{\text{ferrite}} // \langle 0001 \rangle_{\text{R}}$  and  $\{110\}_{\text{ferrite}} // \{30\bar{3}0\}_{\text{R}}$  [1]. The R phase is thought to be related to Laves phase.

### 2.2.6 Chi ( $\chi$ ) Phase

The  $\chi$ -phase is an intermetallic that forms frequently in DSS upon aging leading to degradation of mechanical properties. The  $\chi$ -phase is enriched in Mo and can transform to  $\sigma$ -phase upon prolonged ageing [1].

### 2.2.7 Sigma ( $\sigma$ ) Phase

The sigma phase is enriched with Cr and Mo. The  $\sigma$  phase is a tetragonal crystal composed of  $(\text{Cr,Mo})_x(\text{Ni,Fe})_y$ , forming at high-energy interfaces such as triple junction points, grain boundaries, and twin boundaries. The  $\sigma$ -phase acts as a nucleation site for cavities during grain-sliding and thus is deleterious to the plastic behavior of DSS [1]. The CALPHAD calculation predicted that a large amount greater than 20% of  $\sigma$ -phase will precipitate. However, the  $\sigma$ -phase precipitates is typically detected at temperatures between 600 °C and 1000 °C and its production below this temperature is very sluggish [46]. Thus, in a definite time, the mole fraction of the sigma phase will be very small. Such sluggish formation of the  $\sigma$  phase suggests that the total amount of precipitates in the austenite matrix after a practical term of aging will be less than that in the ferrite matrix.

### 2.2.8 Laves ( $\eta$ ) Phase

The Laves ( $\eta$ ) phase particles are hexagonal crystals that are composed of  $\text{Fe}_2\text{Mo}$  in many molybdenum-containing alloys. The Laves phase is often found as small equiaxed particles intragranularly, and occasionally found on the grain boundaries [1]. Usually, the Laves phases are considered detrimental to ductility and

fracture toughness, although its actual contribution will be insignificant due to the low mole fraction. In addition, the CF-3 and CF-8 steels are low Mo alloys.

#### 2.2.9 Cr<sub>2</sub>N and $\pi$ Phase

The precipitation of nitrides, such as Cr<sub>2</sub>N and  $\pi$  phase, compromises the ductility of the steel. Nitrogen (N) is added to increase the resistance to localized pitting attack and inter-granular corrosion. The Cr<sub>2</sub>N phase has discontinuous precipitation in ferritic and austenitic grains. The  $\pi$  phase precipitates intragranularly in the ferrite grains with an orientation relationship of  $\langle 100 \rangle_{\text{ferrite}} // \langle 100 \rangle_{\pi}$  [1].

#### 2.2.10 Carbides

In CDSS, different types of carbides may form. M<sub>7</sub>C<sub>3</sub> carbide has a pseudo-hexagonal lattice and is found when the carbon levels are very high [1]. The M<sub>23</sub>C<sub>6</sub> carbide is the most extensively studied due to their ubiquitous occurrence, where the metal atom (M) is most likely to be chromium. The M<sub>23</sub>C<sub>6</sub> has a f.c.c lattice and forms on the austenite-ferrite phase boundary. It is aligned with the austenite phase,  $(11-1)_{\text{M}_{23}\text{C}_6} // (111)_{\gamma}$  and satisfies a cube-on-cube orientation relationship [51]. Carbide-forming alloying elements are added to serve as strengtheners, but excessive alloying brings ductility loss. The attendant decrease in Cr content at the periphery of the ferrite phase degrades corrosion resistance and is the main culprit for sensitization. As the carbon supply is limited, the amount of M<sub>23</sub>C<sub>6</sub> is mainly determined by C content. Maetz et al [52] found that in 2101 lean DSS, the M<sub>23</sub>C<sub>6</sub> carbide volume fraction was 0.1 % throughout the aging study period.

The  $M_{23}C_6$  carbide has an incoherent boundary with the ferrite phase, featuring curved boundaries further into the ferrite phase in comparison to the straight boundaries at the edge of the austenite phase. The  $M_{23}C_6$  carbide depletes the ferrite phase of Cr and ejects Ni and Si into it. Some researchers [14] state that near the carbide, there is a eutectoid transformation of  $\delta \rightarrow M_{23}C_6 + \gamma_2$ , thus propagating the ferrite to austenite transformation. Other researchers [53] claim that the G-phase precipitates are precipitating instead of a new austenite phase.

### 2.3 Thermodynamics and Kinetics of Phase Transformations

The microstructure and properties of metallic materials are derived from phase transformations. The processing route of a component through thermo-mechanical treatments determines the microstructure, which are the phases and defects. The microstructure transforms with the driving force of decreasing the free energy. Thermodynamics and kinetics describe the order and speed of the transformation, respectively.

In a single component, the change in free energy is dependent on temperature only. However, in a binary system with two components, Fe and Cr, the free energy change varies by composition and temperature. The free energy will have terms for enthalpy and entropy of mixing, according to the equation:  $\Delta G_{\text{mix}} = \Delta H_{\text{mix}} - T\Delta S_{\text{mix}}$ . The enthalpy of mixing can be zero, positive, or negative depending if the system is ideal and has no preference of neighboring atoms, prefers Fe-Fe and Cr-Cr bonds, or prefers Fe-Cr bonds, respectively. Configurational entropy change comes from the possibilities of arranging atoms. Entropy increases according to the second law of thermodynamics, which will decrease the free energy. In the case of a positive

enthalpy of mixing, if  $\Delta H_{mix} > T\Delta S_{mix}$ , the  $\Delta G_{mix}$  will be higher than the  $G_o = X_{Fe}G_{Fe} + X_{Cr}G_{Cr}$  line, where  $X_iG_i$  are the molar fraction and free energy of component, i. The total free energy,  $G = G_o + \Delta G_{mix}$ , will be higher than  $G_o$  but not higher than  $G_{Fe}$  or  $G_{Cr}$ , because entropy has infinite slope in dilute systems, while enthalpy has a finite slope [34]. The shape of the G curve in (Figure 2) describes the existence of miscibility gap in phase diagrams at high and low temperatures indicated in Figure 1. At higher temperatures,  $\Delta H_{mix} \ll T\Delta S_{mix}$ , at all compositions, and therefore G will always be lower than  $G_o$ .

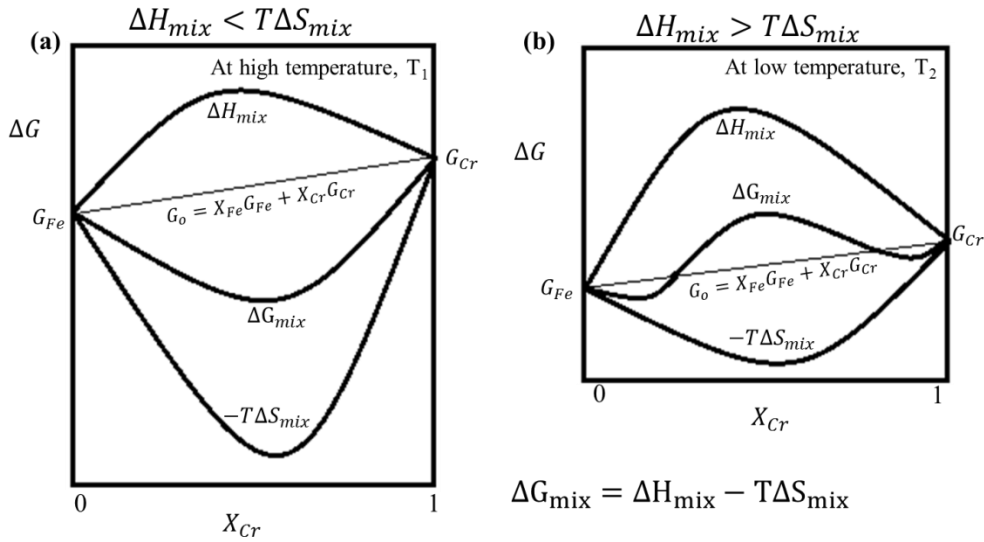


**Figure 2.** Free Energy diagrams at (a) high and (b) low temperatures indicated in **Figure 1**. Adapted from [34].

Phase diagrams are derived from free energy calculations at multiple temperatures. With decreasing temperature, the free energy of the solid ( $G_S$ ) and liquid ( $G_L$ ) phase will change differently. At higher temperatures,  $G_L < G_S$ , so that the liquid phase is stable and vice versa at lower temperatures. At temperatures, where  $G_S$  and  $G_L$  intersects variably with the composition, both phases exists at certain

regions determined by the common tangent. The phase fractions can be found by lever rule.

The Gibb's free energy is a function of temperature, T, pressure, P, and moles of elements,  $n_i$ . The partial derivative or slope of the free energy measures the change in free energy given change to element concentration. This value is called the chemical potential,  $\mu_i$ , and measures the activity of an element. The slope is extended to the  $X_{Cr} = 0$  to find  $\mu_{Fe}$  and  $X_{Cr} = 1$  to find  $\mu_{Cr}$ . On a system with a miscibility gap, the slopes at the  $\alpha_{Fe}$  phase and  $\alpha'_{Cr}$  phase will have different chemical potentials of elements Fe and Cr. From extending the slopes to the axis,  $\mu_{Fe}^{\alpha_{Fe}} < \mu_{Fe}^{\alpha'_{Cr}}$  and  $\mu_{Cr}^{\alpha'_{Cr}} < \mu_{Cr}^{\alpha_{Fe}}$ . This means that the chemical potential of Fe is less in  $\alpha_{Fe}$  phase compared to the  $\alpha'_{Cr}$  phase. Similarly, the chemical potential of Cr is higher in  $\alpha_{Fe}$  phase compared to the  $\alpha'_{Cr}$  phase. Diffusion goes from high to low chemical potential to decrease the free energy of the system. Here, Cr atoms will diffuse uphill from  $\alpha_{Fe}$  phase to  $\alpha'_{Cr}$  phase. Simultaneously, Fe atoms will diffuse against the gradient from  $\alpha'_{Cr}$  phase into  $\alpha_{Fe}$  phase, as shown in Figure 3. This type of phase separation has a spinodal decomposition mechanism and will be described in depth later.

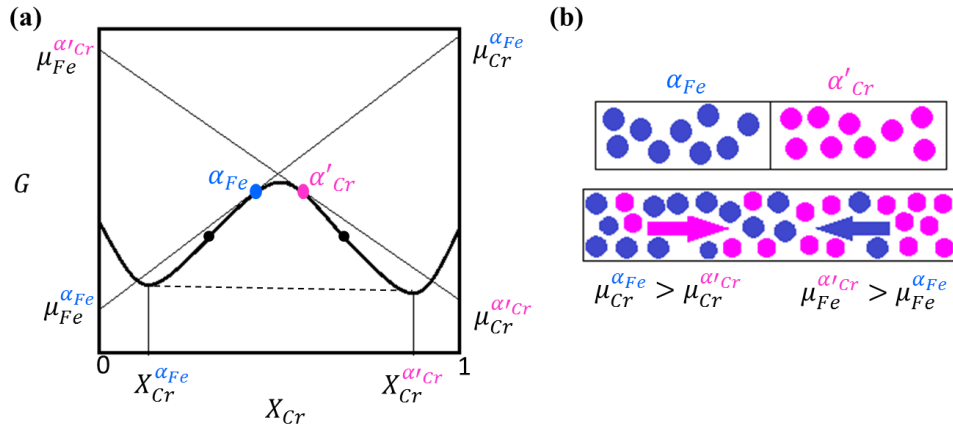


**Figure 3.** (a) Chemical potential of spinodal decomposition; (b) schematic of uphill diffusion. Adapted from [34].

### 2.3.1 Theory of Phase Separation

Phase separation in ferritic stainless steels is a type of phase transformation in which there is only a change in composition but not in the crystal structure. Besides in Fe-Cr alloys, phase separation has also been studied in systems such as Au-Ni [54]. The theory of phase separation originates from a doctoral thesis by Hillert in the 1950s [55], [56]. Later, the theory was extended and developed further by Cahn and Hilliard [57]–[59]. Phase diagrams showing a miscibility gap correspond to solid solutions exhibit clustering tendency, an ordering transformation. Within the miscibility gap, the decomposition can take place by either nucleation-and-growth or by spinodal mechanism, depending on the chromium concentration. Chandra et al. [60], [61] attempted to calculate the solubility of chromium in iron in the temperature range of 280 °C to 500 °C and predicted the boundaries within the miscibility gap for spinodal decomposition and nucleation-and-growth.

The difference between these two mechanisms can easily be distinguished by their morphologies, Figure 1(b). Spinodal decomposition is an up-hill diffusion

process due to the negative diffusivity inside the spinodal line [34]. At concentrations between the spinodal points where the second derivative of free energy with composition equals zero, the region is metastable. Phase separation via the spinodal mechanism is spontaneous and occurs without any incubation time. Between the miscibility gap boundary and the spinodal boundary, the phase separation occurs via nucleation-and-growth in a down-hill diffusion process. In this region, the composition is unstable according to the Gibbs energy curve. Usually, an incubation time is accompanied with the mechanism of nucleation-and-growth because there is an energy barrier to overcome for nucleation.

In nucleation and growth mechanism, once the particles nucleate, the composition of the second phase remains unaltered with time. The interface between the nucleating phase and the matrix is sharp and there is a random distribution of particle size and position. The particles tend to be spherical with low connectivity. On the other hand, in spinodal mechanism, there is a continuous fluctuation of composition until equilibrium is attained, the interface is initially diffuse but eventually sharpens, and there is a complex regularity in the sizes and distribution of phases in the networked non-spherical structure. In spinodal, the Fe-rich and Cr-rich domains have near-identical lattice parameters. The interfacial energies are low and hence the energy barrier is very small.

### 2.3.2 Nucleation, Growth, and Coarsening

The process of phase transformations is dynamic. There will be a range of particle sizes due to time of nucleation and rate of growth. Homogenous nucleation takes place throughout the system, while heterogeneous nucleation is an assisted

process where a surface can catalyze or facilitate the event by reducing the activation barrier. Nucleation implies the formation of an interface. Figure 4 shows that the free energy change as a function of radius is balanced by the two competitive factors, the volume free energy ( $\propto r^3$ ) and the interfacial energy ( $\propto r^2$ ) [34]. As the radius increases beyond the critical radius, the free energy reaches the maximum and starts to decrease due to the volume cubic radius contribution.

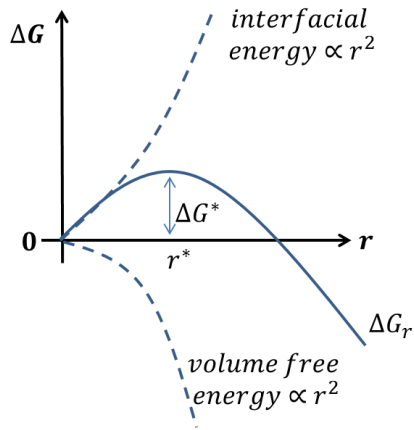


**Figure 4.** Homogenous nucleation. Adapted from [34].

The evolution of the size, number density, and volume fraction of G-phase particles has two regimes after nucleation. Initially, there is a simultaneous increase in size, number density, and volume fraction up to a certain time and temperatures. Secondly, there is a continuous increase in size but a decrease in the number density, whereas the volume

fraction behaves asymptotically towards its equilibrium value. These behaviors observed in the second regime are a signature of the coarsening regime of the G-phase particles as illustrated in Figure 5.

The evolution of the G-phase is observed after the spinodal decomposition is well developed. These observations confirm that G-phase precipitate formation at the interface of spinodal domains results from the rejection of G-forming species in the domains as depicted in Figure 6. When the composition at the inter-domains reaches a critical composition, G-phase particles crystallize.

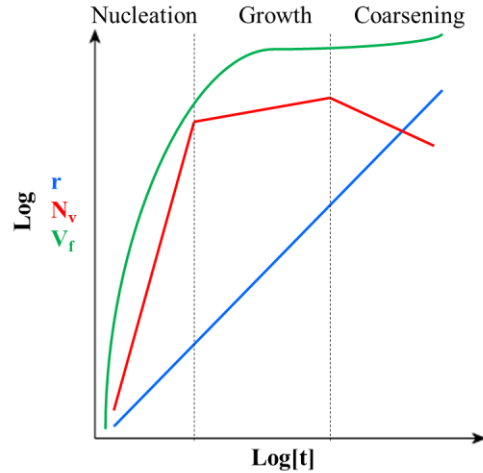


**Figure 5.** The change in size, number density, and volume fraction at different growth regimes

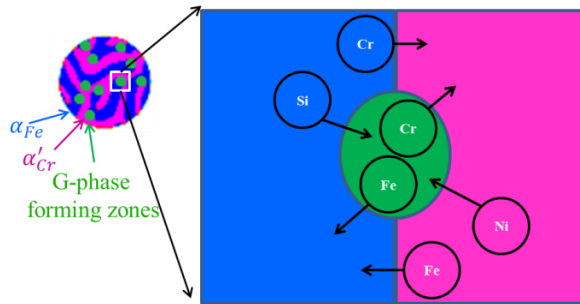


**Figure 6.** Flux of elements in spinodal decomposition domains and G-phase precipitates

The theory of particle coarsening was developed by Lifshitz and Slyozov and independently by Wagner, and is known as LSW theory [62], [63]. The isothermal grain growth can be represented by  $d = Kt^n$  or  $\ln[d] = \ln[K] + n \ln[t]$ , where  $d$  is the mean grain diameter,  $t$  is the time, and  $K$  is the constant of proportionality. The values of  $n$  and  $K$  explicitly depend on the coarsening mechanism and also on the morphology and volume percent of the component phases. The exponent  $n$  varies from 0.20 for pipe diffusion control to 0.33 for bulk diffusion [64], [65].

The LSW theory applies to Ostwaldian systems consisting of a solute-lean matrix with solute-rich particles. Excess free energy associated with the particles'

interfacial surface area leads to thermodynamic instability tending to decrease this surface free energy by the process of particle coarsening. The dissolution of the particles depends on their radius of curvature, described by the Gibbs-Thompson relation:  $C_r = C_\infty(1 + 2\gamma V_m/RT_r)$ , where  $C_r$  is the solute concentration of matrix near a particle of radius  $r$ ,  $C_\infty$  is the equilibrium solute concentration in matrix,  $\gamma$  is the interface free energy,  $V_m$  is the molar volume,  $R$  is the gas constant and  $T$  is the temperature [64]. As the curvature of the particle increases, the solute concentration in the matrix adjacent to the particle increases. The concentration gradient drives the solute to diffuse from the small particles towards the large particles in a process called particle coarsening. While maintaining a constant volume fraction, the small particles shrink as the larger ones grow. With time, the number density of the particles decreases as the mean radius increases.

To determine the activation energy, the parameter,  $\ln[K]$ , is the intercept of  $\ln[d] = \ln[K] + n \ln[t]$  and is related to temperature by the following equation:  $\ln[K] = \ln[K'] - Q/RT$ . The change in slope  $Q/R$  of the line  $\ln[K]$  vs  $1/T$  would suggest that the rate-controlling mechanism changes as the temperature varies. In the LSW theory,  $n$  represents the diffusion path mechanism and  $Q$  represents the ‘bottleneck’ or barrier for the slowest diffusing specie.

The coarsening kinetics may not solely be controlled by dislocation pipe, interface, or bulk/lattice diffusion. Figure 7 shows the rate controlling mechanisms as a function of inverse temperature. Bulk/lattice diffusion has greater diffusivity at higher temperatures, while grain boundary diffusion is greater at lower temperatures [34]. The apparent diffusivities is the contribution of both mechanisms, given by:

$D_{app} = D_l + D_b \delta/d$ , where  $D_l$  is the diffusivity of the lattice or bulk,  $D_b$ , is the diffusivity of grain boundary or interface,  $\delta$  is the effective width of grain boundary, and  $d$  is the effective mean grain size.

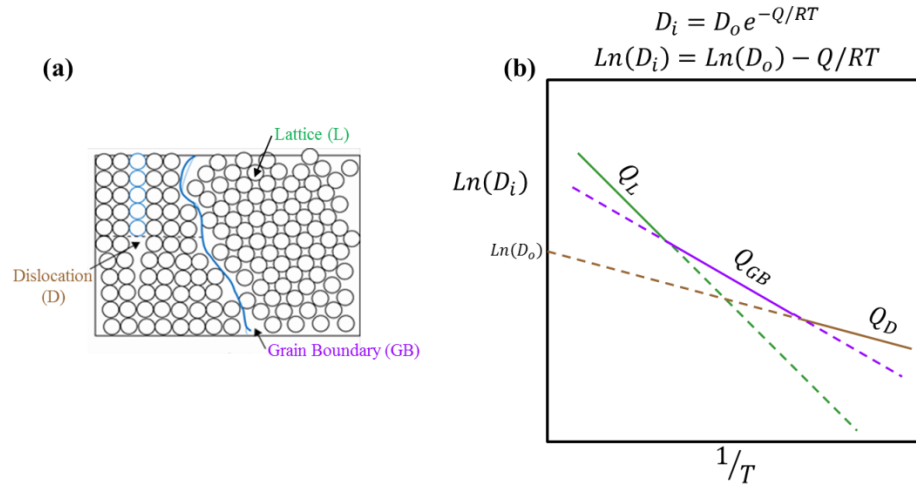


**Figure 7.** (a) Diffusion paths in steel; (b) Plot of diffusion as a function of inverse temperature illustrating the slope of the dominating diffusion mechanism with solid lines while contributing factors are in dashed lines. Adapted from [34].

The mutual exchange of fluxes in coarsening can only occur by the process of long-range diffusion. Diffusion is a process of mass transport by atomic movement under the influence of thermal energy and chemical potential gradient. Small atoms, such as C, can diffuse via interstitial mechanism. Larger atoms, such as Fe and Cr, proceed via substitutional diffusion. Defects, such as dislocations and grain boundaries, play a role in diffusion due to their open structure. The lower activation barrier in defects provides a higher diffusion rate than through the lattice as illustrated in Figure 7 (a). Diffusion on the surface has the lowest activation energy because the top layer has vacancies.

The slope of the diffusion versus inverse temperatures gives the activation barrier of diffusion ( $Q$ ) from the Arrhenius equation:  $D = D_o \text{Exp}[-Q/RT]$ , where

$D$  is  $\text{m}^2/\text{s}$ ,  $T$  is in  $\text{K}$ ,  $R$  is the ideal gas constant  $8.314 \text{ J/mol K}$ , and  $Q$  is in  $\text{J/mol}$ . Lower activation energy,  $Q$ , implies higher rates of diffusion. The diffusion coefficient,  $D_0$ , is constant within a defined temperature range; however, it varies with composition [66]. This key aspect was not taken into account in this study of spinodal decomposition, where the compositional amplitude increases with thermal aging time and temperature. The activation energies, derived from the slope of Figure 7 (b), increase in order from surface to dislocation pipe to grain boundary to lattice or bulk diffusion. Bulk/lattice diffusion is dominant at high temperatures because there is sufficient thermal energy from atomic vibrations to overcome the activation barrier. The solid lines represent the temperature range, where a certain diffusion mechanism is dominant.

## 2.4 Literature Review

### 2.4.1 Groundbreaking work

In order to characterize the phase separation in Fe-Cr alloys, scientists for almost a century have made advancements in finding the cause and effects of embrittlement. Although Becket [67] observed the hardness increase and ductility drop during the aging of stainless steels in 1938, the mechanism of hardening was not discovered until Fisher et al. [68] detected the formation of Cr-rich phase ( $\alpha'$ ) in 1953 by X-ray examinations, which showed that the precipitation of  $\alpha'$  should be responsible for the phenomenon of '475 °C Embrittlement' in ferritic stainless steels. Furthermore, Williams & Paxton in 1957 [69] were first to propose the existence of a miscibility gap in the Fe-Cr system. They confirmed that the 475 °C embrittlement was due to the formation of Cr-rich precipitates ( $\alpha'$ ) which can increase the hardness

while decreasing the ductility of the materials. Later, Cahn in the early 1960s theoretically explained the hardening mechanism by spinodal decomposition and claimed that it was due to the internal stresses induced by the spinodal decomposition that could hinder the migration of dislocation, analogous to the influence by precipitation hardening. More importantly, Cahn claimed that the hardening extent should be proportional to the square of the amplitude during spinodal decomposition.

With the development of the theory of spinodal decomposition by Hillert, Cahn, and Hilliard [56], [59], the ‘475 Embrittlement’ in Fe-Cr alloys has gradually drawn a lot of attention. Since the 1960s, different techniques have been applied to study phase separation in the binary system of Fe-Cr. For instance, in 1971, Chandra & Schwartz [60] employed Mössbauer spectroscopy to investigate the phase separation in Fe-60Cr alloys according to the fact that an absorption peak occurs in the paramagnetic environment, which corresponds to the Cr-rich domains. In 1978, Okada et al. [70] used transmission electron microscopy (TEM) to visualize the morphology of phase separation. In the 1980-90s, Miller et al. [71]–[73] and Brenner et al. [74], [75], successively employed atom probe field ion microscopy (APFIM) and atom probe tomography (APT) to study the morphology of the phase separation in ferritic steels.

In the 1990s, Danoix et al. [4], [21] studied the relations between the hardness increase and the amplitude of phase separation during aging by atom probe tomography, and found that the hardness increase has a positive correlation with the amplitude of the phase separation that is represented by variation ( $V$ ) values. The experimental results are good evidence of the theory proposed by Cahn (Cahn, 1963)

for the hardening mechanism by spinodal decomposition. This confirms that the spinodal decomposition is the main source of embrittlement. The hardening is attributed to the increase of elastic strain due to the crystallographic misfit between the forming  $\alpha$  and  $\alpha'$  domains. Recently, scientists [15] have investigated the hardening mechanism by hardness test and APT analysis. They compared the hardness increase with the size of  $\alpha'$  and composition amplitude of phase separation, respectively, and concluded that the hardness increase is more related to the composition amplitude instead of the size of  $\alpha'$ . Some other concurrent phenomena have also been reported to be responsible for the embrittlement, such as Cu clusters and G-phase precipitates. Intermetallic precipitations between the domains further increase the embrittlement. However, it is difficult to deconvolute the individual effects on hardness.

#### 2.4.2 Analyzing Kinetics – time exponents

At the late stages of spinodal decomposition, the domains approach their equilibrium compositions. The driving force for further decomposition is the reduction of interfacial area between the domains, since these are associated with high surface energies. As the domains coarsen, the curvature smoothens, thus decreasing the interfacial area. For materials with low volume fraction of particles, the larger particles will grow at the expense of smaller ones, by Ostwald ripening. As decomposition proceeds, the rate of growth of the particles slows. The LSW law predicts the power law growth of the mean precipitate size as  $d(t) \propto t^{1/3}$ . In the LSW formulation, the only method of interface motion or particle growth is by long range diffusion across the matrix. Systems with interconnected microstructures have

long range diffusion coupled with diffusion along the interface. To date, neither a growth law nor a scaling formula has been derived directly for the case when both of these mechanisms occur simultaneously. Several researchers have assessed numerical models based on the Cahn-Hilliard-Cook equation and there is general agreement that the late stage development of scale fits a power law. They found that at later times, the domains coarsen with a time exponent of  $\frac{1}{3}$ . Another study [40] found that the scaling exponent increased continuously from  $\frac{1}{4}$  to  $\frac{1}{3}$  with increasing time. The change in the exponent was interpreted as originating from a crossover from the interfacial to bulk diffusion mechanisms.

Pareige et al [40] reported the wavelength evolution of Mo-free grade CF-3 had a power law time exponent of 0.07, which is a very low value with respect to both classical exponents for spinodal decomposition and values observed for Mo-bearing steels. Low values between 0.078 and 0.097 were also reported by Hamaoka et al. [5], [76] in a Mo-bearing steel at different temperatures. Scientists agree that the effective time exponent is strongly related to the diffusion mechanism and the evolution of the domain size of an interconnected structure must evolve gradually with time, depending on the relative weight of interface diffusion and bulk diffusion. They claim that alloying can affect the driving force, but is not expected to modify the effective time exponent but rather the time constant [3], [40]. However, this statement is confusing because driving force, the free energy, is a thermodynamic term, while the activation energy is a kinetic term that describes the high energy of the barrier. In the equation  $d = Kt^n$ , the time exponent is  $n$  and the constant of

proportionality is  $K$ , which is temperature dependent and can be used to find the activation energy.

#### 2.4.3 Analyzing Kinetics – change in mechanical properties

The ‘apparent’ activation energy for the process of embrittlement has been derived by Chopra [2] from Charpy tests and described as a function of the chemical composition of the cast material. From the equation,  $Q \left( \frac{\text{kJ}}{\text{mol}} \right) = 10 [74.52 - 7.20 \theta - 3.46 Si - 1.78 Cr - 4.35 I_1 Mn + (148 - 125 I_1) N - 61 I_2 C]$ , where  $I_1 = 0$  and  $I_2 = 1$  for CF-3 and CF-8 steels, composition is in wt. %, and  $\theta$  varies from 2.5 to 3.3 with service temperature from high to low, respectively, the ‘apparent’ activation energy,  $Q$ , ranges between 65 to 250 kJ/mol. These values can be significantly lower than the activation energy of diffusion for metallic species. The lower values of the activation ‘apparent’ energy from Charpy tests were interpreted to be due to other factors, such as carbides at the phase boundaries or G-phase precipitation in ferrite, all of which may change the fracture mechanism of the aged material. For instance, precipitation of large carbides or nitrides at phase boundaries can initiate phase boundary separation by particle cracking. Consequently, a lower degree of spinodal decomposition is needed for a given change in mechanical properties. Therefore, according to Chopra [2], an alloy with carbides would exhibit a faster reduction in impact strength relative to a material without phase boundary carbides.

#### 2.4.4 Relating Microstructural Changes to Mechanical Properties

Thermal aging of CDSS materials at reactor operating temperatures increases their hardness and tensile strength; decreases ductility, impact strength, and fracture toughness; and shifts the Charpy transition curve and the ductile-to-brittle transition temperature to higher temperatures. Microstructural changes due to thermal aging leads to (a) spinodal decomposition of the ferrite into high-Cr  $\alpha'$  and low-Cr  $\alpha$  regions; (b) nucleation and growth of Ni- and Si-rich G-phase precipitates in the ferrite phase; and (c) precipitation and/or growth of  $M_{23}C_6$  carbides at ferrite/austenite phase boundaries. The formation of Cr-rich  $\alpha'$  regions in the ferrite is regarded as the primary mechanism for thermal embrittlement.

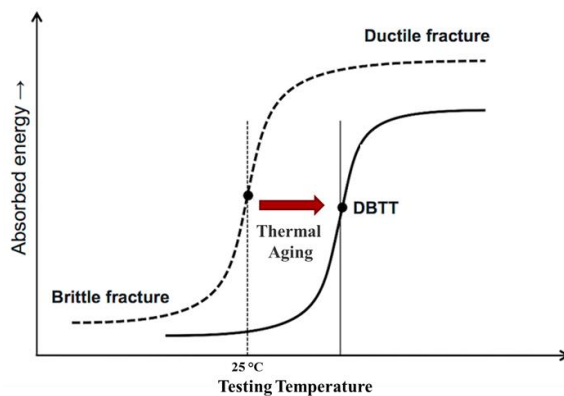


**Figure 8.** Transition of ductile to brittle fracture mode due to thermal aging. Adapted from [77].

Charpy testing at higher temperatures results in higher ductility due to easier motion of dislocations. However, thermal aging results in lower ductility due to precipitation of embrittling phases. Alloying elements play a role in forming precipitates, and therefore influences the ductility of steels.

The  $\alpha'$  phase strengthens the ferrite matrix and increases strain hardening. The G-phase and carbides at phase boundaries also contribute to a brittle failure by phase boundary separation, and may facilitate cleavage of the ferrite by particle cracking. While phase

The formation of G-phase precipitates is expected to harden and embrittle the ferrite phase by acting as Orowan obstacles that impede the glide of dislocations. However, studies since 1990s report inconsistent results, and the role of G-phase precipitates in the embrittlement of ferrite is still unclear due to the significant overlap of the two phase transformations. Spinodal decomposition is suggested to accelerate the G-phase precipitation by ejecting Ni and Si diffusion flux across the  $\alpha/\alpha'$  domain interfaces. Mutual influences between spinodal decomposition and G-phase complicate the analysis of the ferrite embrittlement.

On one hand, APT studies show that the hardening of ferrite is fully correlated to the Cr amplitude of spinodal decomposition, and not affected by the precipitation of G-phase. Pareige et al [3] plotted hardness versus the G-phase number density up to an aging time of 200,000 h for CF-8M. The hardness values did not change as the number density increased during growth and decreased during coarsening. On the other hand, the mechanical properties of CDSS with spinodal decomposition and G-phase precipitates have higher strength than Fe-Cr-Ni alloys with only spinodal decomposition but no G-phase precipitates [78]. The precipitation of G-phase can influence the kinetics of embrittlement by either directly altering the kinetics of spinodal decomposition or changing the deformation and fracture behavior of the ferrite matrix and thereby influencing the effectiveness of spinodal decomposition. The G-phase precipitates may also alter the frequency or spacing (wavelength) of Cr fluctuations.

The kinetics of G-phase precipitation depends on the chemical composition of the cast material. In general, it is accepted by many scientists [25], [79] that the

higher C content, molybdenum-containing CF-8M has a higher precipitation of G-phase and faster embrittlement times than Mo-free alloys. Chopra [28] compiled data from many types of CDSS, including CF-8M, and plotted the average times and temperature for a given decrease in the Charpy-impact energy. The impact energy values varied significantly for the various alloys. Most alloys required  $\geq 10,000$  h at  $400^{\circ}\text{C}$  and  $\geq 30,000$  h at  $350^{\circ}\text{C}$  before G-phase precipitates are detected by TEM or SANS. At  $400^{\circ}\text{C}$ , there was an 80 % reduction in impact energy before G-phase was detected in any of the alloys. However, at  $320^{\circ}\text{C}$ , G-phase was detected before 80% reduction in toughness. These results may indicate that the influence of G-phase precipitation on embrittlement would be greater compared to spinodal decomposition at lower temperatures in the long-term.

G-phase precipitates have been observed on the interdomains of spinodal decomposition by virtually all researches studying thermal aging. However, researchers studying the effect of stress or irradiation on DSS have observed that G-phase could form in the absence or lesser extent of spinodal decomposition [31], [53]. G-phase precipitated readily on dislocations of pre-stressed materials because it is a favorable site of nucleation to lower the free energy of the system and it is also a high diffusivity path favorable for transporting the G-phase elements. In irradiation studies, voids form in the matrix, facilitating faster diffusion. The samples from Chopra's manuscript [28] were taken from decommissioned nuclear plants. Therefore, the contribution of thermal, pressure stress, and irradiation cannot be ruled out.

It must be emphasized that APT does not give crystallographic structure but only composition. APT can detect minute agglomeration of atoms before they crystallize. Therefore, it is likely that small Ni-, Si-, and Mn-enriched particles observed in APT are in fact precursors, or G-phase forming zones. The only way to conclude on this point would be to characterize the structure of these small precipitates by TEM. Comparing G-phase kinetics by different methods, TEM or APT, could lead to different answers if the stage of the G-phase formation is not defined clearly.

#### 2.4.5 Non-uniform kinetics

In the thermally aged CF-8 specimen,  $M_{23}C_6$  carbides, G-phase precipitates, and  $\alpha'$  phase were observed. Carbides were located at the heterophase boundary. Chen et al [53] showed that  $M_{23}C_6$  carbides decorated the ferrite-austenite phase boundary in an unirradiated aged CF-8 specimen. An apparent distinction of the size and density distribution of G-phase was observed between the case with and without carbides. The G-phase precipitates close to the carbides were large as 6-7 nm. The large sizes and higher volume fraction of the G-phase precipitates observed near the carbides in CF-8 may be understood as an enrichment of elements such as Ni, Si, and Mn near its vicinity, which are ejected from the  $M_{23}C_6$  carbide. For the case of a phase boundary without the presence of carbides, the density of G-phase precipitates increased monotonically with increasing distance from the phase boundary while the size remained constant as 3 nm. The low density of G-phase precipitates in the vicinity of a phase boundary without carbides was suggested by Zhang et al [80] to be caused by a solute depletion zone of Ni. The TEM measurements of G-phase

precipitate distributions in ferrite of aged CF-3M by Hamaoka et al [5], [76] are included for comparison. The CF-3M steels have similar duplex structure but different chemical compositions from the CF-8 steels. The lower carbon content in CF-3M results in an absence of carbides at the ferrite-austenite phase boundary. An inhomogeneous distribution of G-phase precipitates was also observed in CF-3M. The size and number density of the G-phase precipitates increased further away from the heterophase interface.

Zhang et al [80] studied the ferrite/austenite interface of a CF-8 equivalent alloy by APT. They reported that Ni, Si, Mn, Mo, Cu, P, C, and B elements segregated to the heterophase interface, thereby creating a nickel depletion zone (NDZ) in the ferrite phase of about 30 nm. The inhomogeneous distribution of G-phase in the ferrite of thermally aged CF-8 further complicates the analysis.

## Chapter 3: Experimental Procedures

The following chapter outlines the mechanical testing procedures of Vickers microhardness and Charpy impact tests, and characterization techniques, including: optical micrography, Scanning Electron Microscopy (SEM), Scanning/Transmission Electron microscopy (S/TEM), and Atom Probe Tomography (APT).

The steels investigated in this study were obtained from Monett Company, Inc. as 17.8 cm × 3.3 cm × 2.9 cm rectangular keel blocks cast to the CF-3 and CF-8 standard specification outlined by ASTM A351-12b. All blocks of each steel type were cast from the same melt followed by a solution treatment at 1065 °C (1338 K) for 2 h and quenched in water at room temperature in accordance with the ASTM standard.

The nominal chemical composition of the two steels as measured by optical emission spectroscopy (OES) is provided in Table 2. The composition of Cu, P, and B were not reported from the foundry, but were detected by Atom Probe Tomography during analysis. The elements Niobium (Nb) and Nitrogen (N), which are often found in steels, were not reported or detected.

**Table 2.** Composition of CF-3 and CF-8 alloys

Steel		Composition (wt.%)						
		Fe	Cr	Ni	Si <sub>max</sub>	Mn <sub>max</sub>	Mo <sub>max</sub>	C <sub>max</sub>
CF-3	ASTM A351	Balance	17.0–21.0	8.0–12.0	2.00	1.50	0.50	0.03
	Unaged	69.52	19.69	8.40	0.98	1.07	0.28	0.02
CF-8	ASTM A351	Balance	18.0–21.0	8.0–11.0	2.00	1.50	0.50	0.08
	Unaged	69.44	19.85	8.30	0.97	0.99	0.35	0.06

\* Measured by Optical Emission Spectrometry

### 3.1 Mechanical Properties

A variety of mechanical tests are conducted to understand the stress-strain behavior. The material property is the response to an external force. Toughness is the capability of absorbing energy before fracture and hardness is the resistance to plastic deformation. Plastic deformation is an irreversible deformation of a material that prevents it from returning to its original state when the stress is removed. Standard tests, defined by ASTM, were followed to measure the material properties.

This chapter describes the mechanical experimental techniques used in the present investigation.

#### 3.1.1 Vickers Micro-Hardness (HV)

Specimen blanks were mechanically reduced and cold mounted in epoxy for metallographic specimen preparation. The mounted specimens were ground and polished to 0.3  $\mu\text{m}$  surface finish employing standard procedures. The polished specimens were tested using an Instron Tukon 2100 tester with a Vickers microhardness indenter, a load of 500 g, and dwell time of 15 s in accordance with the ASTM E384-11 standard procedures. The average of ten measurements was reported and the  $\pm 2\sigma$  errors were based on the standard error of the mean.

The Vickers micro-hardness measurements were calculated by dividing the parameters of load force (F) over the area of the indent diagonals ( $d_1$  and  $d_2$ ). Normally, the Vickers micro-hardness is expressed as a number without units. To report HVN in SI units, multiplying by the universal gravitation acceleration will convert from  $\text{kgf/mm}^2$  to  $\text{N/m}^2$  or Pa.

### 3.1.2 Charpy V-notch Impact Toughness (CVN)

The CVN specimens were fabricated in accordance with the ASTM E23-12c standard from the specimen blanks. The 55 mm × 10 mm × 10 mm CVN specimens were tested employing a Tinius Olsen IT406 test frame at room temperature following the ASTM standard test procedures. The absorbed impact energy was measured and fracture morphology was observed by microanalysis for each specimen. The average of two or three measurements is reported for each aging condition, and the reported errors are based on the standard error of the mean.

### 3.2 Characterization Techniques

In the world of microscopy and microanalysis, a single atom or molecule defines the ultimate length scale. It is a challenge to simultaneously image a single atom and identify its chemistry. There has been a steady advancement in the development of microscopy and microanalysis. Transmission electron microscopy (TEM) has fully exploited the physics of electron optics to reduce aberrations associated the lenses in order to achieve sub-angstrom resolution. Atom Probe Tomography (APT) represents a revolutionary characterization tool for materials that can image and chemically identify hundreds of millions of individual atoms in three dimensions, a major advancement over the two dimensional images of other microscopy techniques. The APT has origins in the field-ion microscope (FIM) that removes atoms from a specimen's surface by field evaporation or laser pulsing in a controlled manner and then sequentially identifies them with a time-of-flight (TOF) mass spectrometer. APT provides the highest spatial resolution of any microanalysis technique [81]. This capability provides a unique opportunity to study chemical

clustering and 3-D distributions of atoms experimentally with atomic resolution. Due to the similarities in lattice parameters of the  $\alpha$  and  $\alpha'$  domains in spinodal decomposition and the small mass difference between iron (56 a.m.u) and chromium (52 a.m.u), it is difficult to study spinodal decomposition wavelength quantitatively with a conventional TEM. Instead, APT has proven to be feasible for this study.

In 1955, Müller developed the prototype of Field Ion Microscopy (FIM) and successfully applied field emission to image atoms for the first time. This new type of microscope was the starting point for the development of atom probe tomography [81]. During field evaporation, the atom with the charge of  $n$  on the surface of the specimen is accelerated up by the applied field. Thus, the potential energy of  $neV_e$  is converted into kinetic energy of  $\frac{1}{2}(mv^2)$ . Therefore, the mass-to-charge ratio  $m/n$  of the evaporated ion can be given by:  $\frac{m}{n} = 2eV_e \left(\frac{t}{d}\right)^2$ , where  $e$  is the charge of an electron,  $d$  is the distance between the specimen and the detector,  $V_e$  is the applied voltage, and  $t$  is the time of flight from the specimen tip to the detector as depicted in Figure 9(a).

In the 1980s, the 3-dimensional (3-D) atom probe instrument was developed to be able to produce three-dimensional images of the internal structures by adding a position-sensitive detector. With the application of a reflectron lens, the mass resolution improved and can easily identify the isotopic atoms, as shown in Figure 9(b), in which different isotopic peaks can be evidently separated, such as Fe, Cr, Ni from the spectrum of the CF-3 alloy.

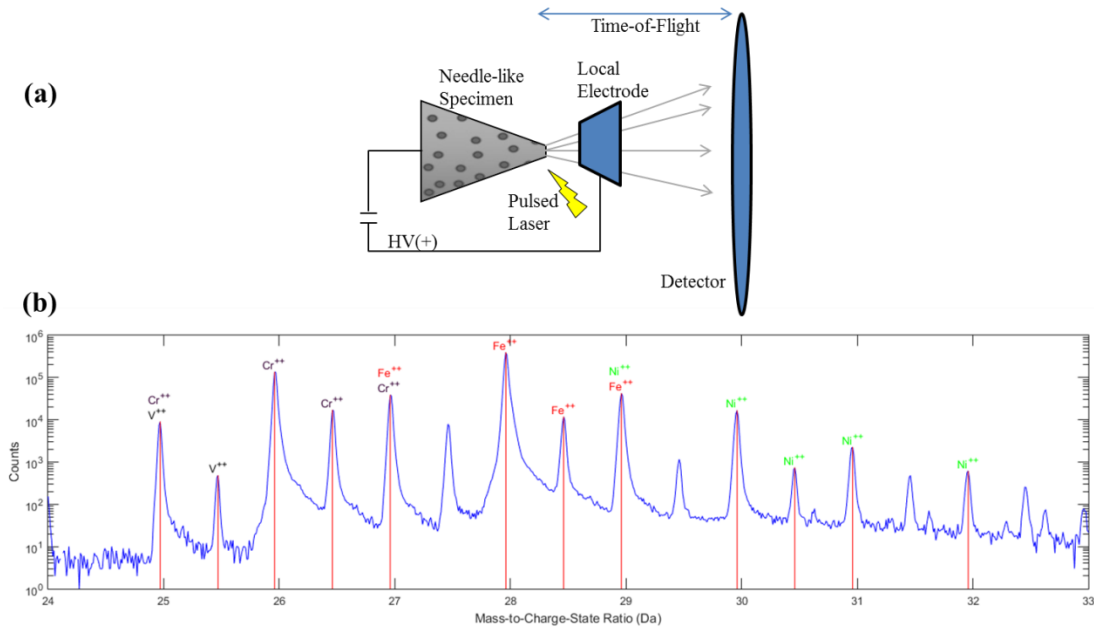


**Figure 9.** (a) Time of flight mass spectrometry, (b) ranging of mass spectra. Adapted from [81].

Today's atom probe tomography instrument is the local electrode atom probe (LEAP) by the company of Imago Scientific Instrument (now CAMECA). The first generation of commercial LEAP was constructed by Kelly and Larson [82].

### 3.2.1 Optical Microscopy

This technique has a wide range of resolution from millimeters to micrometers. Bulk fractography images of the broken Charpy impact specimen were taken with a Canon camera. Metallography was performed employing a Buehler® ViewMet Inverted Metallograph. The metallographic specimens were etched with Kalling's reagent No. 1 following standard procedures at room temperature to reveal the dual-phase microstructure.

The volume percentage (fraction) of the ferrite and austenite phases in the microstructure were determined employing three different methodologies: (1) manual

point counting in accordance with the ASTM E562-11 standard, (2) digital counting of pixels using the Image-J software in accordance with the ASTM E1245-03 standard, and (3) the Schoefer diagram based on composition in accordance with the ASTM A800-14 standard. The percentages determined by the first two methods were measured by utilizing 20 optical micrographs from each of the steels as specified in the standards.

### 3.2.2 Scanning Electron Microscope (SEM)

The scanning electron microscope (SEM) in the present investigation was used for three purposes: examining fracture surfaces of charpy impact specimen at the micro-level; Energy Dispersive Spectroscopy (EDS) mapping of chemical partitioning; and site-specific sample preparation by FIB.

Imaging of fractography surfaces and EDS mapping were done by a Hitachi S-3400 Variable Pressure (VP) scanning electron microscope (SEM) instrument equipped with a Bruker QUANTAX XFLASH 4010 energy dispersive spectrometer (EDS) at 15 kV. Elemental maps at  $\delta$ -ferrite/ $\gamma$ -austenite heterophase interfaces were acquired for 1200 s at 15 kV and low probe current. The National Institute of Standards and Technology (NIST) Desktop Spectrum Analyzer (DTSA-II) program was employed to generate theoretical spectra based on the CDSS nominal composition to validate that no extraneous peaks were present in the experimental spectra. The elemental concentrations of the individual phases were derived from the integrated counts of the spectra. Elemental concentrations were quantified with the Bruker software using a peak-to-background (P/B) ratio analysis with atomic number (Z), x-ray adsorption (A), and x-ray fluorescence (F) matrix effect corrections. A

mathematical series fit in the Bruker software was used for background subtraction in the experimental SEM-EDS spectra. Overlapping peaks, such as the Mn  $K_{\alpha}$  peak at 5.984 keV with the Cr  $K_{\beta}$  peak at 5.947 keV and the Mn  $K_{\beta}$  at 6.49 keV with the Fe  $K_{\alpha}$  at 6.40 keV were deconvoluted in the Bruker software. The mean  $\pm 2\sigma$  errors were reported.

Scanning electron microscope/focused ion beam (SEM/FIB) observations were performed at the Pacific Northwest National Laboratory (PNNL), employing a FEI Helios Nanolab 600 dual beam instrument at 5 keV. Specimens with a needle-shaped geometry necessary for APT analysis were fabricated using a FEI Helios Nanolab 600 dual-beam SEM/FIB instrument following standard lift-out and sharpening procedures [29, 30]. The *in situ* site-specific specimen preparation technique was performed on the metallographic mounts to take APT specimen blanks from  $\delta$ -ferrite/ $\gamma$ -austenite heterophase interfaces, Figure 10. To create the needle-shaped morphology necessary for APT analysis, annular milling was performed employing a 30 keV gallium ion ( $\text{Ga}^+$ ) beam and sequentially decreasing probe currents following standard procedures after transfer of the region of interest (ROI) to the silicon (Si) microtip post with an Omniprobe micromanipulator [31]. As a final step, a low voltage ion beam of 2 keV was allowed to raster over the specimen tip to remove material that had been damaged by the 30 keV  $\text{Ga}^+$  ion beam annular milling operation [30]. The final apex of the specimen tips, imaged by SEM using 5 keV, had radii of about 50 nm, which is suitable for APT analysis.

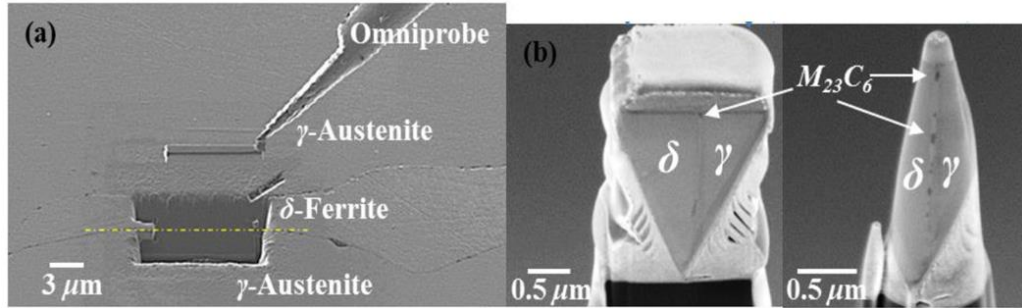


**Figure 10.** *In situ* site-specific specimen preparation technique on the Focused Ion Beam (FIB): (a) After milling, extracted sample with an omniprobe; (b) Attached sample on a post; (c) sharpened sample to sub-100 nm tip.

### 3.2.3 Scanning/Transmission Electron Microscope (S/TEM)

The scanning/transmission electron microscope (STEM/TEM) in the present investigation were performed by microscopists at the FEI Company in Portland, Oregon and by Mr. Schwarm at the University of Maryland (UMD), College Park. In FEI, Bright field (BF) and high angle annular dark field (HAADF) micrographs were obtained in STEM mode on a Talos F200X equipped with XFEG and Super-X EDS technology. At UMD, a JEOL 2100 LaB6 TEM instrument operating at 200 kV and a JEOL 2100 field emission gun (FEG) TEM instrument operating at 200 kV and equipped with an Oxford INCA 250 X-ray energy dispersive spectrometer (EDS) were employed to study the microstructural evolution.

#### *TEM specimen preparation:*

TEM requires electron transparent specimens with a typical thickness around 100 nm for electron transparency. There are several techniques to prepare TEM specimens, including ion milling and jet-polishing.

At FEI, the specimen for STEM imaging was prepared using Helios Plasma Dual Beam FIB. The process was the standard FIB prep process, thinning with 30 kV for the bulk of the milling then final polishing with 5 kV to minimize sample damage.

At UMD, the specimens were punched from a mechanically thinned foil sample of approximately 200  $\mu\text{m}$ . The foils were single-jet electropolished in 10 vol% perchloric acid ( $\text{HClO}_4$ ) solution in acetic acid ( $\text{CH}_3\text{COOH}$ ) at 0  $^\circ\text{C}$  and 20 V for 10 min. The foils were then subsequently ion-beam milled at a  $10^\circ$  milling angle, 5 kV, and 3 mA until perforation in a Fischione Model 1010 milling system [83].

#### *TEM analysis:*

The selected area electron diffraction (SAED) technique was used to identify the  $\delta$ -ferrite,  $\gamma$ -austenite,  $\text{M}_{23}\text{C}_6$  carbide, and G-phase precipitates in the foils. The TEM images and SAED patterns were analyzed using the Gatan Digital Micrograph Microscopy Suite software.

#### 3.2.4 Atom Probe Tomography (APT)

A CAMECA Local-Electrode Atom Probe (LEAP<sup>®</sup>) 4000X instrument in the HR configuration, equipped with a reflectron for high mass resolution, was used for APT analysis at PNNL. The specimen tip base temperature during data acquisition was set at 40 K. There are two kinds of analysis modes in LEAP, i.e. voltage mode and laser mode. Only conductive materials can be analyzed in the voltage mode and laser mode is used for non-conductive materials, such as ceramics. Some CF-8 samples with carbides were analyzed by laser mode with an energy of 30 pJ. In most samples, a voltage pulsed mode was applied to the specimen tips with a pulse-to-standing DC voltage ratio of between 15% and 20% at a pulse frequency of 200 kHz

to promote field evaporation. The evaporation rate was maintained at a constant 1.5% rate or 0.015 ions per pulse. The background pressure was  $\sim 1.6 \times 10^{-11}$  Torr ( $2.1 \times 10^{-9}$  Pa). A low pulse fraction range resulted in a lower probability of tip fracture, low background noise signal, and low incidences of multiple hits. Data sets of greater than four million ions were collected for each specimen tip, which corresponds to analysis depths of 60 nm to 120 nm depending on the tip radius. For each APT needle, the atom probe continued to collect atoms until the maximum voltage is reached or a major specimen fracture occurred. Multiple APT needles were analyzed for each condition to verify data reliability and consistency. However, in APT, the sample size of acceptable tips for statistical purposes is usually limited.

The APT was used to study the microstructural evolution in DSS. The procedures of specimen preparation and data collection are described below.

#### *APT – sample prep*

Focused ion beam (FIB) milling was used to prepare specimens for APT as described in the SEM section.

#### *APT – sample reconstruction*

Data reconstruction and analysis were performed using the CAMECA Integrated Visualization and Analysis Software (IVAS), version 3.6.8. The APT specimen tips were reconstructed with a radius evolution defined using the tip profile morphology from SEM micrographs taken before APT analysis. Overlapping iron (Fe) and chromium (Cr) mass peaks at an m/n ratio of 54 were deconvoluted based on isotopic abundances.

#### *APT – data analysis*

Three analysis techniques were performed: isoconcentration surfaces, proximity histogram (proxigram), and 1-D concentration profiles. The fundamentals of these techniques are described individually below. APT artefacts such as crystallographic poles, where preferred evaporation along certain directions may lead to high density regions, were removed.

### 1) Isoconcentration surface analysis

The G-phase precipitates and Cr-riched  $\alpha'$  domains were visualized with the use of isoconcentration surfaces, or isosurfaces for short. An isosurface is a surface of designated concentration in three dimensions. In order to make comparison among specimens of various aging conditions and local chemical environments, a single or small range of Ni and Cr concentration were used to define the G-phase and  $\alpha'$  precipitates, respectively.

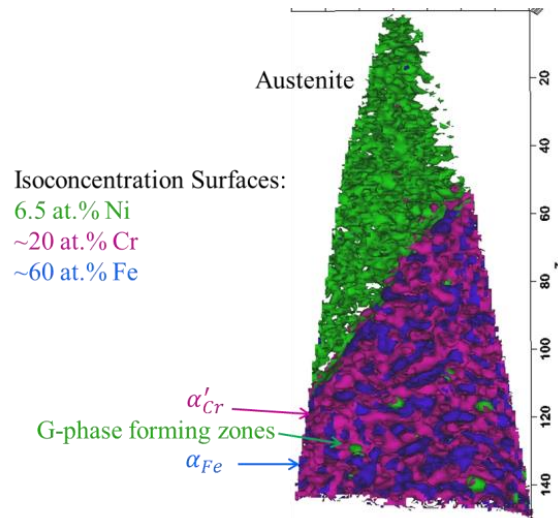


**Figure 11.** Fe, Cr, and Ni Isoconcentration surfaces to illustrate respective phases.

One purpose of using isosurfaces was to delineate an interconnected morphology and plot the element rich and poor regions in a proximity histogram

(proxigram) described below. The element rich region of the curve will indicate the concentration in the Ni-rich G-phase or Cr-rich  $\alpha'$  spinodal decomposition domain. In this study, ~2.7 at. % Ni and ~20 at. % Cr concentrations were used because they are within the average composition of the ferrite and would therefore have the largest network of isosurface concentration as shown in Figure 11.

Another purpose of using isosurfaces was to measure the size and number density of G-phase precipitates defined by the isosurfaces. A concentration of 6.5 at. % Ni is above the average composition in the ferrite phase and suitably reveals the Ni-rich precipitates. The G-phase precipitates in the APT reconstructions were delineated by 6.5 at. % Ni isoconcentration surfaces. The precipitates well inside the ferrite were counted as full, while those located at the edges were counted as half. Information of all the precipitates surface area, volume of enclosed bodies, and location are provided by IVAS. The volume of the ferrite phase was estimated by the number of ranged atoms in the mass spectra. The precipitate volume equivalent sphere radii,  $\langle R \rangle$  [84], number density,  $N_v$ , volume percentage (fraction),  $V_f$ , and core compositions are reported. The estimated steel density,  $\rho$ , is  $8.46 \times 10^{22}$  atoms  $\text{cm}^{-3}$ , which was used to calculate the reconstructed volumes of the APT specimen tips [84] and the estimated detection efficiency,  $\eta$ , is 36% for this atom probe instrument.

The G-phase core compositions of the largest precipitate were derived from the four data points on the right hand side of the proxigram concentration profiles. However, the composition from an average of all precipitates could not compile

correctly due to a wide variation of sizes. Therefore the G-phase composition of the entire ferrite was measured with ~2.7 at. % Ni isosurface as described above.

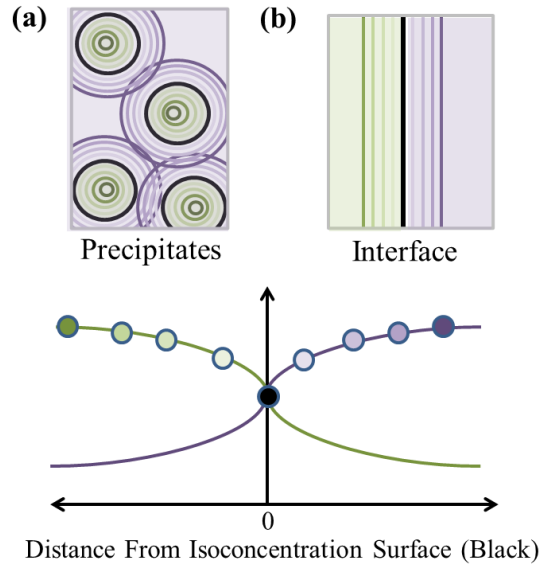


**Figure 12.** Generating proximity histogram plot from: (a) particles with an isoconcentration delineated by the black circular surface, and (b) interface delineated by the black linear surface

## 2) Proximity histogram (proxigram) analysis

A proxigram was used to study the Ni and Cr concentration profile along the distance normal to their respective surfaces. A proxigram is generated by plotting a one-dimensional profile of local concentration versus the proximity to the isosurface as shown in Figure 12. Although a 1-D concentration profile of a single precipitate could also be acquired by using the region of interest (ROI) across the precipitate boundary, the boundary curvatures of the G-phase precipitate and  $\alpha'$  domains were high due to the small sizes of 1-3 nm for ROI method to appropriately capture the composition.

## 3) 1-D concentration profiles

The samples were extracted by rectangular regions of interest (ROI) within the ferrite phase. From these ROIs, concentration profiles were plotted to measure wavelengths and amplitudes by the following procedures: Auto-correlation Functions (ACF), Larson-Bar-on-Miller (LBM), and sinusoidal curves in-lab method. Twenty ROIs of dimensions 3.2 nm by 3.2 nm by 30 nm were chosen randomly in the ferrite phase as shown in Figure 13.

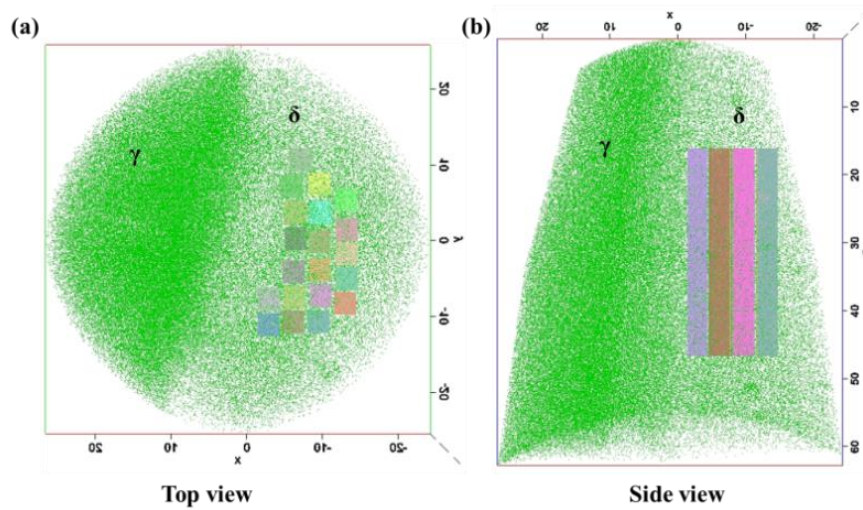


**Figure 13.** 20 ROI's in the ferrite phase (a) top view, (b) side view).

## Chapter 4: Analytical Procedures

This chapter outlines the analysis performed to study phase separation kinetics. For spinodal decomposition, the wavelengths and amplitudes were measured by three techniques: Auto-correlation Function (ACF), Larson-Bar-on-Miller (LBM), and the in-lab method using sinusoidal curves. This chapter also explains how the G-phase forming zones were delineated to measure the radius, number density, and volume fraction. Kinetic analysis was performed by finding time exponents based on the LSW theory. More accurate techniques were successfully developed to describe the Degree of Decomposition (D.o.D) and measure the activation energy to find the diffusion mechanism. Lastly, fitting functions of the form of hyperbolic tangent equations were used in interpolating data at shorter times and extrapolating data within a short range.

### 4.1 Spinodal Decomposition

The extent of spinodal decomposition can be quantified by measuring the wavelength and amplitude changes during thermal aging.

#### 4.1.1 Auto-Correlation Function Method (ACF)

Based on the 1D concentration-field data with a fixed bin width of 0.2 nm, the auto-correlation function (ACF) was employed to evaluate the spinodal decomposition wavelength [72]. The correlation coefficient from autocorrelation function is expressed in the following equation [Brenner et al., 1984]:  $R_k = \frac{1}{\sigma^2} \sum_{r=0}^{r_{max}-k} (C_i - C_o)(C_{i+k} - C_o)$ , where  $C_i$  and  $C_{i+k}$  are the concentrations of the  $i^{th}$  and  $i + k^{th}$  sample blocks;  $C_o$  is the average composition;  $k$  is the lag;  $\sigma^2$  is the

variance of the composition of  $C_i$ , given by  $\sigma^2 = \sum_{i=1}^N (C_i - C_o)^2$ . The ACF obtains the curve of correlation coefficient to find the first maximum, which is corresponding to the wavelength of phase separation, as shown in Figure 14. The  $k^{th}$  term depends on the bin size of the data. With a bin size of 0.2 nm, the conversion of  $k$  to the wavelength,  $\lambda$  is  $\lambda = 0.2(k - 1)$ . From Figure 14, the wavelengths, as marked by a red dot, at 4300 to 17200 at 400 °C are 3.6 nm, 3.8 nm, 6 nm, and 6.4 nm. Note that these values are not averaged and represent only one of the 20 ROI's per sample.

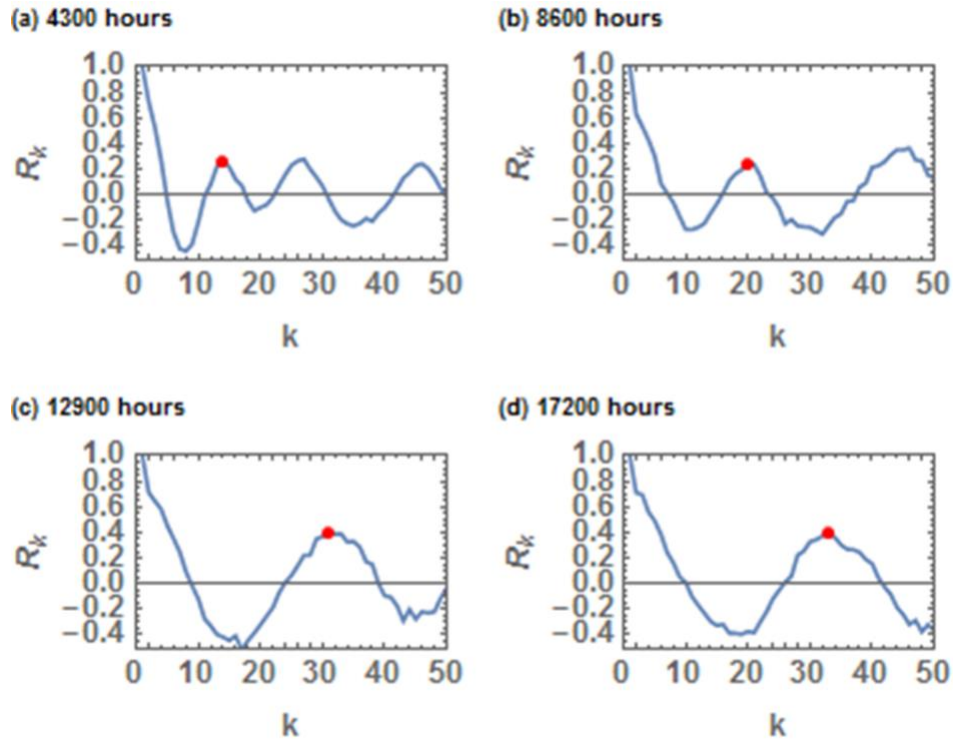


**Figure 14.** Auto-Correlation Function method illustrating how the wavelength is derived from the plot. The plots are derived from CF-3 samples aged at 400 °C to (a) 4300 hours, (b) 8600 h, (c) 12900 h, and (d) 17200 h

#### 4.1.2 Larson-Bar-on-Miller Method (LBM)

There are several methods to measure spinodal amplitude: Variation method (Blavette et al., 1988), Pa method (Sassen et al., 1987; Godfrey et al., 1988; Brown et

al., 1990) and RDF method (Zhou et al., 2013). The LBM method is currently the most widely used method to obtain the amplitude of phase separation. This method is based on the compositional frequency generated by using an ROI with fixed sample count. The binomial distribution represents the ideal distribution in a homogenized alloy. Once the phase separation proceeds, the peak of the distribution becomes lower and the width at the bottom of the distribution becomes wider since two phases with high Fe and Cr contents, respectively, occur.

Since the alloy is decomposed to Fe-rich phase ( $\alpha$ ) and Cr-rich phase ( $\alpha'$ ) during aging, the idea of the LBM method is to deconvolute the frequency diagram into two Gaussian distribution functions where one is for the Fe-rich phase ( $\alpha$ ) and the other is the Cr-rich phase ( $\alpha'$ ). The deconvolution of the frequency diagram is based on [73]:

$$\rho(x) = \frac{1}{(2\pi * \sigma^2)^{1/2}} * \left\{ \frac{\mu_2}{\mu_1 + \mu_2} * \exp\left(-\frac{(x - \mu_1)^2}{2\sigma^2}\right) + \frac{\mu_1}{\mu_1 + \mu_2} * \exp\left(-\frac{(x - \mu_2)^2}{2\sigma^2}\right) \right\}$$

where  $\mu_1$  and  $\mu_2$  are the peak and trough compositions, respectively,  $\sigma^2$  is the variance of the Gaussian distributions, and  $x$  is the composition. Therefore, the amplitude can be obtained by the subtraction between  $\mu_2$  and  $\mu_1$  as depicted in Figure 15. In Figure 15, the trough compositions are plotted in blue, the peak compositions are plotted in green, and the sum of the two Gaussian distribution are plotted in red. The red plot has two distinct peaks, which are spreading apart as the temperature increases, representing the amplitude. The amplitude for the 17,200 hour aged sample from 280 °C to 400 °C are 6.9 at. % Cr, 8.4 at. % Cr, 11.0 at. % Cr, and 13.3 at. % Cr. Note that these peak-to-trough amplitude values are not averaged and represent only one of the 20 ROI's per sample.

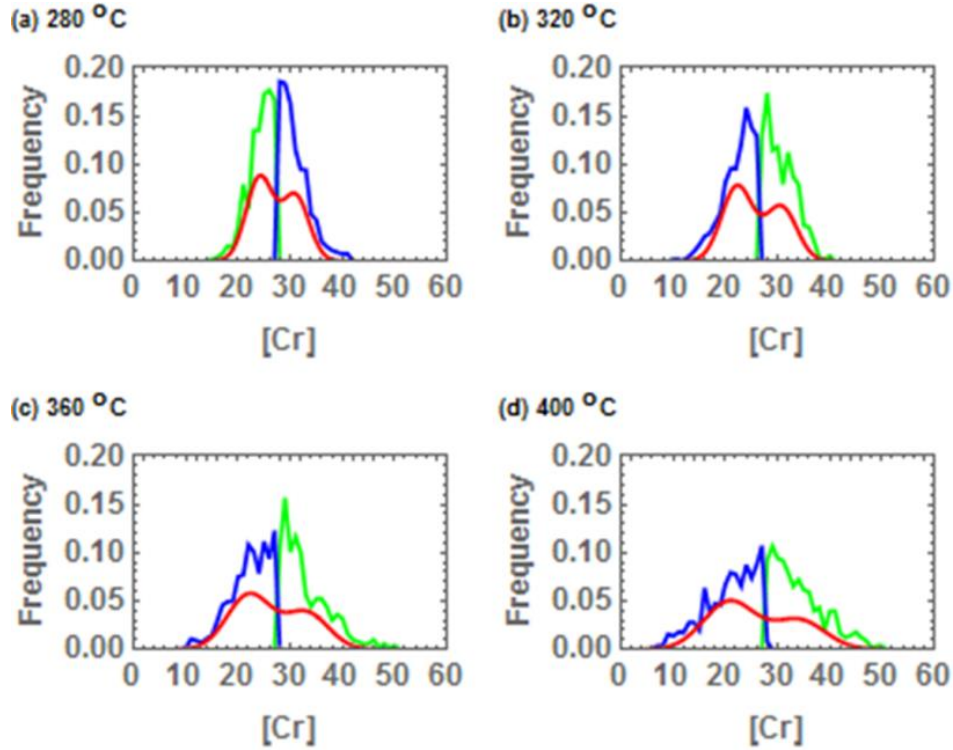


**Figure 15.** Langer-Bar-on-Miller (LBM) method illustrating how the amplitude is derived from the plot. The plots are derived from CF-8 samples aged to 17200 hours at (a) 280 °C, (b) 320 °C, (c) 360 °C, and (d) 400 °C

#### 4.1.3 In-Lab Method by Sinusoidal Curves

For spinodal decomposition analysis, a rectangular ROI of dimensions 3.2 nm × 3.2 nm × 30 nm was created in the ferrite phase of each unaged steel. The ROI was positioned at a distance of at least 1 nm away from the heterophase interfaces. The Fe (blue) and Cr (magenta) concentration profiles were determined using a fixed bin width of 0.2 nm. The initial concentration profile data was smoothed using a triangular 3-point moving average defined by  $T_i = \frac{1}{4}(t_{i-2} + 2t_{i-1} + t_i)$  for bins  $i \geq 3$ , where  $t_i$  is the initial data set and  $T_i$  is the smoothed data set. The smoothed profiles were plotted with the mean of the Fe and Cr concentration profiles, which were derived from the ion counts in each bin, Figure 16(a) – (b). The  $\pm 2\sigma$  error bars

of the mean Fe and Cr concentrations were derived from counting statistics. The alternating Fe and Cr concentration fluctuations were defined in the same method. A Cr concentration fluctuation was defined as when the concentration was greater than its mean value  $+2\sigma$  and concomitantly the Fe concentration fluctuation was less than its mean value. Similarly, the Fe concentration fluctuation was defined as when its concentration was greater than its mean value  $+2\sigma$  and concomitantly the Cr concentration fluctuation was less than its mean value. Thus, the periodic alternating fluctuations are defined along the ROI, as shown in Figure 16.

The amplitude of a concentration fluctuation,  $A$ , of Fe or Cr was defined as the highest point from the mean concentration value of that element,  $A_j^k = C_j^k(\max) - \bar{C}_j$ , where  $j$  is the element and  $k$  is the peak number. The wavelength,  $\lambda$ , of Fe or Cr was defined as the distance between two adjacent amplitudes of a concentration fluctuation,  $\lambda_j^k = x_j^{k+1} - x_j^k$ , where  $x$  is the distance along the concentration profile,  $j$  is the element, and  $k$  is the peak number. The code listed in the Appendices automates this method. The methodology discussed above is consistent with evaluation of wavelength and amplitude for periodic concentration fluctuations, and extant methods evaluate these quantities independently [81]. The above analysis was repeated using 20 non-overlapping rectangular ROIs in order to determine wavelength and amplitude size distributions. The wavelength (in nm) and amplitude (in at.%) size distribution histograms were plotted with a bin size of 0.5 for the ferrite phase of both the CF-3 and CF-8 steels. The mean wavelength (MW) and the mean amplitude (MA) were derived from the histograms. Deviation of the ROI cross-sectional dimension within a certain range did not significantly affect the

wavelength and amplitude size distributions, thereby indicating a numerically stable evaluation procedure. Binomial distribution functions, which represent the distribution of random wavelengths and amplitudes, were superimposed on the histograms for comparative analysis. Using the same 20 ROIs, the mean wavelength results were compared with those obtained by ACF method and the mean amplitude results were compared with those determined by the LBM method.

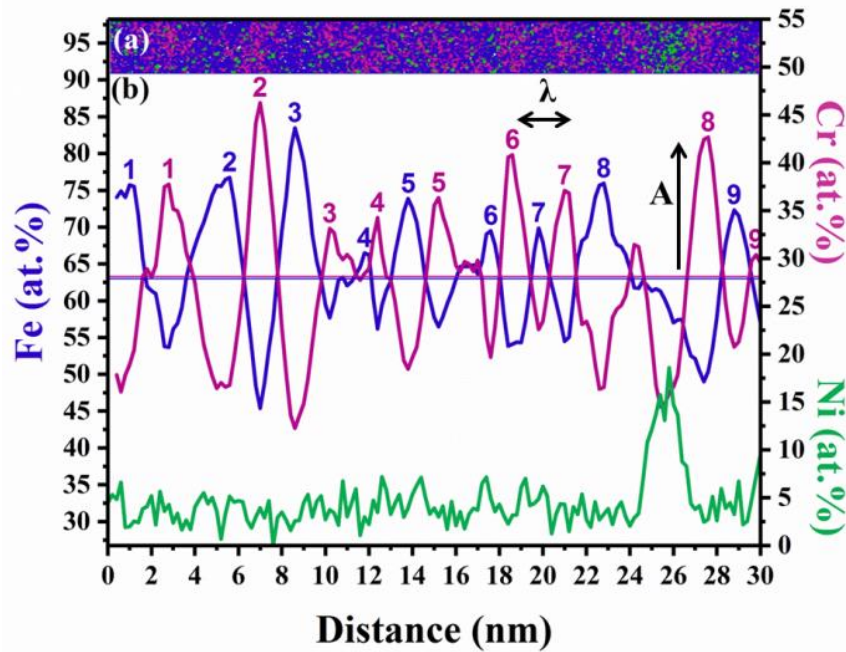


**Figure 16.** (a) APT reconstruction of one ROI that aligns to the Fe, Cr, and Ni curves in (b); (b) Illustrating the in-lab method of simultaneously measuring the spinodal decomposition amplitude and wavelength of sinusoidal waves

#### 4.2 G-phase

##### 3.2.1 Radius (<R>)

The 6.5 at. % Ni isoconcentration were assumed to be spherical. The APT software outputs the volume of the enclosed surface. The radius was calculated using

the volume of a sphere formula,  $V = \frac{4\pi}{3} r_i^3$ .

### 3.2.2 Number Density (N<sub>v</sub>)

Number density was calculated by taking the total number of particles and dividing by the ferrite phase volume. The surfaces of particles that were cut-off at the edge of the tip were counted as ½, while those enclosed in the center of the sample tip were counted as 1.

### 3.2.3 Volume Percentage (V<sub>p</sub>)

The volume percentage summed the volumes of all particles and divided it by the ferrite phase volume using the following equation:  $Vol. \% = \frac{\sum_{i=1}^{i=N} \frac{4\pi}{3} r_i^3 \times 100\%}{Vol_{ferrite}}$

## 4.3 Kinetic Analysis

### 4.3.1 Time Exponents (n)

Time exponents, n, were calculated by fitting the four times and wavelengths data at each temperature to the non-linear LSW theory equation,  $d = Kt^n$  in a mathematical software to find the best fit and output the K and n parameters.

### 4.3.2 Degree of Decomposition (D.o.D)

In spinodal decomposition theory, the amplitudes of the concentration fluctuations increase during thermal aging. The wavelength increases as result of coarsening. Previous researchers [8], [40] have studied the kinetics of the amplitude and wavelength separately. However, this type of analysis underestimates the total amount of Cr atoms that have diffused. To take this into account, the spinodal decomposition ‘volume’, referred to as the degree of decomposition was calculated by multiplying the amplitude to the cubed wavelength as depicted in Figure 17.

The same concept was applied to calculate the D.o.D of the G-phase forming zones. For the G-phase forming zones, the D.o.D was calculated by multiplying the volume fraction to the amplitude because the number density of G-phase is increasing unlike the constant volume fraction in spinodal decomposition.

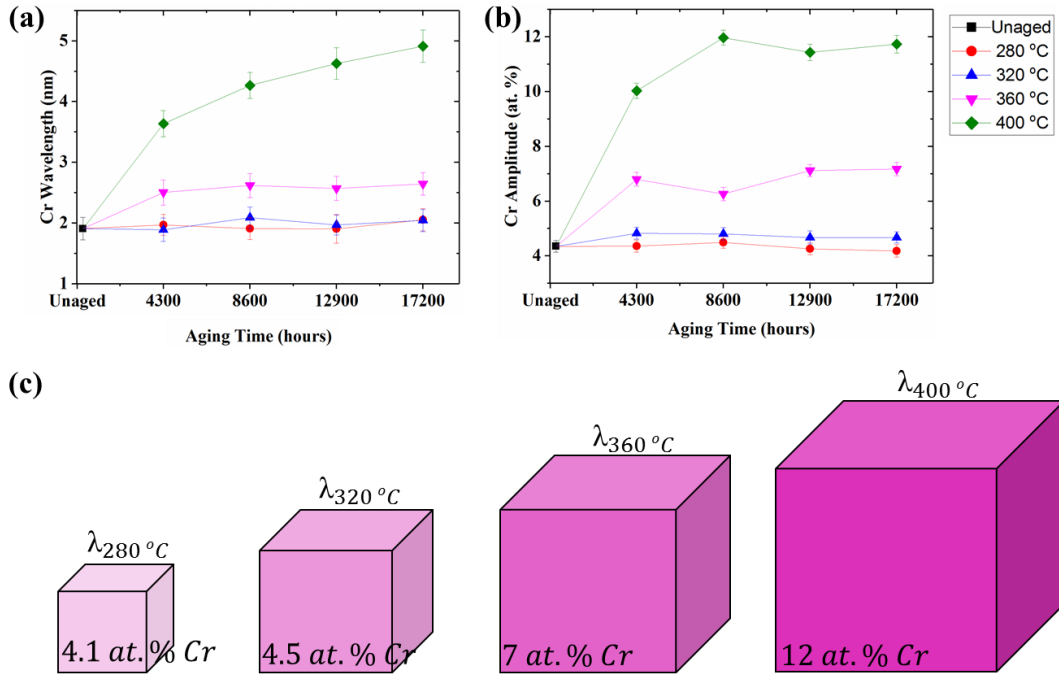


**Figure 17.** Demonstrating the concept of Degree of Decomposition (D.o.D) by showing that (a) the wavelength and (b) the amplitude of CF-3 samples are both increasing during thermal aging. (c) An illustration of the spinodal decomposition domain drawn as a cube, where the wavelength is length of the domain and the amplitude is the Cr concentration in the domain.

#### 4.3.3 Activation Energy

The activation energy of the degree of decomposition (D.o.D) from spinodal decomposition and G-phase precipitation was calculated by finding the slope from a plot of the natural logarithm of D.o.D versus the inverse temperature.

#### 4.4 Fitting Functions

A hyperbolic tangent fitting equation was used to interpolate data between the unaged and 4300 hour time. The calculation to predict the D.o.D was as follows:

$$D.o.D(t, T) = A + B \left( 1 - \operatorname{Tanh} \left[ \frac{\operatorname{Log}[t] - 1000Q/8.314T - C}{D} \right] \right).$$

The constants A, B, C, and D are fitting parameters. The constant Q is also a fitting parameter, regarded as 'apparent' activation energy. The t is time in hours and T is temperature in Kelvins.

## Chapter 5: Experimental Data – Results and Discussion

In this chapter, the data from mechanical testing are presented and analyzed. For microstructural characterization, the elemental partitioning is investigated at multiple length scales by the SEM, S/TEM, and APT methods.

### 5.1 Mechanical Properties

#### 5.1.1 Vickers Microhardness (HV)

The large indents from the 500g load of Vickers microhardness testing encompass the decomposing ferrite phase, the ductile austenite phase, and the ferrite/austenite interphase. Therefore, the microhardness values are an average from all microstructural events, such as spinodal decomposition  $\alpha'$  domains, G-phase precipitates, and  $M_{23}C_6$  carbides, borides, and other large particles. The results in Figure 18 illustrate that the unaged CF-3 has a lower mean Vickers microhardness value of  $151.8 \pm 4.6$  HV500g, whereas the unaged CF-8 has a greater mean value of  $165.8 \pm 5.8$  HV500g. As we discuss below, this difference is possibly caused by the presence of the  $M_{23}C_6$  carbide phase at the heterophase interfaces in the CF-8 steel but not the CF-3 steel. Additionally, C is well known to cause interstitial solid-solution hardening and the nominal concentration of C in the CF-8 steel is greater than in the CF-3 steel. The mean Vickers microhardness increased for both steels after aging due to phase decomposition, as discussed below. After aging, the microhardness values of the two steels are comparable at all four temperatures. The mean microhardness values are greater after aging at accelerated temperatures than operational temperatures for both steels.

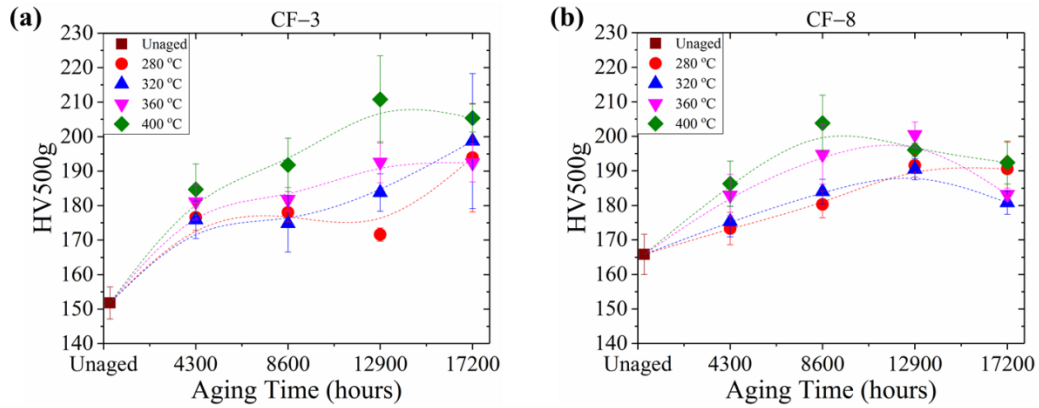


**Figure 18.** Vickers microhardness (HV) data from all (a) CF-3 and (b) CF-8 samples

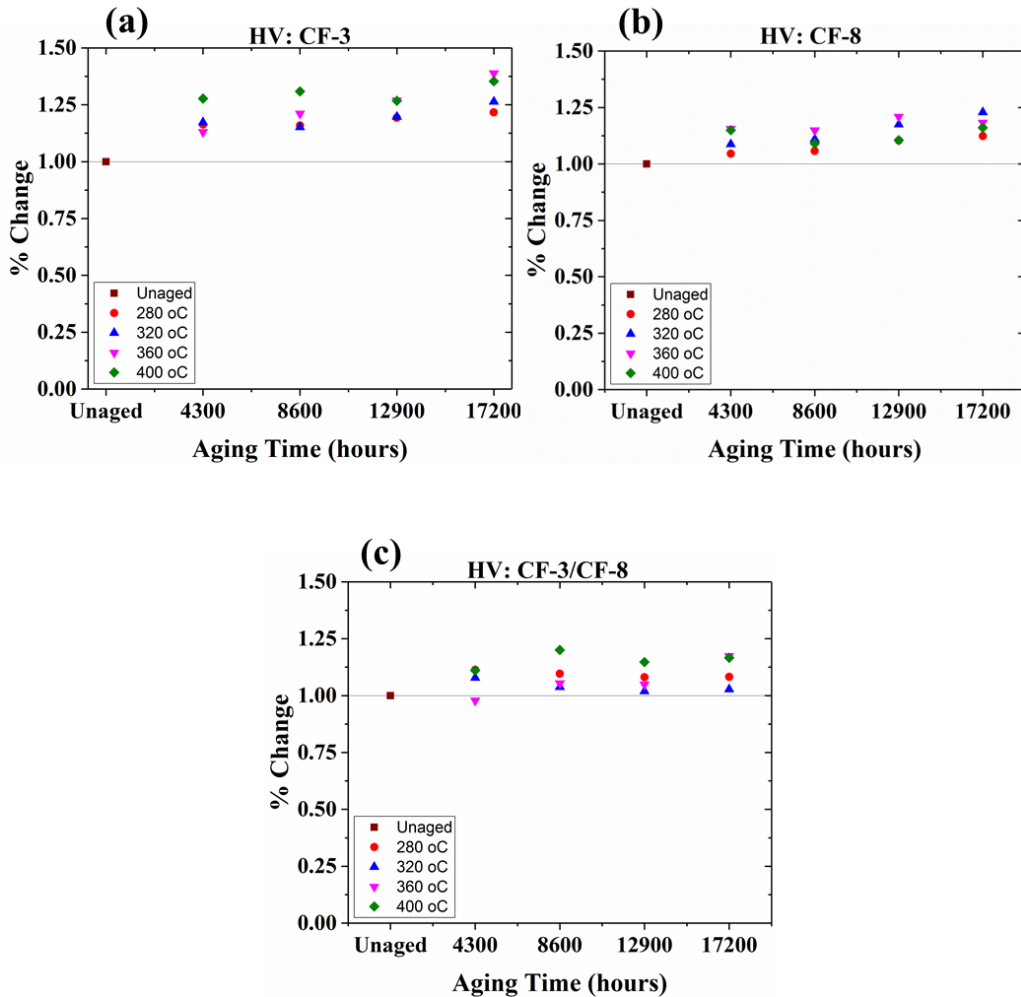


**Figure 19.** Normalized HV data to the unaged value showing percent change in HV data for (a) CF-3 samples, (b) CF-8 samples, and (c) ratio of CF-3 to CF-8

The change in HV was normalized and plotted for both alloys in Figure 19(a)-(b). The ratio of normalized percent change of Vickers microhardness in the CF-3 alloy in Figure 19(c) had a higher increase in hardness than the CF-8 alloy with a range of 2-20%. The discussion will be combined below with CVN.

#### 5.1.2 Charpy V-notch Impact Toughness (CVN)

As illustrated in Figure 20, the lower CVN impact toughness value of the unaged CF-8 of  $317 \pm 80$  J as compared to the unaged CF-3 of  $392 \pm 14$  J is most likely due to the presence of  $M_{23}C_6$  carbides at the heterophase interfaces. Carbides located at the heterophase interfaces may influence the failure mode by causing phase boundary separation thereby leading to low impact toughness values [2]. Previous research also demonstrated a similar trend where an as-cast CF-3 steel [12] had a higher upper shelf energy of  $> 300$  J when compared to the unaged CF-8 steel [85], which had an upper shelf energy of 225 J. The mean CVN values were lower after aging at accelerated temperatures than operational temperatures and both steels exhibited the lowest CVN values when aged at 400 °C. The CF-3 steel had a value of  $\sim 60$  J while CF-8 steel had  $\sim 115$  J. The microstructural evolutions are the basis of the material properties phenomena. When the microstructural reactions approach thermodynamic equilibrium state, the CVN impact toughness saturates to a minimum value.

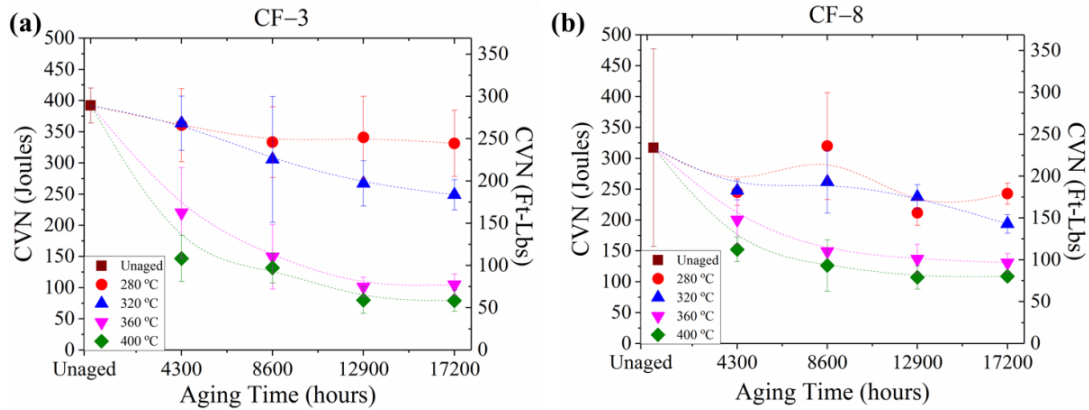


**Figure 20.** Charpy impact toughness data from all (a) CF-3 and (b) CF-8 samples

At operational temperatures, the CF-8 steel exhibited lower values in mean CVN values when compared to CF-3. This could be due to the small carbides scattered along the heterophase interphase. At accelerated temperatures, the CF-3 steel had slighter lower impact toughness when compared to CF-8. This could be due to the greater ferrite content in CF-3, undergoing spinodal decomposition and G-phase precipitation, when compared to CF-3. The carbides in CF-8 are also coarsening, as discussed below, thereby increasing their size but decreasing their surface area along the heterophase interface.

The change in CVN was normalized and plotted for both alloys in Figure 21. The normalized percent change of Charpy V-notch impact toughness in the CF-8 alloy had a larger decrease in impact toughness than the CF-3 alloy with a range of 18-30% at operational temperatures. However, at higher temperatures, the CF-3 alloy had a larger decrease in impact toughness than the CF-8 alloy with a range of 5-40%. This is attributed to the microstructure of the two alloys. The CF-8 alloy has  $M_{23}C_6$  carbides at the heterophase interface that were not dissolved during the solidification heat treatment. At low temperatures, the phase separation kinetics is slow, therefore the effects of the carbide dominates. At higher temperatures, the kinetics of phase

separation is fast, therefore, the effects of phase separation dominate. In addition, the CF-3 alloy has higher ferrite content, and will therefore have more embrittled areas than the CF-8 alloy.

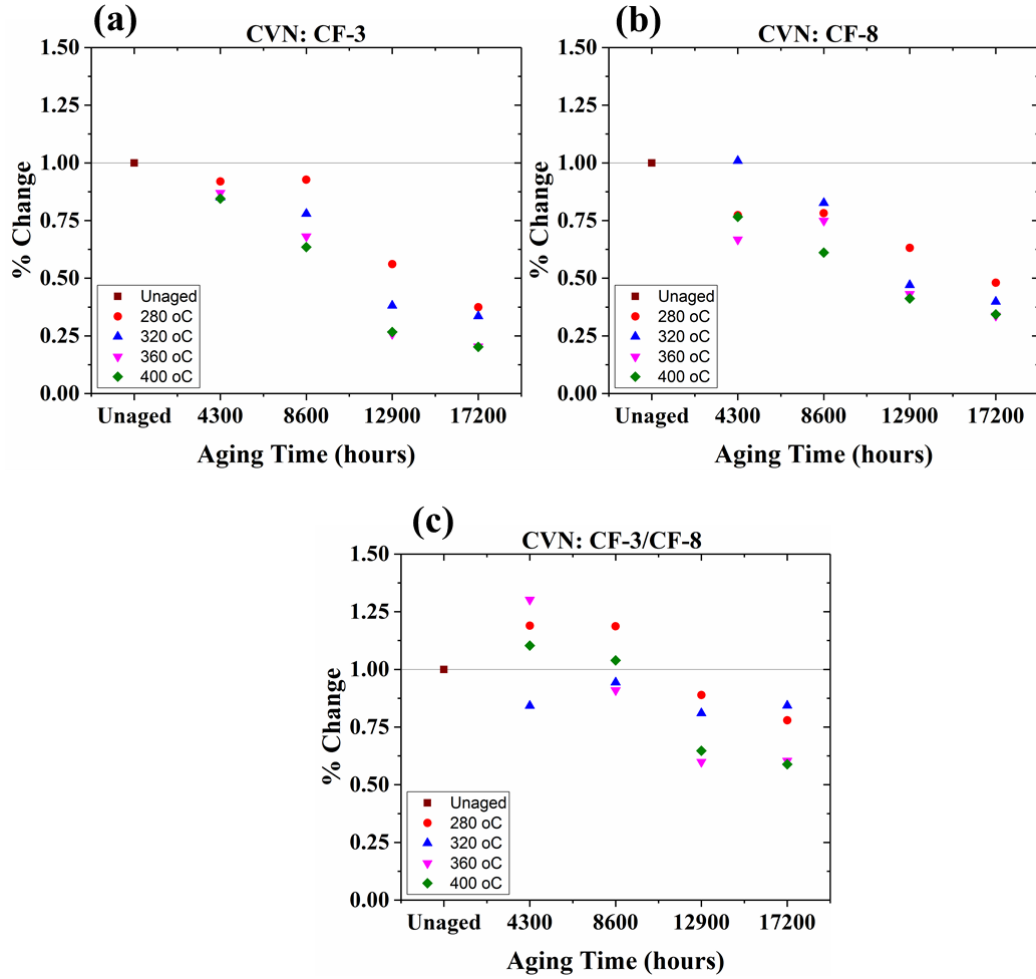


**Figure 21.** Normalized CVN data to the unaged value showing percent change in CVN data for (a) CF-3 samples, (b) CF-8 samples, and (c) ratio of CF-3 to CF-8

Fracture occurs by the nucleation and coalescence of microvoids and is characterized by a dimpled fracture-morphology. The unaged specimens exhibited ductile fracture with significant deformation and did not completely break. All aged specimens exhibited more brittle fracture with less deformation and more granular fracture surfaces. The presence of  $\alpha'$  and G-phase precipitates initiate transgranular

fracture by decohesion of the ferrite spinodal domains. Fractographic evaluation of the specimens exhibited similar fracture modes in both steel as shown in Figure 22. Embrittled CDSS generally have large areas of brittle fracture of ferrite, linked by ductile shearing or tearing of the austenite ligaments. The austenite provides adequate toughness even after long-term aging.

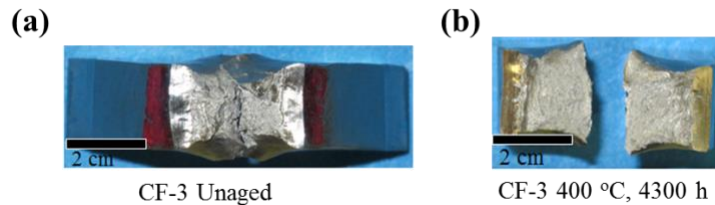


**Figure 22.** Fractography of Charpy specimen: (a) Unaged CF-3 and (b) CF-3 sample aged to 4300 h at 400 °C

Charpy specimens experience both tensile and compressive stresses near the notch tip and on the opposite side of the notch, respectively. Cleavage facets of ferrite occur when the local tensile stress reaches the critical cleavage fracture stress. The degree of embrittlement and, hence, the toughness of the material, is controlled by the amount of brittle fracture. A predominantly brittle failure occurs when either the ferrite phase is continuous and has a large content or the ferrite/austenite phase boundary with phase-boundary carbides provides an easy path for crack propagation. The CF-3 steel with lacy ferrite morphology and a ferrite content of about 10% or greater provides a continuous ferrite phase. The low C content in the CF-3 steel forms little or no carbides compared to the higher C content in CF-8. Even though the CF-8 steel has carbides, it has a lower ferrite content compared to CF-3. Therefore, there is a competition of the effects of embrittling factors from the larger area of decomposed ferrite or carbides at the ferrite/austenite interphase. The relationship between the degree of cleavage fracture and toughness is complex because cleavage

cracks can be initiated by several mechanisms, such as dislocation pile up and cracking of carbide particles. Each of the mechanisms requires a unique stress level. Thus, for the same amount of cleavage fracture, the toughness may vary in different cast materials [85], [86].

## 5.2 Optical Microscopy

An optical micrograph, Figure 23, illustrates a microstructure consisting of a network of island-shaped  $\delta$ -ferrite phase (dark color) in the continuous  $\gamma$ -austenite phase (light color) for the unaged CF-3 steel. The microstructure of the unaged CF-8 steel has a qualitatively similar appearance to that of the CF-3 steel.

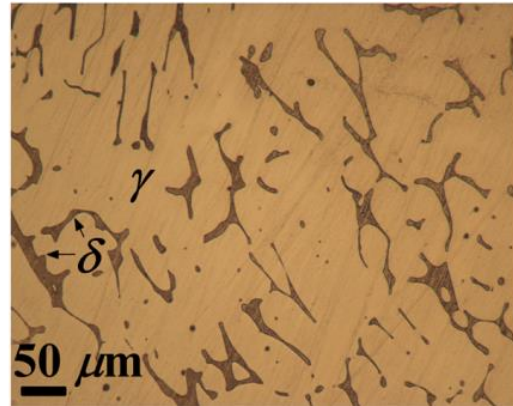


**Figure 23.** Optical Micrograph of representative CF-3 alloy.

### 5.2.1 Volume Fractions

The ferrite volume percentage is  $11.5 \pm 1.1$  % for the CF-3 steel while that of the CF-8 steel is  $9.1 \pm 0.9$  % as measured by the manual point counting method specified in the ASTM E562-11 standard [87] and [88]. The microstructure observed in this study is consistent with that reported in the literature of a steel with a composition similar to CF-8 and with a ferrite volume percentage of less than 20 % [15], [16]. The ferrite volume percentage was stable during aging at all four temperatures.

The b.c.c.  $\delta$ -ferrite phase volume percentage of the CF-3 steel is greater than the CF-8 steel when measured by the three aforementioned methods, Table 3. By the manual point counting method, the CF-3 steel ferrite volume percentage is  $11.5 \pm 1.1$  vol% while that of the CF-8 steel is  $9.1 \pm 0.9$  vol%. The digital counting method results in a ferrite volume percentage of  $12.1 \pm 1.0$  vol% for the CF-3 steel and  $10.0 \pm 0.4$  vol% for the CF-8 steel. The Schoefer method based on the CF-3 and CF-8 nominal compositions predicts ferrite volume percentages of  $18 \pm 6.3$  vol% and  $14 \pm 4.8$  vol%, respectively.

**Table 3.** Ferrite volume fraction measurements by manual point counting, digital counting and Schoefer diagram.

<b>Steel</b>	<b>Manual Point Counting [ASTM E562-11]</b>	<b>Digital Counting [ASTM E1245-03]</b>	<b>Schoefer Diagram [ASTM A800-14]</b>
<b>CF-3</b>	$11.5 \pm 1.1$	$12.1 \pm 1.0$	$18 \pm 6.3$
<b>CF-8</b>	$9.1 \pm 0.9$	$10.0 \pm 0.4$	$14 \pm 4.8$

The Schoefer diagram is based on Cr equivalency and Ni equivalency values, where the magnitude of each element's contribution to the b.c.c.-forming chromium equivalency term,  $Cr_{eq}$ , and f.c.c.-forming nickel equivalency term,  $Ni_{eq}$ , affect the formation of either the  $\delta$ -ferrite or the  $\gamma$ -austenite phase, respectively. The CF-3 steel has a  $Cr_{eq}/Ni_{eq}$  ratio of 1.34, whereas the CF-8 steel has a ratio of 1.25, resulting in a larger expected ferrite volume percentage in the former. Since the Schoefer diagram is not specific to the CDSS used in this study and is based on generalized composition and element equivalency data of many duplex stainless steels, the values measured by the manual point counting method and the digital counting of pixels method are likely more accurate. The directly measured values are, however, comparable with the

values estimated from the material chemical composition using the ASTM A800/A800M methodology.

### 5.3 Scanning Electron Microscopy (SEM)

#### 5.3.1 Elemental Partitioning

The SEM-EDS spectra, SEM micrograph, and corresponding SEM-EDS elemental maps were obtained from an example  $\delta$ -ferrite/ $\gamma$ -austenite heterophase interface in the unaged CF-3 stainless steel, as illustrated in Figure 24. The CF-8 SEM-EDS elemental maps and spectra are qualitatively similar to that of the CF-3 steel. The elemental maps, in which brighter colors indicate higher elemental contents, clearly exhibit elemental partitioning between the two phases: an enrichment of Cr (magenta) in the  $\delta$ -ferrite phase, and an enrichment of Ni (green) in the  $\gamma$ -austenite phase. It is well known that Cr is a ferrite stabilizer, whereas Ni is an austenite stabilizer [1].

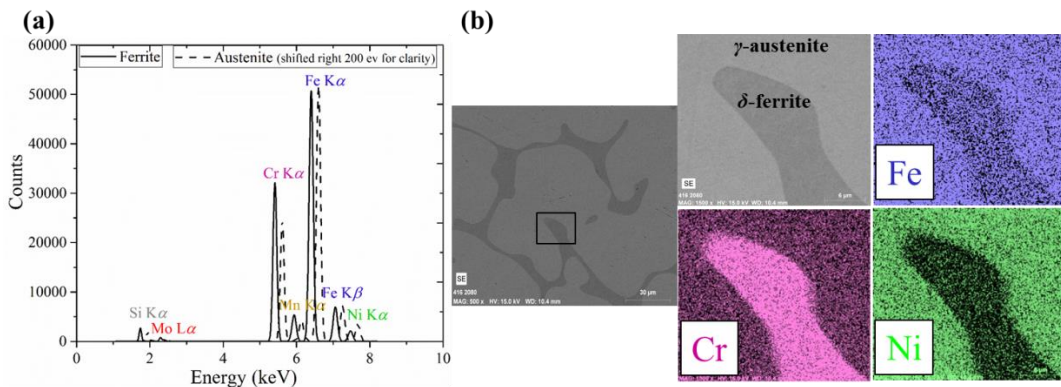


**Figure 24.** SEM-EDS (a) Spectra, and (b) Elemental mapping for the ferrite and austenite phases in the unaged CF-8 sample

The corresponding SEM-EDS spectra also supports the observed elemental partitioning in the  $\gamma$ -austenite phase, showing a greater peak maxima of the major

elements Fe  $K_{\alpha}$ , Fe  $K_{\beta}$ , and Ni  $K_{\alpha}$ , whereas the  $\delta$ -ferrite phase has a greater peak maxima for the major element Cr  $K_{\alpha}$ , and the minor elements Mn  $K_{\alpha}$ , Si  $K_{\alpha}$ , and Mo  $L_{\alpha}$ . The partitioning ratio of an element j,  $\kappa_j$ , is defined as the element j concentration in the ferrite phase,  $C_j^{\delta}$ , divided by the elemental concentration in the austenite phase,  $C_j^{\gamma}$ , or  $\kappa_j^{\delta/\gamma} = C_j^{\delta}/C_j^{\gamma}$ . The major element partitioning ratios calculated from the SEM-EDS results are 0.97 for Fe, 1.25 for Cr, and 0.57 for Ni in the CF-3 steel, whereas they are 0.93 for Fe, 1.19 for Cr, and 0.38 for Ni in the CF-8 steel.

#### 5.4 Atom Probe Tomography (APT)

##### 5.4.1 Elemental Partitioning Across the Heterophase Interface

Example APT reconstruction and proximity histogram concentration profiles of the unaged CF-3 stainless steel are illustrated in Figure 25(a) – (b) and of the unaged CF-8 stainless steel are illustrated in Figure 26(a) – (b). The APT reconstructions, Figure 25(a) and Figure 26(a), illustrate the enhancement of Cr (magenta) atoms in the b.c.c.  $\delta$ -ferrite phase and Ni (green) atoms in the f.c.c.  $\gamma$ -austenite phase. The corresponding proxigrams in Figure 25(b) for the CF-3 stainless steel and Figure 26(b) for the CF-8 stainless steel show monotonically increasing Ni and Mn concentrations across the heterophase interface from the  $\delta$ -ferrite phase to the  $\gamma$ -austenite phase.

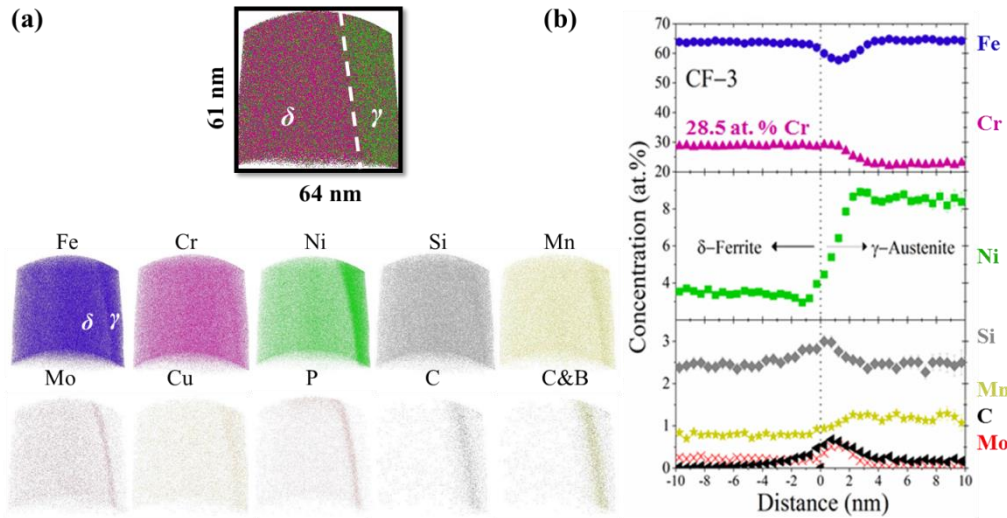


**Figure 25.** (a) APT reconstructions and (b) proxigram of unaged CF-3

Interfacial segregation of C, Mo, and Si at the heterophase interface is also observed in both steels. From the proxigram profiles, the ferrite phase has an average concentration of 28.7 at.% Cr and 63.8 at.% Fe for the CF-3 steel in Figure 25(b), and 24.9 at.% Cr and 67.5 at.% Fe for the CF-8 steel in Figure 26(b). The major element partitioning ratios extracted from the APT proximity histogram concentration profiles are 0.97 for Fe, 1.19 for Cr, and 0.64 for Ni in the CF-3 steel, whereas they are 1.05 for Fe, 1.10 for Cr, and 0.37 for Ni in the CF-8 steel.

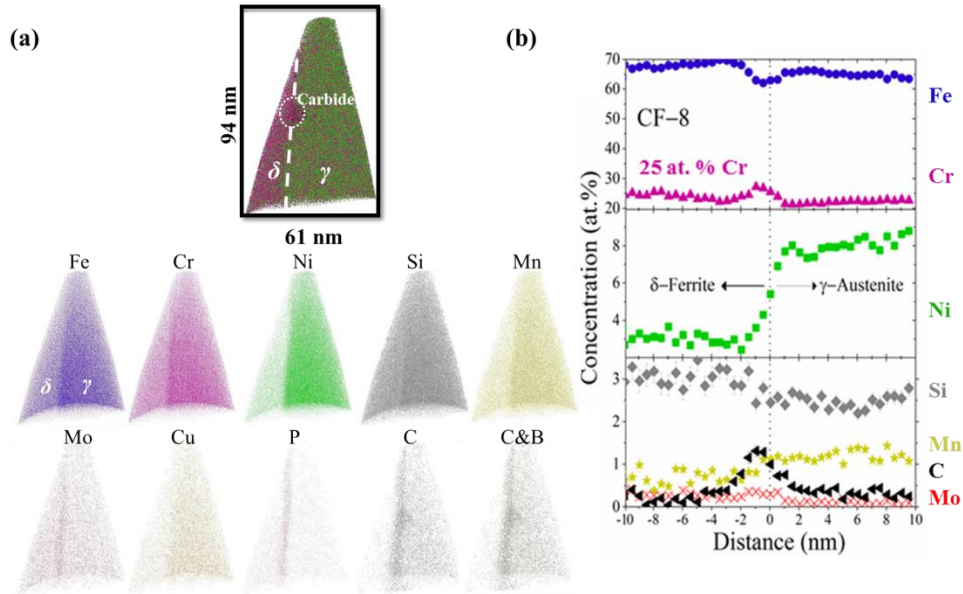


**Figure 26.** (a) APT reconstructions and (b) proxigram of unaged CF-8

The differences in composition and elemental partitioning as measured by SEM-EDS and APT analysis likely results from the differences in the effective analysis volume of each technique and natural heterogeneity of the specimen. The x-rays generated during an SEM-EDS analysis using 15 kV electrons emanate from an interaction volume on the order of cubic-microns, thus averaging over intersected regions of varying heterogeneity, while APT is able to directly measure local compositions at the nanometer length scale. Studies, by Brown and Smith employing 1-D APT on CF-3 steel [17] and Guo, et al. employing electron probe microanalysis (EPMA) on Z3CN20-09M steel, which has a composition similar to CF-8, measured partitioning ratios. Brown and Smith obtained partitioning ratios of 0.95 for Fe, 1.34 for Cr, and 0.56 for Ni, whereas Guo, et al. determined partitioning ratios of 0.97 for Fe, 1.28 for Cr, and 0.57 for Ni, which are qualitatively similar to the measurements on the steels in this study.

#### 5.4.2 Spinodal Decomposition and G-phase Formation in Ferrite Phase

In the unaged samples, all elements appear to be uniformly distributed inside each phase. In the CF-3 steel, the ferrite phase is enriched in Cr and Mo. In the CF-8 steel, the ferrite phase has less Cr than the austenite. The austenite phases of both steels are enriched in Fe, Ni, Mn, Cu, and C. The ferrite/austenite interface of the specimen was observed with a clear enrichment of Mo, C, P and B, but a slight depletion of Fe and Cr, and insignificant enrichment of Ni, Mn, Si and Cu as seen in APT maps in Figure 25 and Figure 26. The strong interface segregates, C, Mo, B may lead to formation of carbides, sigma, laves, or borides, respectively.

In the APT maps, Figure 27, of CF-3 and CF-8 steels aged for 8600 h at 400 °C, Cr appears to be homogeneous inside both the ferrite and the austenite grains by a visual examination. However, Cr amplitude measurements clearly demonstrate slightly developed non-random distributions, as discussed later. The G-phase forming elements of Ni, Si, Mn, and Cu are also clearly partitioning within the ferrite phase. Clustering of Mo, Cu, P, C, and B are forming in parts of the ferrite/austenite interface together with slight segregation of Fe, Ni, Mn, and Si to the heterophase interface.

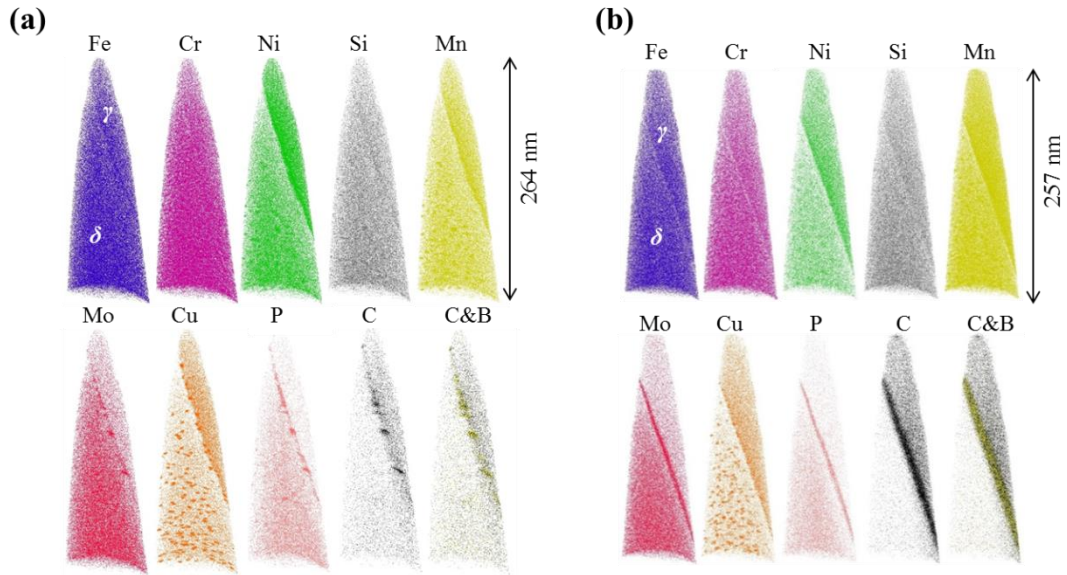


**Figure 27.** APT elemental mapping of (a) CF-3 and (b) CF-8 steels aged for 8600 h at 400 °C

In the APT maps, Figure 28, of CF-3 sample aged for 17200 h at 400 °C, the uneven Cr distribution in the ferrite phase is visibly clear. The Cr-rich domains are elongated and interconnected. The G-phase forming elements of Ni, Si, Mn, and Cu have clearly formed clusters. Only a small portion of the austenite phase was captured in this sample. Nonetheless, it is clear that there is a slight depletion of Fe and Cr at the ferrite/austenite boundary, while Ni, Si, Mn, Mo, Cu, P, C, and B, are segregating to the interface. Due to the segregation of solute elements to the heterophase interface, no G-phase formation is visible within about 10 nm of the interface. This indicates that nucleation and growth of G-phase precipitates are fully suppressed in the Ni SDZ and thus are thermodynamically and kinetically different from that in the inner ferrite. Interestingly, some elements of Cu, P, C, and Mo were clustering along the heterophase interface boundary, while of Ni, Si, and Mn were spread like a film. This segregation of solute elements leads to further weakening of the heterophase boundary.

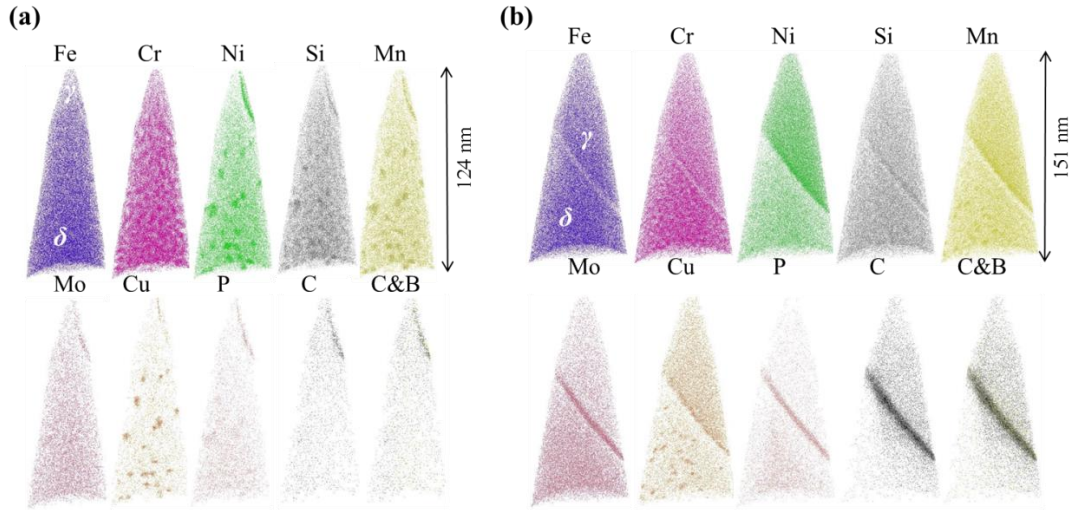


**Figure 28.** APT elemental mapping of (a) CF-3 and (b) CF-8 steels aged for 17200 h at 400 °C

#### 5.4.3 Elemental Segregation to the Heterophase Interface

With the partitioning of solute elements, four primary microstructural changes occur in the alloys: spinodal decomposition of Cr-rich  $\alpha'$ -domain, precipitation of  $\varepsilon$ -Cu clusters, formation of Ni-Si-Mn-rich clusters in G-phase zones, and growth of carbides or other interface precipitates. The first three take place within the ferrite phase while the latter takes place at the ferrite/austenite interphase boundary.

As reported above, the proximity histogram (proxigram) concentration profiles across the  $\delta$ -ferrite/ $\gamma$ -austenite heterophase interfaces are qualitatively similar for the unaged CF-3 and CF-8 steels, Figure 25 and Figure 26, respectively. However a distinct carbide phase is observed in the CF-8 reconstruction. The peak C concentration at the heterophase interface is  $\sim 0.8$  at.% for the CF-3 steel and  $\sim 1.5$  at.% for the CF-8 steel, which is influenced by the presence of a carbide phase. As discussed below, this carbide phase is identified as the  $M_{23}C_6$  carbide. Since the CF-8 steel has a greater nominal C concentration than the CF-3 steel, the thermodynamic

driving force for carbide formation at the heterophase interfaces is greater [18]. A more detailed analysis, Figure 29 was performed to determine the  $M_{23}C_6$  carbide phase composition. The carbides are interspersed along the  $\delta$ -ferrite/ $\gamma$ -austenite heterophase interface of the APT specimen tip, Figure 29(a), and an example of the carbide is visible in the APT reconstruction, Figure 29(b). The Cr and C are enriched, while Fe and Ni are depleted within the carbide phase (black box), Figure 29(c). The carbide composition is  $32.5 \pm 2.1$  at.% Fe,  $49.2 \pm 1.5$  at.% Cr,  $11.9 \pm 1.2$  at.% C,  $2.0 \pm 0.4$  at.% Mo,  $2.1 \pm 0.7$  at.% Ni,  $1.1 \pm 0.2$  at.% Mn, and  $0.65 \pm 0.14$  at.% Si. Recent CALPHAD calculations indicate that the most common carbide present in CF-8 steels is the f.c.c.  $M_{23}C_6$  carbide, where  $M = Cr$  [18]. Since the steels were cast, solution-treated, and quenched in water at room temperature, the carbide composition in the unaged state is most likely not yet at equilibrium.

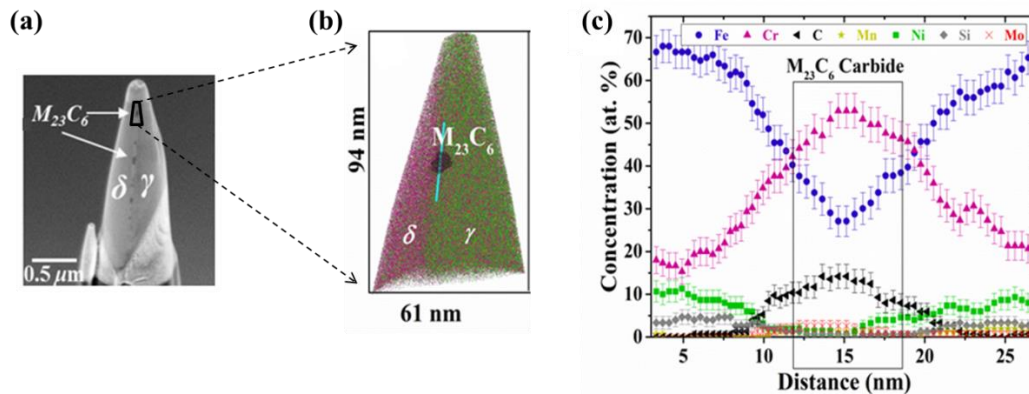


**Figure 29.** (a) SEM image and (b) APT reconstruction of unaged CF-8 sample with carbide. (c) The 1-D composition profile is plotted along the carbide.

The lower C alloy, CF-3 has less C segregation at the phase boundary than CF-8, which has carbides in many locations on the phase boundary. Not only C, but also Mo and B, which probably have similar concentrations in both steel, segregate to the heterophase interface to form precipitates. Compared to Figure 30, the interface

precipitates are observed sparingly in the unaged condition but are much more prevalent in the aged materials. In the SEM images, the precipitates at the heterophase interface are distinguished from the ferrite and austenite by the high channeling contrast of high density metallic elements. However, it is not possible to identify the type of precipitate without further structure and chemical analysis. The images that are labeled with a phase were samples that were successfully collected in the APT.

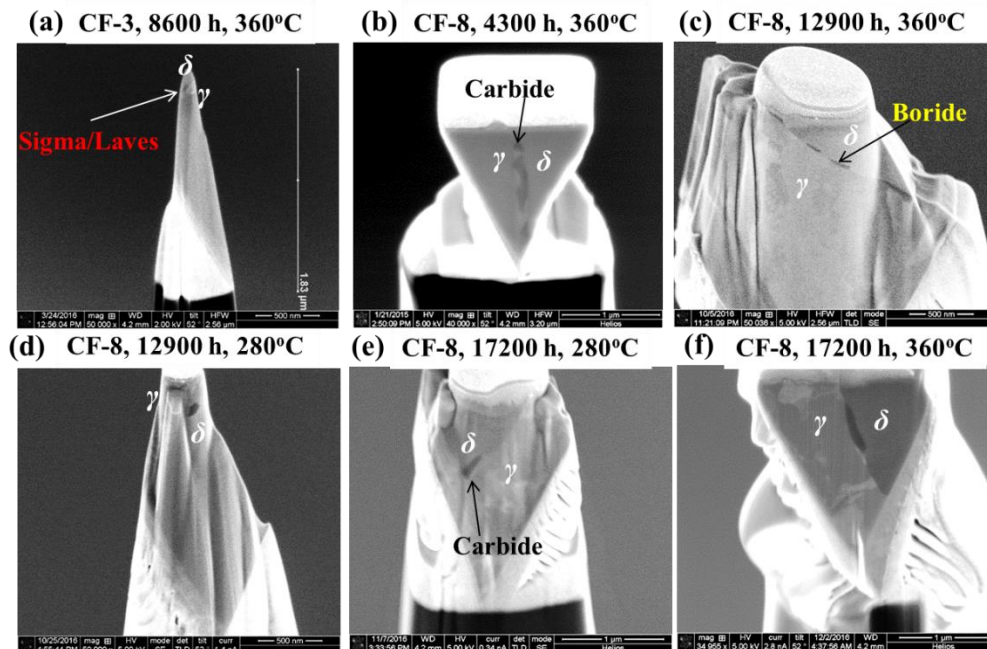


**Figure 30.** SEM images of precipitates at the ferrite/austenite interface. (a) A possible sigma/laves phase in CF-3 steel aged for 8600 h at 360 °C; (b) a carbide phase in CF-8 steel aged for 4300 h at 360 °C; (c) a boride phase in CF-8 steel aged for 12900 h at 360 °C; (d) an unknown phase in CF-8 steel aged for 12900 h at 280 °C; (e) a carbide phase in CF-8 steel aged for 17200 h at 280 °C; and (f) an unknown phase in CF-8 steel aged for 17200 h at 360 °C.

#### 5.4.4 Carbides and Other Heterophase Precipitates

There are many small sized carbides in the unaged compared to the few large coarsened ones in the aged samples as shown in Figure 29 and Figure 30. The  $M_{23}C_6$

carbide has an elongated morphology along the heterophase interface. The  $M_{23}C_6$  carbide and  $\gamma$ -austenite phase are both f.c.c and they exhibit a cube-on-cube orientation relationship (OR) of  $\{111\}_{\gamma} \parallel \{333\}_{M_{23}C_6}$ ,  $\langle 110 \rangle_{\gamma} \parallel \langle 330 \rangle_{M_{23}C_6}$ . In the CF-8 sample aged for 17200 hours at 400 °C, as shown in Figure 31, the phase boundary is very jagged. The carbide grows into the  $\delta$ -ferrite phase because the  $\delta$ -ferrite/ $M_{23}C_6$ -carbide boundary has incoherent interfaces and the  $\delta$ -ferrite has higher Cr-content and faster diffusivity of Cr in the b.c.c lattice.

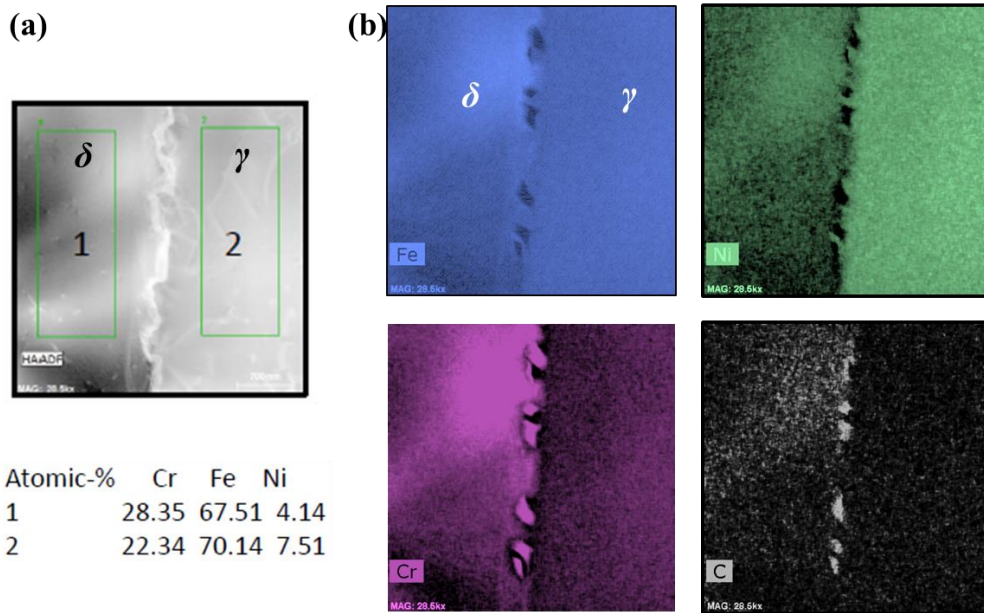


**Figure 31.** (a) S/TEM image and (b) chemical mapping of carbide along the ferrite/austenite interface of the CF-8 samples aged to 17200 hours at 400 °C

By TEM study, the carbides were not observed wholly inside the b.c.c.  $\delta$ -ferrite phase or the f.c.c.  $\gamma$ -austenite phase. They were only found along the  $\delta$ -ferrite/ $\gamma$ -austenite heterophase interfaces. With a low nominal C concentration and lack of carbides, the CF-3 alloy exhibited straight interfaces of the steel. In contradistinction, the CF-8 alloy exhibited undulating interfaces and carbides. The SAED patterns of the CF-3 steel showed a lack of superlattice diffraction spots.

Meanwhile, the SAED patterns of the CF-8 steel, along the austenite zone axis [001], revealed the presence of f.c.c. superlattice diffraction spots indicative of an  $M_{23}C_6$  carbide phase [83]. The lattice parameter of the carbide was 1.109 nm, which is comparable to literature values between 1.05 nm and 1.10 nm [51], [32], [89]. The small variations in the lattice parameter are due to differences in chemical composition of the steel [38]–[40].

A TEM-EDS line-scan was taken across the ferrite,  $M_{23}C_6$  carbide, and austenite phases [83]. It illustrated that the unaged carbide is enriched in Cr, C, and Mn and depleted in Fe and Ni when compared to the adjacent ferrite and austenite phases. In addition, at a distance of approximately 50 nm away from the heterophase interface into the ferrite phase, a depletion of Cr was observed, which suggests the presence of a solute depleted zone (SDZ). How a Cr SDZ affects the kinetics of spinodal decomposition will be discussed below.

Due to the difficulty of capturing carbide at every tip, the data for carbides is sparse. In addition, there was a high incidence of tip fracture during data acquisition of carbides. A proxigram of a 4300 hour aged sample at 360 °C in Figure 32 shows a possible  $M_{23}C_6$  carbide that has a composition of  $22.5 \pm 0.7$  at.% Fe,  $58.5 \pm 0.8$  at.% Cr,  $13.5 \pm 0.6$  at.% C,  $1.1 \pm 0.2$  at.% Mo,  $1.4 \pm 0.2$  at.% Ni,  $0.7 \pm 0.1$  at.% Mn,  $0.7 \pm 0.1$  at.% B, and  $0.0 \pm 0.0$  at.% Si, while the ferrite has a composition of  $75.2 \pm 0.4$  at.% Fe,  $16.0 \pm 0.4$  at.% Cr,  $0.1 \pm 0.0$  at.% C,  $0.2 \pm 0.0$  at.% Mo,  $3.7 \pm 0.2$  at.% Ni,  $0.7 \pm 0.1$  at.% Mn,  $0.0 \pm 0.0$  at.% B, and  $0.0 \pm 0.0$  at.% Si.

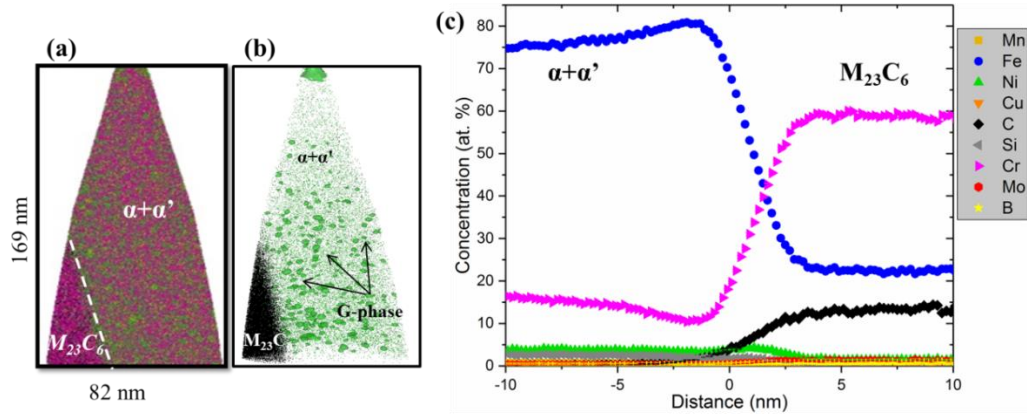


**Figure 32.** (a) Reconstruction and (b) proxigram of possible  $M_{23}C_6$  carbide in 4300 hour aged CF-8 sample at 360 °C

Other carbides have been captured at other aging temperatures and times. A proxigram of a 12900 hour aged sample at 320 °C in Figure 33 shows a possible  $M_{23}C_6$  carbide that is enriched in Cr and B and depleted in Fe, Ni, and Si, with a composition of  $22.0 \pm 2.3$  at.% Fe,  $50.5 \pm 2.7$  at.% Cr,  $20.0 \pm 2.2$  at.% C,  $1.8 \pm 0.7$  at.% Mo,  $1.9 \pm 0.7$  at.% Ni,  $0.9 \pm 0.5$  at.% Mn,  $0.8 \pm 0.5$  at.% B, and  $0.2 \pm 0.2$  at.% Si in the carbide and  $75.2 \pm 1.8$  at.% Fe,  $16.2 \pm 1.5$  at.% Cr,  $0.4 \pm 0.2$  at.% C,  $0.2 \pm 0.1$  at.% Mo,  $4.0 \pm 0.8$  at.% Ni,  $0.6 \pm 0.3$  at.% Mn,  $0.0 \pm 0.0$  at.% B, and  $3.0 \pm 0.7$  at.% Si in the ferrite.

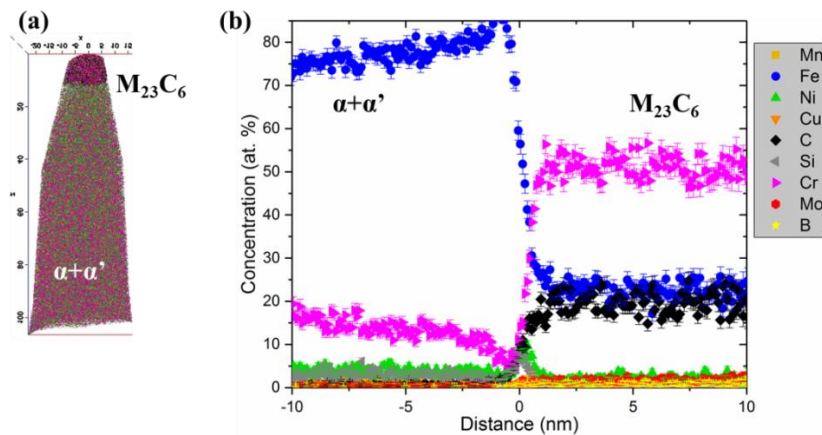


**Figure 33.** (a) Reconstruction (scale in nm) and (b) proxigram of possible  $M_{23}C_6$  carbide in 12900 hour aged CF-8 sample at 320 °C

A proxigram of a 17200 hour aged sample at 280 °C in Figure 34 shows a possible  $M_{23}C_6$  carbide that is enriched in Cr and B and depleted in Fe, Ni, and Si, with a composition of  $23.6 \pm 3.1$  at.% Fe,  $52.7 \pm 3.6$  at.% Cr,  $16.6 \pm 2.7$  at.% C,  $1.6 \pm 0.9$  at.% Mo,  $2.4 \pm 1.0$  at.% Ni,  $0.9 \pm 0.6$  at.% Mn,  $1.5 \pm 0.8$  at.% B, and  $0.0 \pm 0.0$  at.% Si in the carbide and  $77.9 \pm 0.9$  at.% Fe,  $13.7 \pm 0.7$  at.% Cr,  $0.1 \pm 0.0$  at.% C,  $0.1 \pm 0.1$  at.% Mo,  $4.2 \pm 0.4$  at.% Ni,  $0.6 \pm 0.2$  at.% Mn,  $0.0 \pm 0.0$  at.% B, and  $2.8 \pm 0.3$  at.% Si in the ferrite.

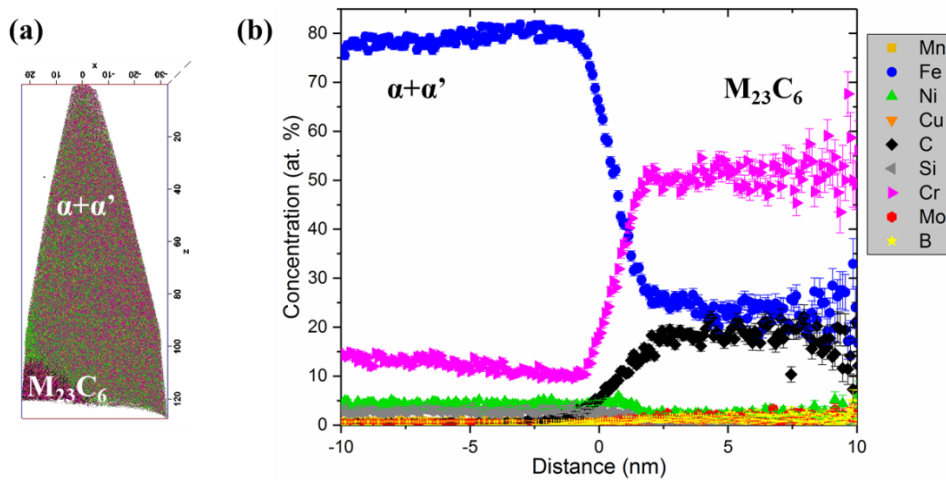


**Figure 34.** (a) Reconstruction (scale in nm) and (b) proxigram of possible  $M_{23}C_6$  carbide in 17200 hour aged CF-8 sample at 280 °C

Boron also segregates to the heterophase interface. A proxigram of a 12900 hour aged sample at 360 °C in Figure 35 shows a possible  $Cr_2B$  boride that is enriched in Cr and B and depleted in Fe, Ni, and Si, with a composition of  $19.5 \pm 1.0$  at.% Fe,  $45.9 \pm 1.2$  at.% Cr,  $0.9 \pm 0.2$  at.% C,  $0.8 \pm 0.2$  at.% Mo,  $0.5 \pm 0.2$  at.% Ni,  $0.6 \pm 0.2$  at.% Mn,  $31.3 \pm 1.1$  at.% B, and  $0.0 \pm 0.0$  at.% Si in the boride and  $65.4 \pm 0.4$  at.% Fe,  $26.6 \pm 0.4$  at.% Cr,  $0.2 \pm 0.0$  at.% C,  $0.4 \pm 0.1$  at.% Mo,  $3.4 \pm 0.2$  at.% Ni,  $0.7 \pm 0.1$  at.% Mn,  $0.0 \pm 0.0$  at.% B, and  $2.6 \pm 0.2$  at.% Si in the ferrite.

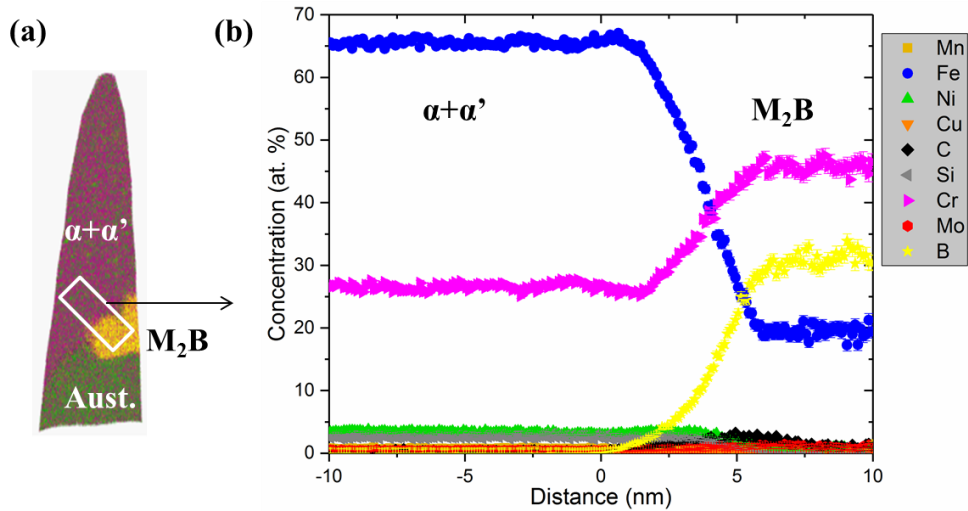


**Figure 35.** (a) Reconstruction (scale in nm) and (b) proxigram of possible  $\text{Cr}_2\text{B}$  boride in 12900 hour aged CF-8 sample at  $360^\circ\text{C}$

Since both C and B are at the heterophase interface, an interesting mix of the two elements with Cr is also possible. A proxigram of a 8600 hour aged sample at  $360^\circ\text{C}$  in Figure 36 shows a possible  $\text{Cr}_{23}(\text{C},\text{B})_6$  hybrid that is enriched in Cr, C, and B and depleted in Fe, Ni, and Si, with a composition of  $29.7 \pm 0.9$  at.% Fe,  $45.4 \pm 0.9$  at.% Cr,  $15.2 \pm 0.7$  at.% C,  $1.1 \pm 0.2$  at.% Mo,  $1.3 \pm 0.2$  at.% Ni,  $0.8 \pm 0.2$  at.% Mn,  $5.7 \pm 0.4$  at.% B, and  $0.0 \pm 0.0$  at.% Si in the hybrid and  $65.6 \pm 0.5$  at.% Fe,  $21.9 \pm 0.5$  at.% Cr,  $0.4 \pm 0.1$  at.% C,  $0.2 \pm 0.0$  at.% Mo,  $7.2 \pm 0.3$  at.% Ni,  $1.0 \pm 0.1$  at.% Mn,  $0.0 \pm 0.0$  at.% B, and  $2.5 \pm 0.2$  at.% Si in the austenite. Since the APT samples only captured the edge of the precipitate, it is difficult to discuss the equilibrium stoichiometry of the carbides.

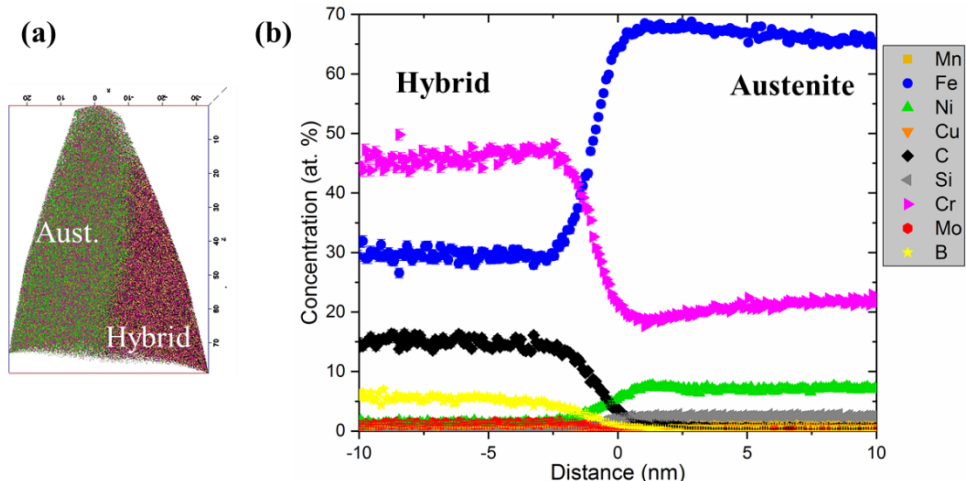


**Figure 36.** (a) Reconstruction (scale in nm) and (b) proxigram of possible Cr<sub>23</sub>(C,B)<sub>6</sub> hybrid in 8600 hour aged CF-8 sample at 360 °C

The process of steel production can be easily contaminated with trace amounts of impurities, such as Cu, B, and P. The probability of finding boride in Figure 35 was by sheer chance. The CF-3 steel had a lack of carbides due to its low carbon content. Both the CF-3 and CF-8 steels have a low Mo content. It was coincidental to find a Mo-enriched phase in the SEM and APT analysis in Figure 37. Without TEM SAED patterns, there is a variety of possibilities for the type of this precipitate. Both sigma and laves phases have enriched Mo. The 1-D concentration profile from ferrite to the precipitate shows the ferrite has a composition of  $63.5 \pm 1.0$  at.% Fe,  $28.3 \pm 1.0$  at.% Cr,  $0.2 \pm 0.1$  at.% C,  $0.3 \pm 0.1$  at.% Mo,  $3.7 \pm 0.4$  at.% Ni,  $0.9 \pm 0.2$  at.% Mn,  $0.0 \pm 0.0$  at.% B, and  $2.4 \pm 0.3$  at.% Si and the possible laves/sigma phase has a composition of  $71.1 \pm 1.1$  at.% Fe,  $18.9 \pm 0.9$  at.% Cr,  $0.2 \pm 0.1$  at.% C,  $1.0 \pm 0.2$  at.% Mo,  $4.4 \pm 0.5$  at.% Ni,  $1.0 \pm 0.2$  at.% Mn,  $0.0 \pm 0.0$  at.% B, and  $2.7 \pm 0.4$  at.% Si.

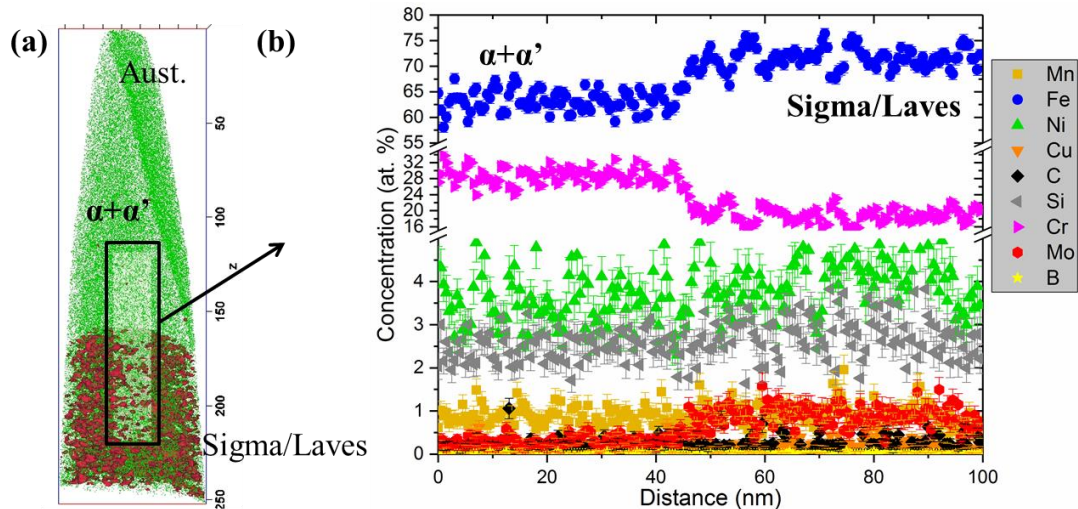


**Figure 37.** (a) Reconstruction (scale in nm) and (b) proxigram of possible Sigma or Laves phase in 8600 hour aged CF-3 sample at 360 °C

In Table 1, the compositions of the ferrite/austenite interface segregates, such as Cu, P, and B, were not reported from the foundry. It is logical to assume that they are impurities and would be equivalent for both alloys. For all other reported interface segregates, there is slightly more Mo in CF-8 and slightly more Ni, Si, and Mn in CF-3. Boride and hybrid of mixed carbide and boride have been identified in the CF-8 steel. A small edge of an unknown phase enriched in Fe, Mo, and Ni and depleted in Cr was spotted in the CF-3 steel. It is possibly a Laves or Sigma phase, even if the Mo content is still quite low.

The carbides and borides are enriched in Cr, thus depleting the Cr concentration in the ferrite phase. The probable laves or sigma phase is depleted in Cr compared to the ferrite phase. The Cr content changes with the local environment. Since the Cr concentration is one of the main elements in spinodal decomposition, the precipitates at the ferrite/austenite boundary may play a role in the phase separation kinetics.

## Chapter 6: Phase Separation Kinetics – Results and Discussion

In this chapter, the wavelengths and amplitudes are used to measure the total diffusion of Cr atoms for spinodal decomposition while the volume fraction and concentration amplitude of G-phase are used to measure the total diffusion of the G-phase forming elements for G-phase precipitation. The activation energy is derived from the total diffusion of involved species and is used to infer the diffusion mechanism. The influence of carbide on the phase separation was quantified and explained in detail.

### 6.1 Spinodal Decomposition

#### 6.1.1 Composition Fluctuation

Proximity histograms of the CF-3 steel, derived from ~20 at. % Cr interconnected isoconcentration surfaces within the ferrite, as shown in Figure 38 confirmed that the Cr peak and trough correspond to the  $\alpha'$ -phase and  $\alpha$ -phase domains, respectively. The mean Cr concentration of the CF-3 had less variation than the CF-8 steel that is rife with Cr-drawing carbides. The mean Cr concentration of the ferrite is indicated by a reference line on each plot. The mean concentration did not evolve over time, but varied with local chemical environment. The Cr fluctuations, however, evolved gradually with time, faster at higher temperatures as shown in Figure 39 and Figure 40 for CF-3 and CF-8 alloys, respectively. The CF-8 curves in Figure 40 were plotted from samples way from carbides, whenever possible. However, a few tip samples had carbides. For the tips without carbides, the distances to the nearest carbide were not measured. The  $\alpha'$ -phase is enriched in Si and the  $\alpha$ -

phase is enriched in Ni. These major G-phase forming elements are ejected from their respective domains unto the interdomain, where they combine to form G-phase precipitates, as discussed below.

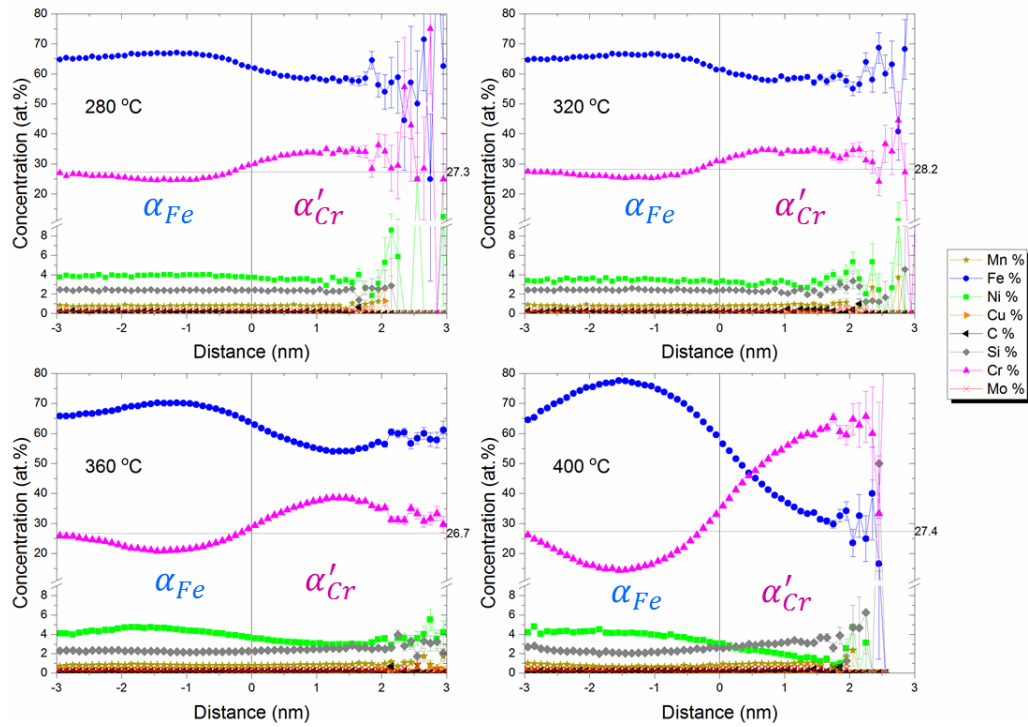


**Figure 38.** Chemical composition of  $\alpha'$ -phase and  $\alpha$ -phase domains in CF-3 samples aged for 17,200 hours at (a) 280 °C, (b) 320 °C, (c) 360 °C, and (d) 400 °C.

CF-3

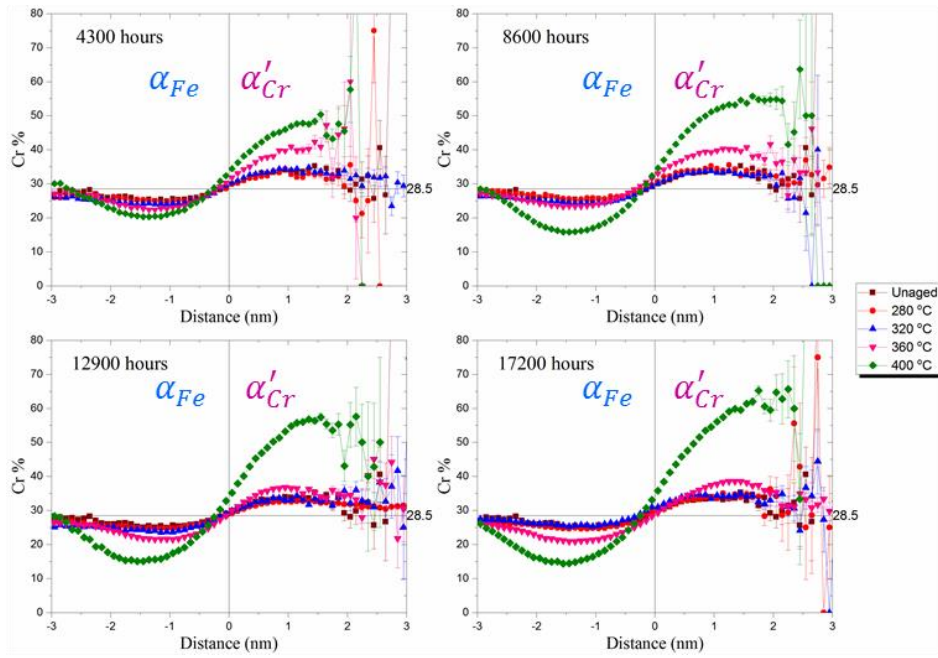


Figure 39. Cr composition in  $\alpha'$ -phase and  $\alpha$ -phase domains in all samples of CF-3 alloy.

CF-8

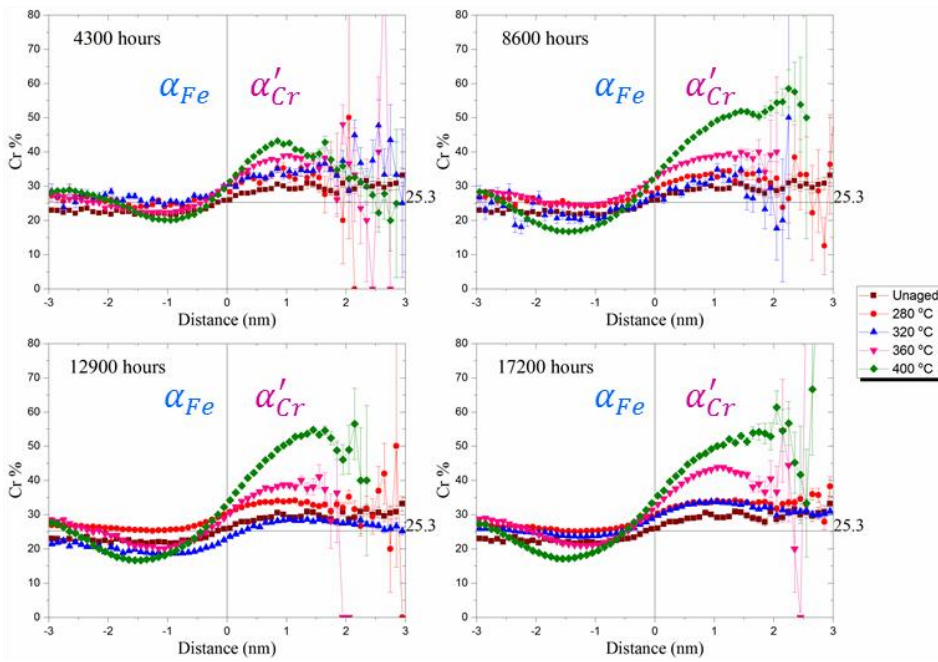
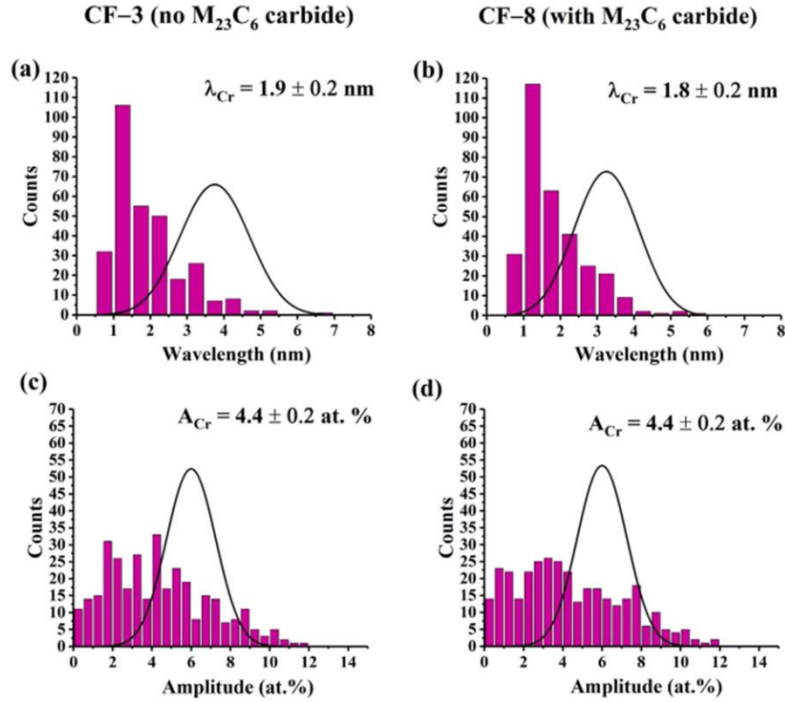


Figure 40. Cr composition in  $\alpha'$ -phase and  $\alpha$ -phase domains in all samples of CF-8 alloy.

### 6.1.2 Wavelength and Amplitude

Spinodal decomposition in CDSS is described as phase separation of the  $\delta$ -ferrite phase into Fe-rich  $\alpha$ -domains (blue) and Cr-rich  $\alpha'$ -domains (magenta). Incipient spinodal decomposition in the ferrite phase of the unaged CDSS was observed. In concurrence with literature, the distribution of the Cr elements had a slight deviation from a random in the as-received condition. This can be attributed to the delay in quenching after the homogenization heat treatments. This shows that microstructural evolution is sensitive to the manufacturing process.

The observations are similar to those in unaged model Fe-25Cr at.%, Fe-30Cr at.%, and Fe-36Cr at.% binary alloys where the authors suggested that small amounts of decomposition may be present in the unaged ferrite phase due to the presence of positive Cr-Cr interactions at short distances when using radial distribution function (RDF) analysis [90]. Moreover, an earlier study by Pumphrey and Akhurst [14] on an unaged CF-3 steel suggested that a small spinodal amplitude exists in the ferrite phase, but the wavelength was not determined. The Cr wavelength and amplitude size distributions in the unaged CF-3 and CF-8 stainless steels are illustrated in Figure 41 (a) – (d). The binomial distribution of random wavelengths and amplitudes are superimposed on both figures and differ from the experimentally measured distributions. The quantity MW (Mean Wavelength derived from sinusoidal curves) for Cr in CF-3 is  $1.9 \pm 0.2$  nm and  $1.8 \pm 0.2$  nm in CF-8. The quantity MA (Mean Amplitude derived from sinusoidal curves) for Cr in the CF-3 steel is  $4.4 \pm 0.2$  nm and  $4.4 \pm 0.2$  nm in the CF-8 steel.



**Figure 41.** Wavelength size distributions of unaged (a) CF-3 and (b) CF-8 alloy. Amplitude size distributions of unaged (c) CF-3 and (d) CF-8 alloy.

Phase decomposition in the ferrite phase is shown to progress and the wavelength and amplitudes of the concentration fluctuations increased during aging as illustrated for both steels at all aging conditions, Figure 42(a) – (d). Additionally, a small G-phase precipitate of a CF-8 sample aged to 4300 h at 400 °C is observed at an  $\alpha$ -domain/ $\alpha'$ -domain interface in Figure 16 and is discussed below. The CF-3 steel has a consistent increase of wavelength and amplitude values compared to the CF-8 steel. Comparing the evolution of the two alloys, the data clearly show that spinodal decomposition is less developed in CF-8 than in CF-3. The amplitude values of the two alloys were comparable; however, the wavelength was smaller in the CF-8 alloy. The local environment of the CF-3 steel is more consistent than the CF-8, in which some samples had close proximity to carbides, while others did not.

For this reason, only the values from the CF-3 steels will be analyzed for calculating the activation energies, as will be discussed below.

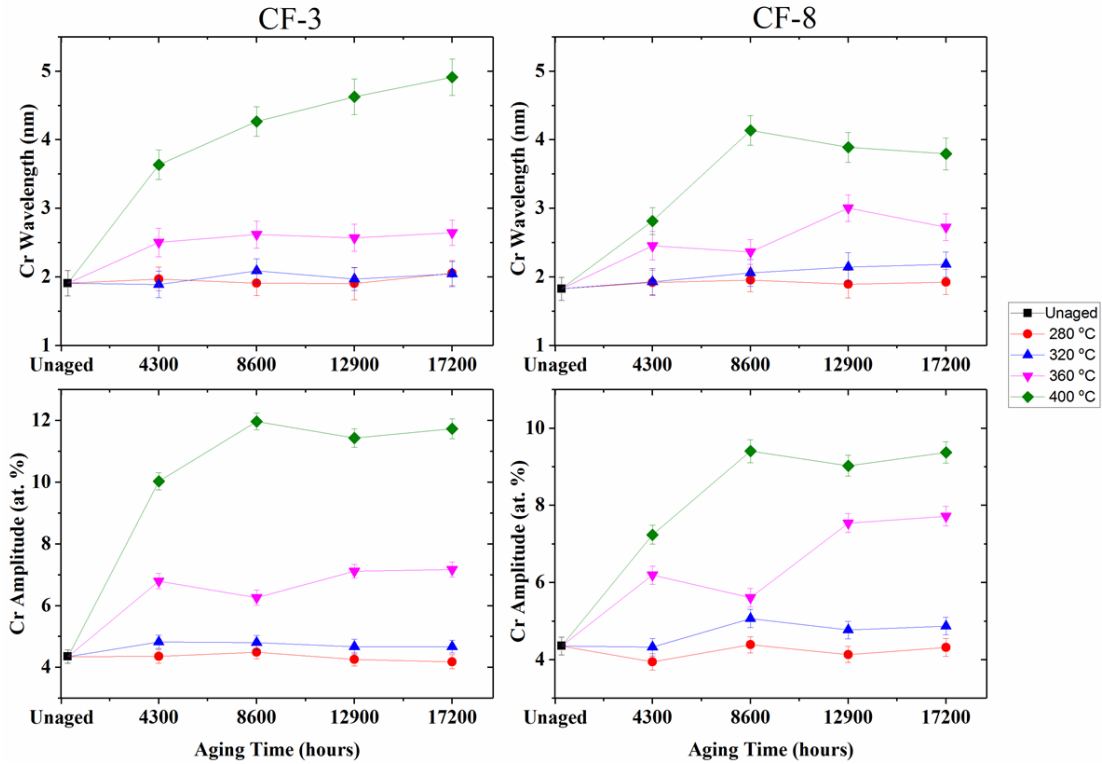


**Figure 42.** Increase of wavelength in (a) CF-3 and (b) CF-8 alloy during thermal aging. Increase of amplitude in (c) CF-3 and (d) CF-8 alloy during thermal aging.

The quantities MW and MA demonstrate an increasing upward trend with increasing aging temperature and time. The values are larger for both accelerated temperatures when compared to the operational temperatures of both steels. Only small differences exist in the quantities MW and MA between the two steels at operational temperatures. The larger MW and MA values at accelerated temperatures may be influenced by the G-phase precipitates on spinodal decomposition, as discussed below.

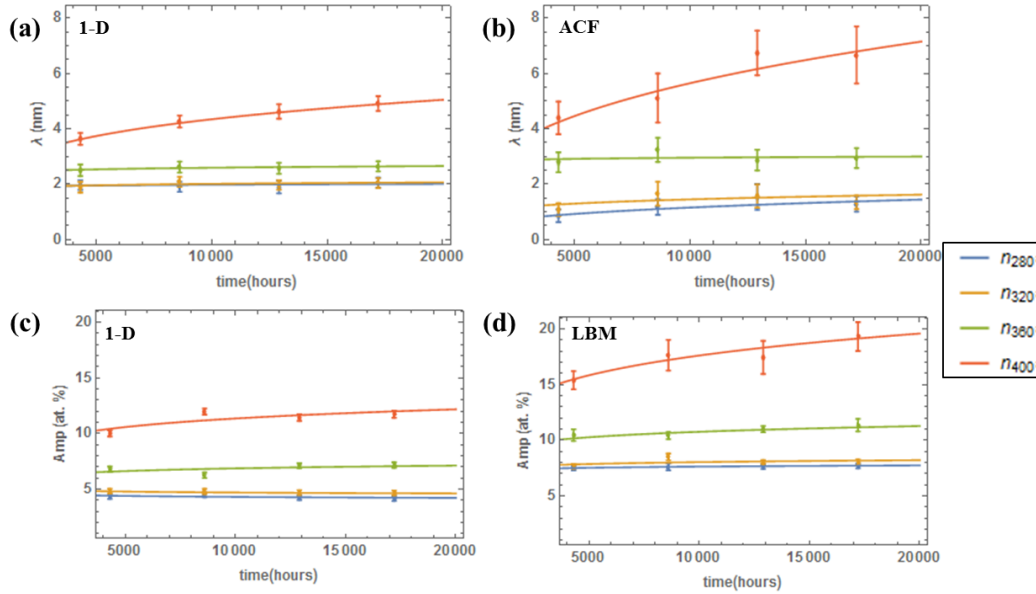


**Figure 43.** Comparison of the developed 1-D concentration profile to the other traditional methods in measuring wavelengths and amplitudes. Wavelength values with (a) 1-D method and (b) ACF methods. Amplitude values with (c) 1-D method and (d) LBM methods.

The quantity of MW has slight differences when compared to the mean wavelength determined by the ACF method, but both methods illustrate similar trends, Figure 43. The amplitude determined by the LBM method is consistently greater than the quantity of MA, but both methods exhibit similar trends, Figure 43. Earlier studies of evaluating spinodal decomposition have illustrated quantitative differences between various methods of determining amplitude although they may exhibit similar trends [73] and [90]. In this study, the differences observed between the LBM method and the quantity MA is due to their underlying basis. The LBM method is categorized as a peak-to-trough amplitude method, whereas the method presented in this study is a peak-to-mean composition amplitude method and thus the former will have quantitative values approximately twice as great as the latter. Furthermore, the LBM method is dependent on symmetry of the frequency distributions [90], and multicomponent alloys whose nominal or local compositions

are not centered in the miscibility gap of the phase diagram, such as the CF-3 and CF-8 CDSS in this study, will exhibit asymmetry and thus the LBM method can produce greater variability in its results.

## 6.2 G-phase Forming Zones

### 6.2.1 Composition

The G-phase precipitate is a ternary intermetallic silicide that has a nominal stoichiometric composition of  $\text{Ni}_{16}\text{Si}_7\text{Ti}_6$  [91]. Other metallic elements such as Cr, Fe, and Mn can substitute for Ni and titanium (Ti) [4], [91], and [49]. Proximity histograms derived from ~2.5 at. % Ni interconnected isosurfaces within the ferrite of CF-3 samples show an increase in the composition of G-phase forming elements on the right of the reference point, Figure 44 (a) – (d). The composition on the left side is the average of the ferrite matrix that has spinodally decomposed into  $\alpha/\alpha'$  domains. The proxigrams show that the G-phase precipitates are enriched in Ni, Si, Mn, and Cu but are depleted in Fe and Cr. Copper is present as a residual element in the steels and may be the  $\epsilon$ -Cu phase that acts as a nucleation site for G-phase precipitation as observed by other researchers [50]. The G-phase compositions still contain measurable concentrations of Fe and Cr. Both elements diffuse out of the G-phase while Ni, Si, and Mn diffuse into the G-phase during further aging as the precipitates approach their equilibrium compositions. Trajectory aberrations and local magnifications effects may also influence the Fe and Cr concentrations in the G-phase. However, since the mean radius quantity  $\langle R \rangle$  is  $> 1$  nm, this will have limited effect on the core compositions [92]. Recent studies of the G-phase in CF-3M illustrated that Fe and Cr concentrations decrease while Ni, Mn, Si, and Mo

concentrations increase in the precipitates with increasing aging time at accelerated temperatures [3] and [5].

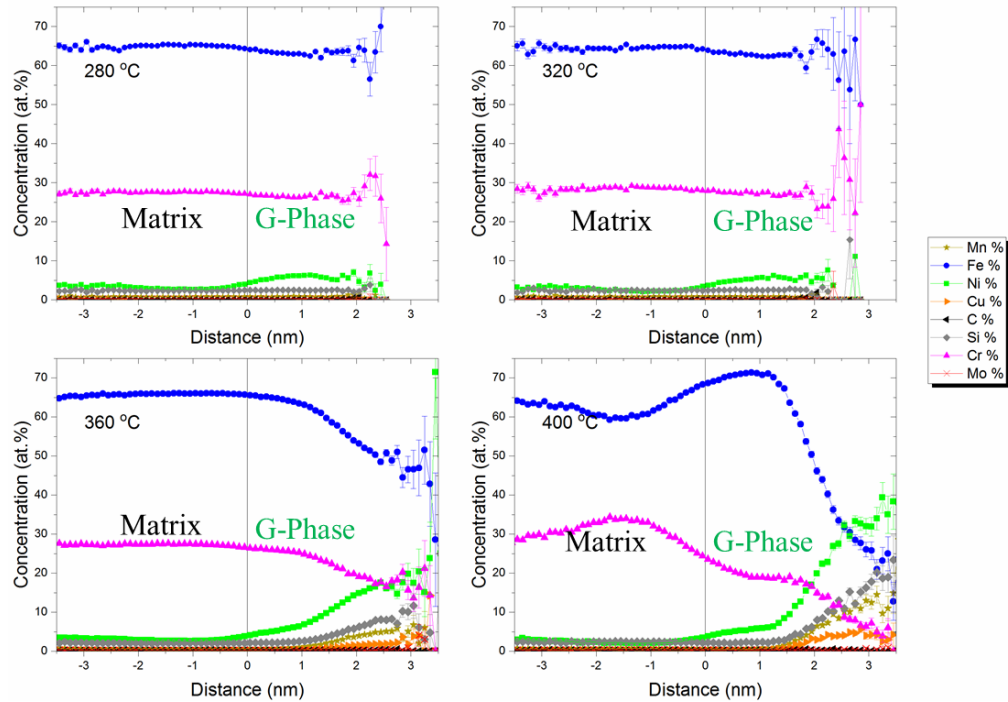


**Figure 44.** Chemical composition of possible G-phase forming zones in CF-3 steel after 17200 hours of thermal aging at (a) 280 °C, (b) 320 °C, (c) 360 °C, and (d) 400 °C.

In spinodal decomposition, the  $\alpha'$ -domain becomes more enriched in Cr, while losing Fe to the  $\alpha$ -domain and Si to the G-phase precipitate. Therefore, only the Cr concentration was taken into consideration when computing the wavelength and amplitude. In contradistinction, the G-phase precipitate is enriched not only in Ni, but also Si, and Mn. In literature, Mo, Cu, and C are believed to also participate [5]. Fe and Cr can substitute for Ni and Mn, but they will eventually diffuse out and be replaced as the G-phase composition approaches equilibrium. Therefore, the G-phase precipitate concentration is the sum of Ni, Si, Mn, Mo, Cu, and C, and not just a single element like for spinodal decomposition. Figure 45 and Figure 46 display only the Ni concentration in G-phase forming zones in the CF-3 and CF-8 alloys, respectively. Comparing to Figure 47, displaying the summation of all G-phase

forming elements compositions in the CF-3 alloy, it is clear that Ni is the major element.

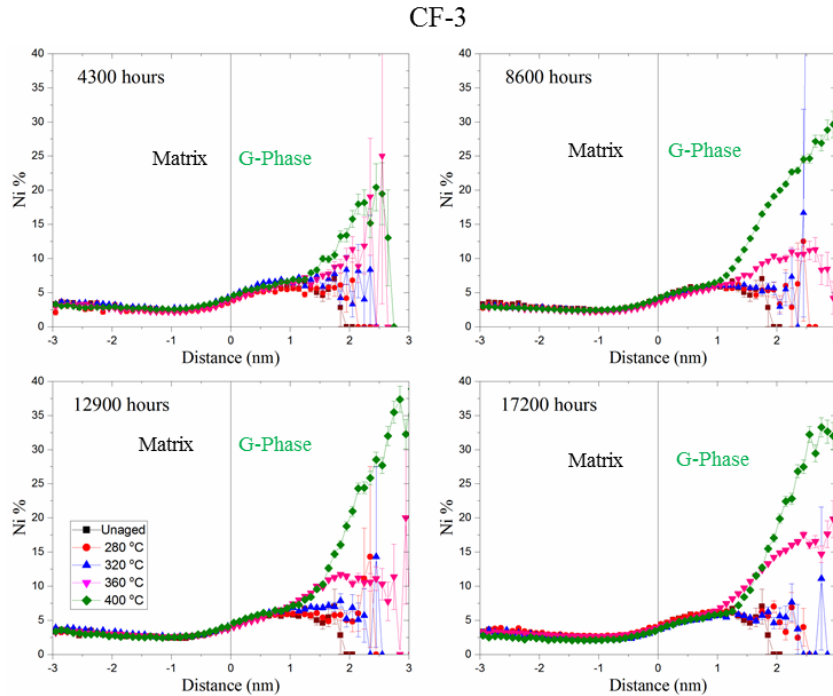


**Figure 45.** Ni composition in CF-3 steels at all aging conditions.

The kinetics of G-phase precipitation are slower at 360 °C than at 400 °C. This is supported by the lower Fe and Cr concentrations and concomitantly higher Ni, Si, and Mn concentrations at 400 °C aging when compared to 360 °C aging for both steels. In Figure 45, Figure 46, and Figure 47, the Ni concentration of CF-3 steel, the Ni concentration of CF-8 steel, and the sum of compositions of G-phase forming elements, Ni, Si, Mn, Cu, Mo, and C in CF-3 steel, were plotted, respectively, at all aging conditions for both steels. From these plots, the composition amplitude was calculated by subtracting the values obtained from 10 left-hand-side points and 10 right-hand-side points.

## CF-8

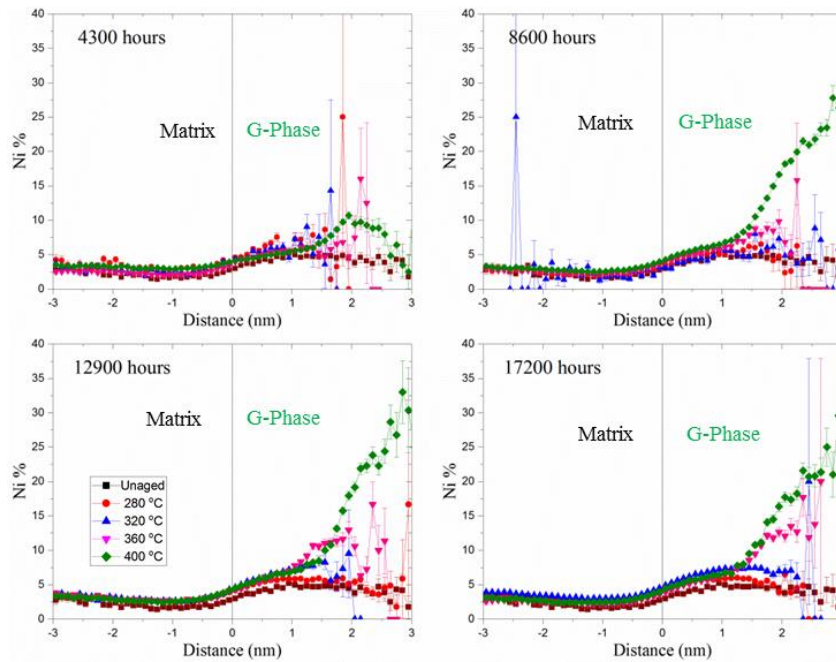


**Figure 46.** Ni composition in CF-8 steels at all aging conditions.

Similar to the spinodal decomposition concentrations in Figure 39 and Figure 40, the same samples were used in plotting the G-phase compositions. The CF-8 samples without carbides on the tip were chosen, if available. The abrupt increase in G-phase composition is apparent between the 4300 and 8600 hours aging at 400 °C and between the 12900 and 17200 hours aging at 360 °C. This abrupt increase in G-phase precipitation at different times and temperatures is likely due to the nucleation and growth of G-phase precipitates, which requires a two-stage process of expelling Ni from  $\alpha'$ -domain and Si from  $\alpha$ -domain followed by precipitate nucleation at the  $\alpha/\alpha'$  interface. In the first step, the G-phase forming zone reaches a critical composition, and in the second step, the G-phase forming elements rearrange their respective lattice positions to form a critical radius. In contrast, the increase in wavelength and amplitude in spinodal decomposition was continuous, with no obvious abrupt

changes. The wavelength and amplitudes appear to be still increasing at 17,200 at all temperatures. However, for the G-phase precipitate at 400 °C, the composition does not change after 8,600 hours. More time is needed at the 360 °C to note when the composition stays constant.

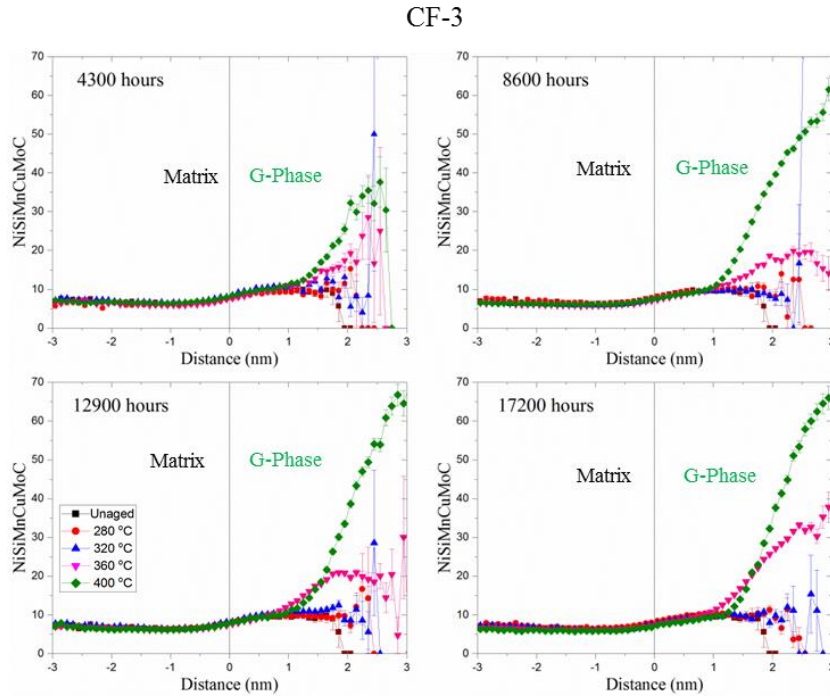


**Figure 47.** G-phase forming elements composition in CF-3 steels at all aging conditions.

### 6.2.2 Radius ( $\langle R \rangle$ ), Number Density ( $N_v$ ), and Volume Percentage ( $V_p$ )

The APT as a characterization method for G-phase allows for high resolution and quantitative characterization of very fine particles. The forming G-phase precipitates mean radius sizes ( $\langle R \rangle$ ), number density ( $N_v$ ), and volume percentages ( $V_p$ ) were quantified using a delineation of 6.5 at. % Ni isoconcentration surfaces. These G-phase precipitates were not observed in the unaged specimens or the

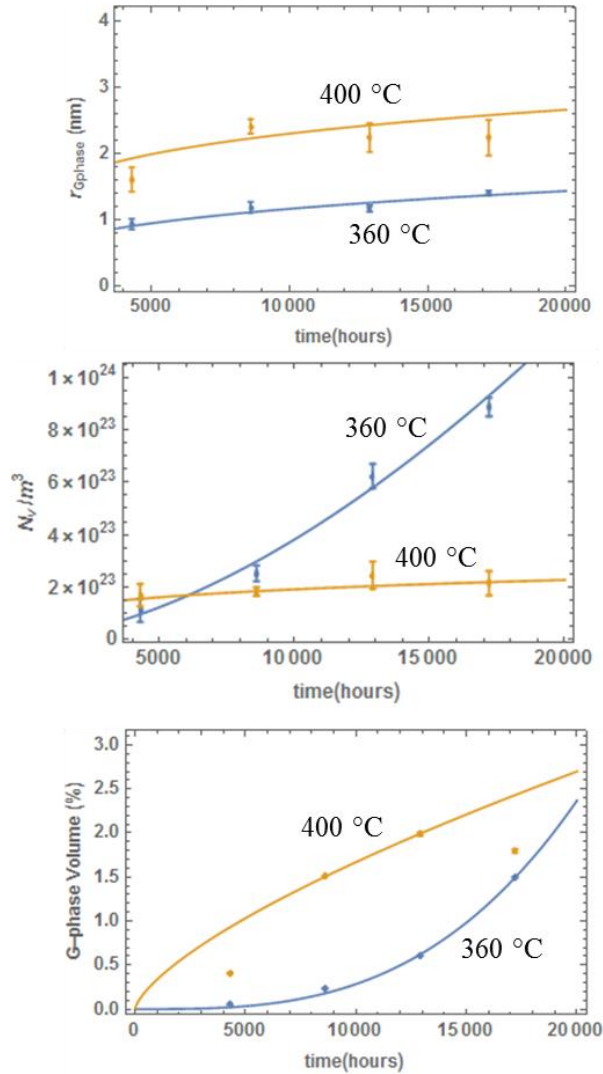


**Figure 48.** Plot of (a) radius:  $\langle R \rangle$ , (b) number density:  $N_v$ , and (c) volume percentage:  $V_p$  of G-phase precipitates in CF-3 steel.

specimens aged at operational temperatures in both steels, and therefore only the data at accelerated temperatures are plotted for the CF-3 alloy, Figure 48.

The G-phase precipitation system is non-ideal and does not meet the LSW requirements. The clusters of G-phase forming elements nucleate and grow at different times and locations. Overtime, as shown in Figure 49 and Figure 50, for CF-3 and CF-8 alloys respectively, the clusters of Ni, Si, Mn, and Cu atoms coalesce to form constellation of clusters, which would eventually become a G-phase precipitate.

As the size of the cluster increases, the composition of the G-phase forming elements increases. Since only the 6.5 at. % Ni isosurfaces are measured, the size, number density, and volume fraction of disjointed clusters may be underestimated at lower times in accelerated temperature samples and perhaps at all the operational temperature samples.

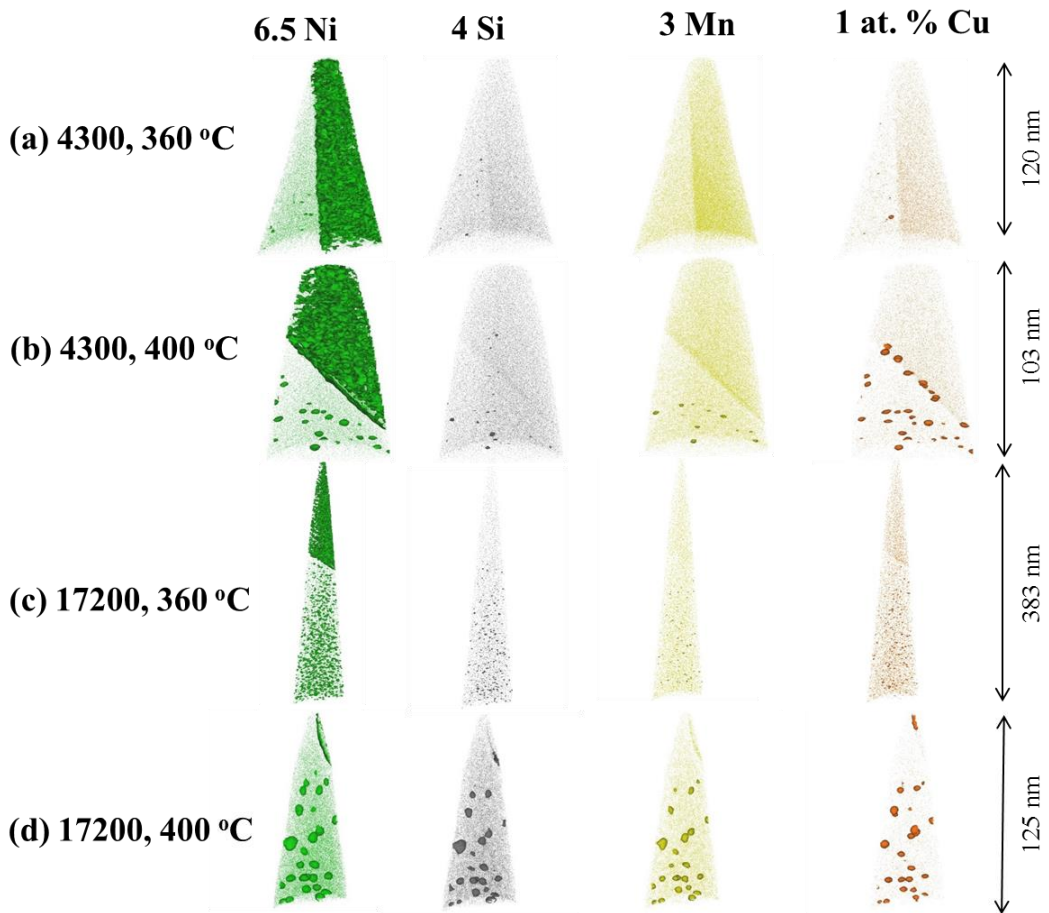


**Figure 49.** Coalescence of Ni-Si-Mn-Cu clusters in CF-3 steel of samples aged for (a) 4300 h at 360 °C, (b) 4300 h at 400 °C, (c) 17200 h at 360 °C, and (d) 17200 h at 400 °C.

The volume fractions of the G-phase precipitates were calculated by summing the volumes from all precipitates and dividing the sum to the volume of the sample tip. This is analogous to multiplying the numbers density by the average radius volume of a sphere. The volume fraction increases and approaches equilibrium when

the number density decreases during the coarsening regime. The volume fraction of the 400 °C data was initially higher due to a large  $N_v$  and  $\langle R \rangle$ . As the aging time progressed, the  $N_v$  of 360 °C was much higher than that of 400 °C. Therefore, the volume fractions of the data are about equal after 2 years of aging. The rate of increase, as indicated by the time exponent, is much higher for 360 °C than 400 °C. Since the  $\langle R \rangle$  and  $N_v$  of the G-phase precipitates at 360 °C and 400 °C are different, the volume fraction is more suitable for comparison at all temperatures.

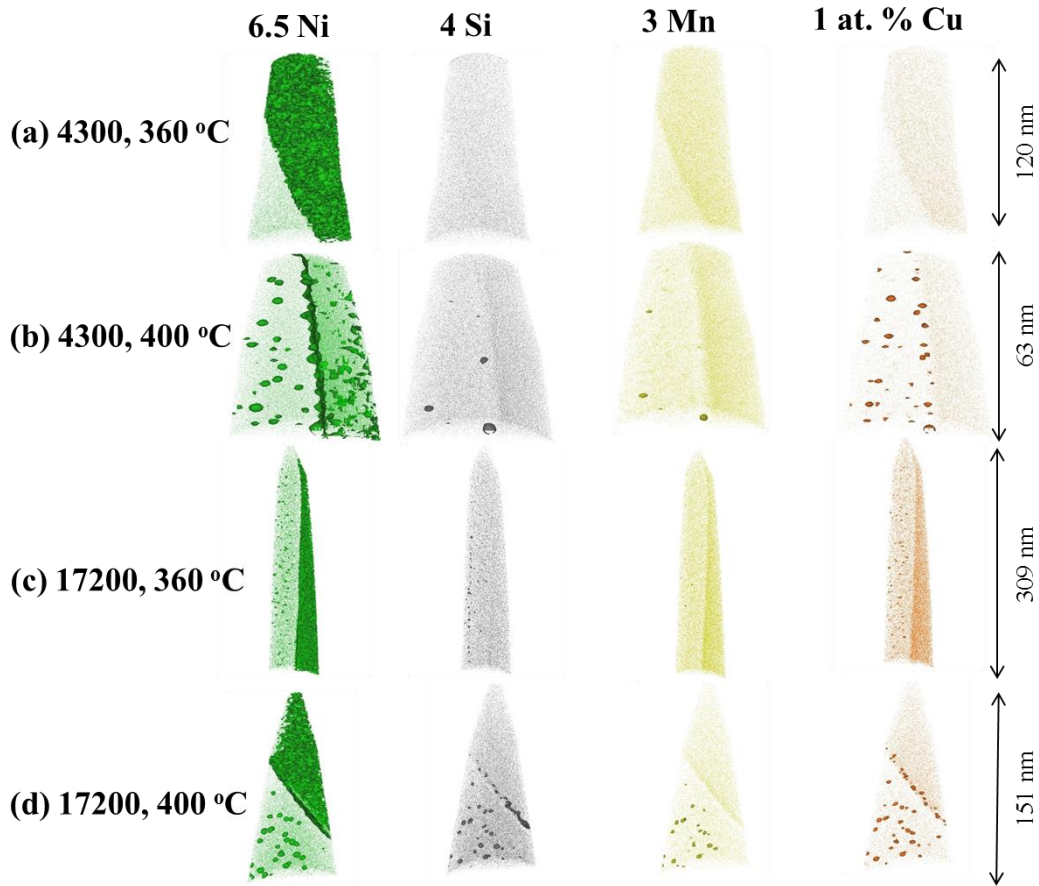


**Figure 50.** Coalescence of Ni-Si-Mn-Cu clusters in CF-8 steel of samples aged for (a) 4300 h at 360 °C, (b) 4300 h at 400 °C, (c) 17200 h at 360 °C, and (d) 17200 h at 400 °C.

Similar to the D.o.D in spinodal decomposition, the composition of the G-phase precipitates should also be taken into account. The G-phase ‘volume’, also

referred to as the D.o.D, was calculated by multiplying the concentration amplitude from the mean composition to the volume fraction.

### 6.3 Time Exponents

#### 6.3.1 Spinodal Decomposition

The calculated time exponents of the wavelengths and amplitudes convey an earlier assertion by Zhou et al [90], [93], [94], that the values of time exponents are method dependent. Even though there are similar trends and values for MW with ACF and MA with LBM, the time exponents vary widely, Table 4. Therefore, drawing conclusions on the diffusion mechanisms based on interpreting time exponents can be erroneous on two conditions: spinodal decomposition is a complex system that does not meet the requirements for the LSW theory and the aging times observed in this study were too short for effective analysis.

**Table 4.** Time exponents of wavelengths and amplitudes by in-lab, ACF, and LBM methods.

Temp	Wavelength: $\lambda = kt^n$		Amplitude: $A = kt^n$	
	In-lab	ACF	In-lab	LBM
280 °C	0.02 ± 0.09	0.32 ± 0.24	-0.03 ± 0.05	0.02 ± 0.02
320 °C	0.04 ± 0.09	0.16 ± 0.9	-0.03 ± 0.04	0.03 ± 0.03
360 °C	0.03 ± 0.08	0.02 ± 0.12	0.05 ± 0.03	0.07 ± 0.04
400 °C	0.22 ± 0.06	0.34 ± 0.13	0.10 ± 0.03	0.15 ± 0.06

The time exponents based on the LSW theory were found not to give consistent values depending on the method applied to measure the increase of wavelength and amplitude. Zhou et al [90] concluded similarly and developed the Radial Distribution Function (RDF) method to simultaneously measure the wavelength and amplitude for consistency. At low temperatures, the average wavelength time exponents calculated by the in-lab method developed in this

investigation were less than 0.05. However, the ACF method applied to the same samples gave an average time exponent of 0.32 at 280 °C, 0.16 at 320 °C, 0.02 at 360 °C, and 0.34 at 400 °C. In literature, the increase of wavelength time exponent values from 0.15 to 0.33 inclusive indicates a transition from the dislocation to bulk diffusion mechanism, respectively. However, not all results in literature had expected results; some reported very low time exponents similar to the 0.02 value measured at 360 °C. Due to the variability from sample to sample and the method employed, it is logical to conclude that the LSW theory time exponents are not an appropriate method of describing kinetics in complex systems, where size, concentration, and/or volume fraction may be increasing altogether.

### 6.3.2 G-phase Forming Zones

The radius, number density, and volume fraction of G-phase forming zones were quantified. They were delineated by a 6.5 at. % Ni isoconcentration surface. These surfaces were only found in the ferrite phases at the two accelerated temperatures. The radii of the G-phase forming zones were larger at 400 °C and the number densities were larger at 360 °C. The volume fractions were calculated from both the radius and number density. At first, the volume fraction of the G-phase was greater at 400 °C. As time progressed, the volume fraction at 360 °C approached that of 400 °C. There is a progression of G-phase formation to occur at lower temperatures because there is a tendency of increasing Ni concentration. The Ni concentration at low temperatures does not reach the 6.5 at.% threshold for detection within two years. However, the trend suggests that the G-phase will form beyond 2 years at low temperatures.

The time exponent of the radius in Table 5 shows that value at 400 °C is within error to that of the wavelength measured by both in-lab and ACF methods. Danoix et al [8] compared the time exponents of the spinodal decomposition wavelength and G-phase radius to suggest that their kinetics were linked. However, the time exponents are not reliant in describing the kinetics of complex systems.

**Table 5.** Time exponents of G-phase radius, number density, and volume percent

<b>Temp</b>	<b>Radius: <math>r = kt^n</math></b>	<b>Number Density: <math>N_v = kt^n</math></b>	<b>Volume Percentage: <math>V_p = kt^n</math></b>
<b>360 °C</b>	0.3 ± 0.06	1.65 ± 0.15	3.05 ± 0.00
<b>400 °C</b>	0.21 ± 0.11	0.25 ± 0.22	0.69 ± 0.01

#### 6.4 Degree of Decomposition (D.o.D)

##### 6.4.1 Spinodal Decomposition

In a spinodal decomposition system, the volume fractions of the interconnected Cr-rich domains ( $\alpha'$ -phase) and Cr-lean domains ( $\alpha$ -phase) domains do not change, as indicated by similar Fe and Cr wavelengths throughout the aging period. However, even with a constant volume fraction, not only were the sizes (wavelengths) of the domains increasing, but also the amplitudes (concentrations) within those domains were increasing. Therefore to describe the kinetics of such a complex system, the method termed D.o.D was developed to calculate the total diffusion by multiplying the cubed wavelength by the amplitude.

##### 6.4.2 G-phase Forming Zones

The D.o.D for G-phase precipitation was calculated in the same fashion as of the spinodal decomposition with some difference. For the G-phase forming zones, the D.o.D was calculated by multiplying the volume fraction to the amplitude because

the number density of G-phase is increasing unlike the constant volume fraction in spinodal decomposition.

### 6.5 Activation Energy

The thermal activation energy is the key parameter for using the common activation model of an Arrhenius-type equation. Assuming the same diffusion distance  $x_1 = x_2$  at high temperatures (1) and low temperatures (2), we can relate the diffusion distance,  $x_i = \sqrt{D t}$ , to the total diffusion in a given time,  $D_1 t_1 = D_2 t_2$ . The activation energy of diffusion is given by  $D_i = D_o e^{-Q/RT}$ . By plugging into the equations, we derive the Arrhenius equation,  $\ln\left[\frac{t_1}{t_2}\right] = \frac{Q}{R} \left(\frac{1}{T_1} - \frac{1}{T_2}\right)$  to relate two times and two temperatures with the same mechanism of activation energy, Q. However, even if the same microstructural mechanisms occur in both the service and the accelerated aging experiment, the relative contributions of those mechanisms will change with temperature and thus the mechanism-averaged activation energy should vary with aging temperature. Therefore, with multiple kinetic factors in play, a careful analysis is needed to justify an extrapolation of data obtained for high temperatures to predict the extent of thermal embrittlement at reactor temperatures.

#### 6.5.1 Spinodal Decomposition

The change of slope in the  $\ln[D.o.D]$  vs  $1/T$  plot from high to low temperatures shows that there is a change in mechanism. The activation energy of D.o.D is the summation from contributions of the cubed wavelength ‘volume’ and the amplitude. It is clear that D.o.D takes the total diffused Cr atoms to accurately measure the activation energy. For instance, in the CF-3 sample aged for 17200

hours, the high temperature activation energy was:  $43.6 \pm 3.8 \text{ kJ/mol}$  using amplitude, (Figure 51),  $165 \pm 23 \text{ kJ/mol}$  using cubed wavelength, (Figure 52), and  $208 \pm 23 \text{ kJ/mol}$  using D.o.D, (Figure 53). The activation energy of Cr diffusion in the ferrite lattice is within that range [39]. The bulk activation energy of D.o.D increased with a decreasing rate as a function of time. This follows well with the progress of spinodal decomposition wavelength and amplitude values, whose values increased with a decreasing rate as they approached equilibrium. At 4300 h,  $Q_{Cr}^{high T} = 134 \pm 27 \text{ kJ/mol}$ , the activation value is low probably due to the available pipe diffusion in dislocations. At 8600 h,  $Q_{Cr}^{high T} = 187 \pm 25 \text{ kJ/mol}$ , the activation value increased probably due to annihilation of dislocation, leaving bulk diffusion as the only diffusion path. At 12900 h,  $Q_{Cr}^{high T} = 197 \pm 26 \text{ kJ/mol}$ , the activation value indicates bulk diffusion. At 17200 h,  $Q_{Cr}^{high T} = 208 \pm 23 \text{ kJ/mol}$ , the activation value indicates bulk diffusion. The kinetics of diffusion at low temperatures were too slow. The calculated activation energies varied with low numbers and high error values.

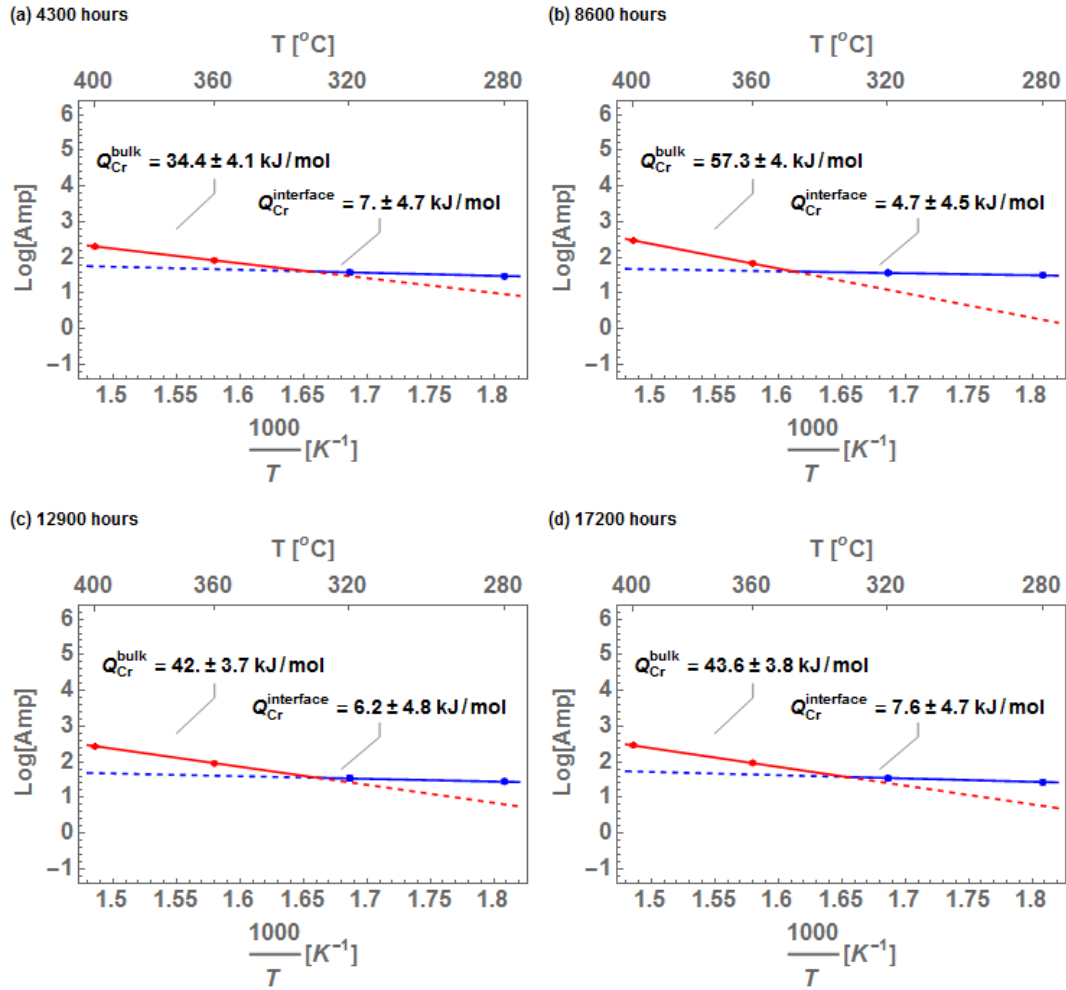


**Figure 51.** Activation energy of spinodal decomposition derived from only the amplitude component of D.o.D at low operational (blue) and high accelerated (red) temperatures at (a) 4300 h, (b) 8600 h, (c) 12900 h and (d) 17200 h.

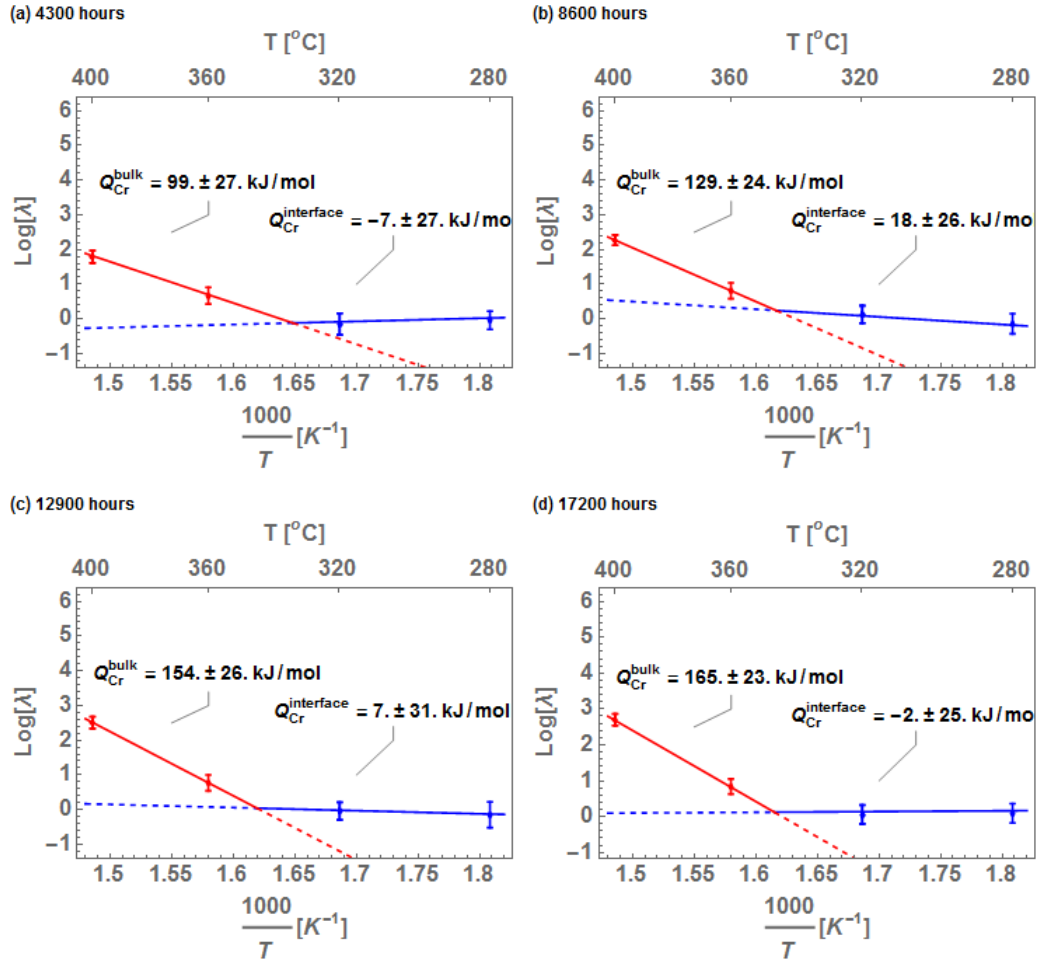


**Figure 52.** Activation energy of spinodal decomposition derived from only the wavelength component of D.o.D at low operational (blue) and high accelerated (red) temperatures at (a) 4300 h, (b) 8600 h, (c) 12900 h and (d) 17200 h.

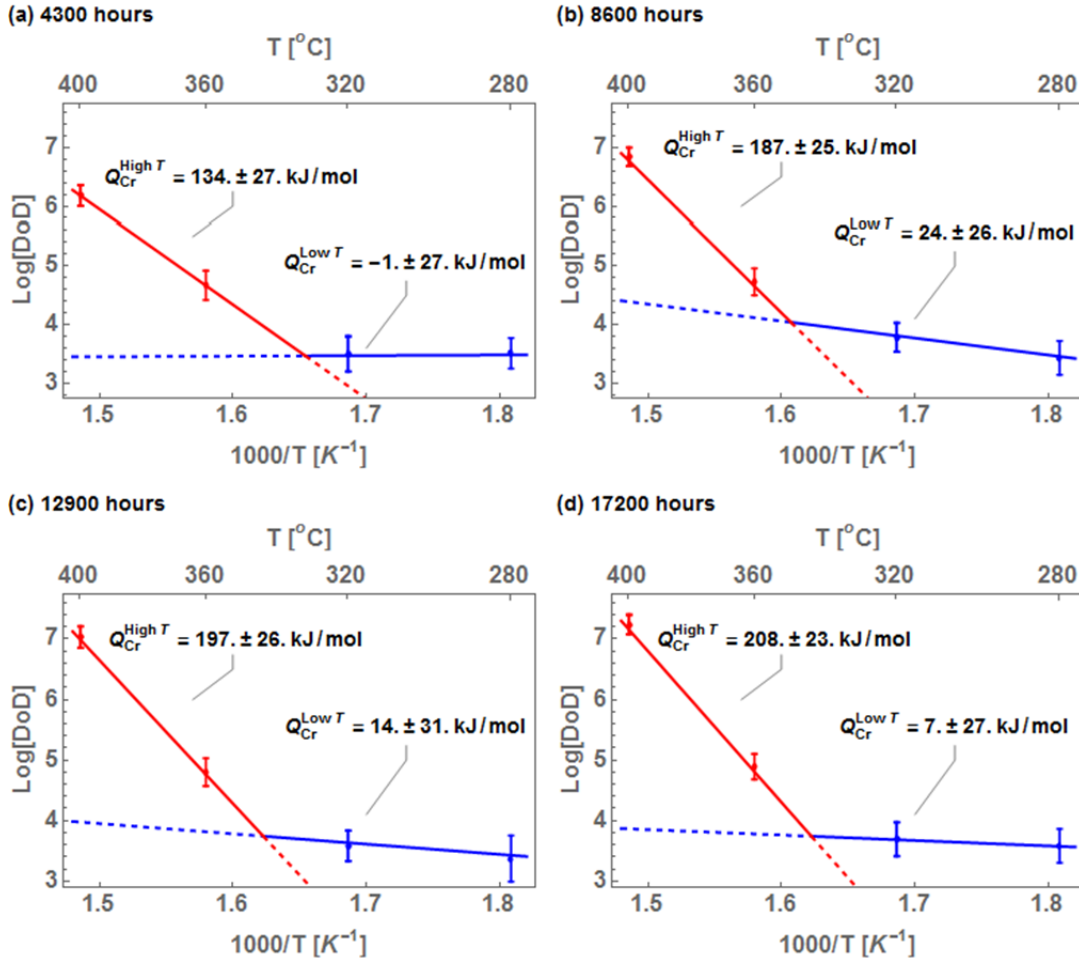


**Figure 53.** Activation energy of spinodal decomposition derived from both amplitude and wavelength components of D.o.D at low operational (blue) and high accelerated (red) temperatures at (a) 4300 h, (b) 8600 h, (c) 12900 h and (d) 17200 h.

### 6.5.2 G-phase Forming Zones

The change of slope in the  $\text{Ln}[\text{D.o.D}]$  vs  $1/T$  plot from high to low temperatures indicates that there is a change in diffusion mechanism. The activation energy of D.o.D is the summation from contributions of the G-phase volume fraction and the composition amplitude of the G-phase elements. The volume fraction was calculated from the 6.5 at. % Ni isosurfaces, while the G-phase elements are Ni, Si, Mn, Mo, Cu, and C. Figure 49 and Figure 50 shows that at shorter aging times and lower temperatures, the isosurfaces of Ni, Si, Mn, and Cu are not in the same location

for CF-3 and CF-8 alloys, respectively. This indicates that the clusters of these elements need to diffuse to the same location and arrange themselves in the G-phase lattice. Since only the Ni isosurfaces are taken into account, this method slightly underestimates the volume fractions, especially at the shorter times and lower temperatures. In the operational temperatures, a volume fraction of 0.01 % had to be assumed because the actual values were orders of magnitude smaller. The slopes and resulting activations energy derived from the actual volume fractions were too high and nonsensical. G-phase precipitation follows a nucleation and growth mechanism while  $\alpha'$ -phase follows a spinodal decomposition mechanism.

The activation energies from the slopes changed as the growth stage regime of the G-phase precipitate occurred at different times and temperatures. For instance, the activation energy in the CF-3 sample aged for 8600 hours, the high temperature activation energy was:  $145 \pm 14 \text{ kJ/mol}$  using amplitude (Figure 54),  $164.7 \pm 0.4 \text{ kJ/mol}$  using volume fraction (Figure 55), and  $310 \pm 15 \text{ kJ/mol}$  using D.o.D (Figure 56), which is the summation of the activation energies from the volume fractions and amplitude. In the CF-3 sample aged for 17200 hours, the bulk activation energy was:  $77 \pm 12 \text{ kJ/mol}$  using amplitude (Figure 54),  $16.2 \pm 1 \text{ kJ/mol}$  using volume fraction (Figure 55), and  $92 \pm 12 \text{ kJ/mol}$  using D.o.D (Figure 56). The bulk activation energy of D.o.D increased and then decreased with time. This agrees with the mechanism of nucleation and growth, in which there is an incubation period before the G-phase precipitate nucleates and grows. This incubation period depends on temperature. At 4300 h,  $Q_{\text{Elements}}^{\text{high } T} = 249 \pm 18 \text{ kJ/mol}$ , the activation value is relatively low probably due to the available pipe diffusion

in dislocations. At 8600 h,  $Q_{G_{elements}}^{high T} = 310 \pm 15 \text{ kJ/mol}$ , the activation value increased probably due to annihilation of dislocation, leaving bulk diffusion as the only diffusion path. At 12900 h,  $Q_{G_{elements}}^{high T} = 261 \pm 17 \text{ kJ/mol}$ , the activation value decreased, probably due to distinct spinodal decomposition domain interfaces to facilitate diffusion. At 17200 h,  $Q_{G_{elements}}^{high T} = 92 \pm 12 \text{ kJ/mol}$ , the activation value decreased even more to indicate G-phase coarsening through interface diffusion along the developed  $\alpha/\alpha'$  interfaces. The kinetics of diffusion at low temperatures was too slow. The calculated activation energies varied with low numbers and high error values.

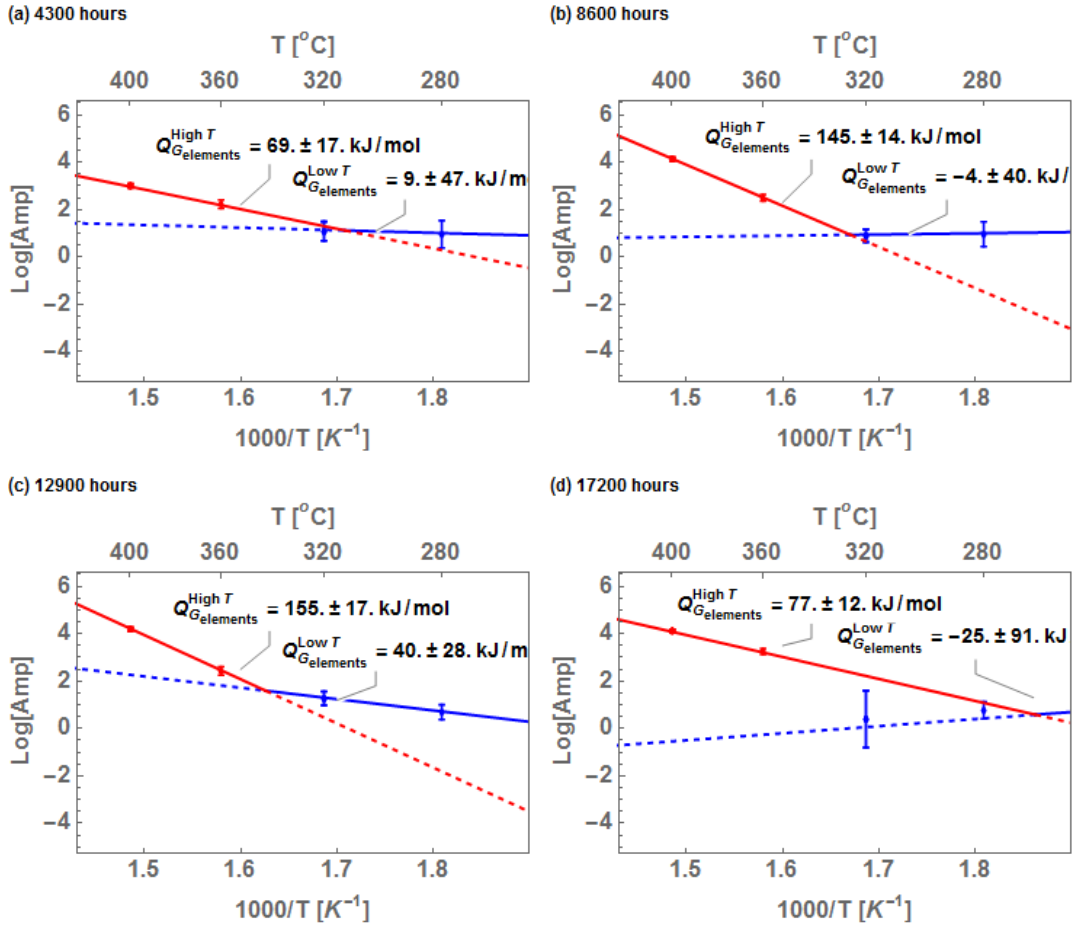


**Figure 54.** Activation energy of G-phase precipitation derived from the amplitude component of D.o.D at low operational (blue) and high accelerated (red) temperatures at (a) 4300 h, (b) 8600 h, (c) 12900 h and (d) 17200 h.

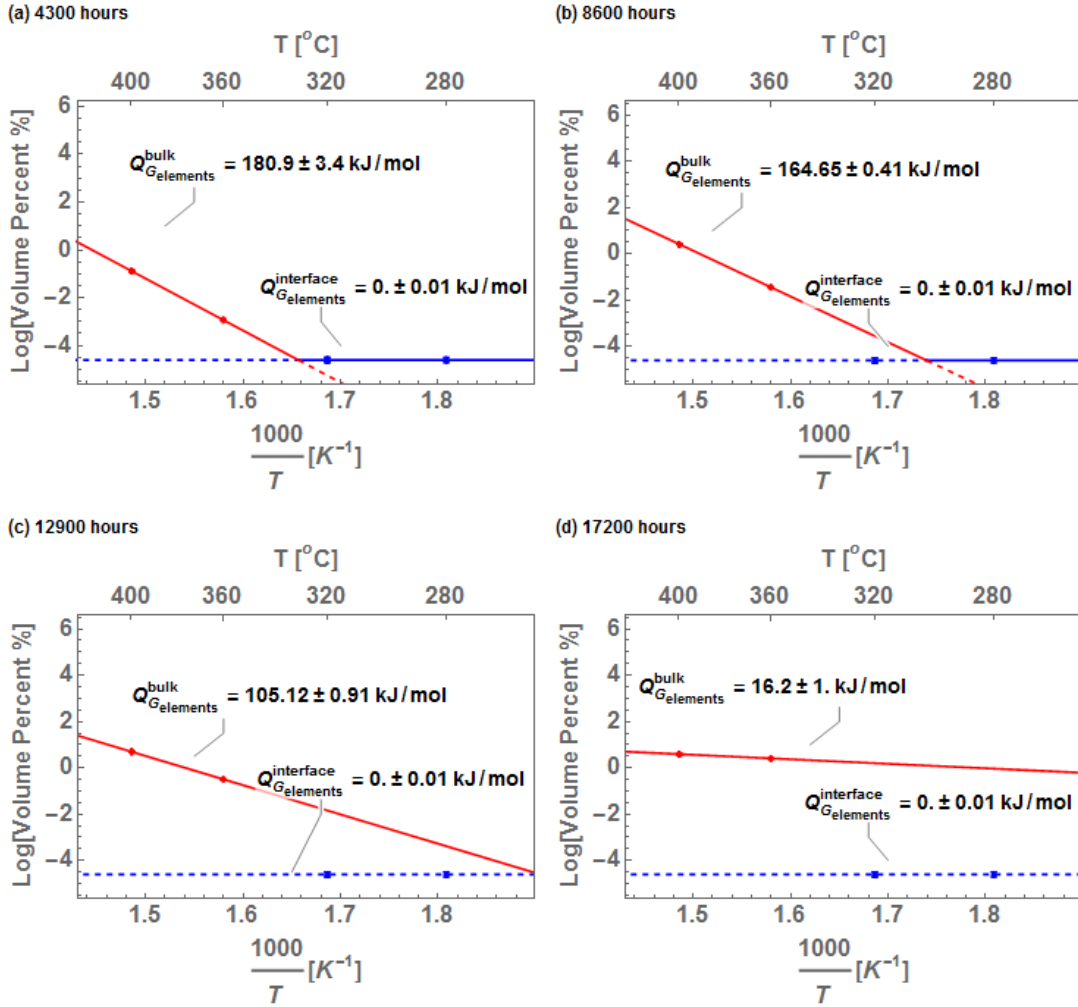


**Figure 55.** Activation energy of G-phase precipitation derived from the volume fraction component of D.o.D at low operational (blue) and high accelerated (red) temperatures at (a) 4300 h, (b) 8600 h, (c) 12900 h and (d) 17200 h.

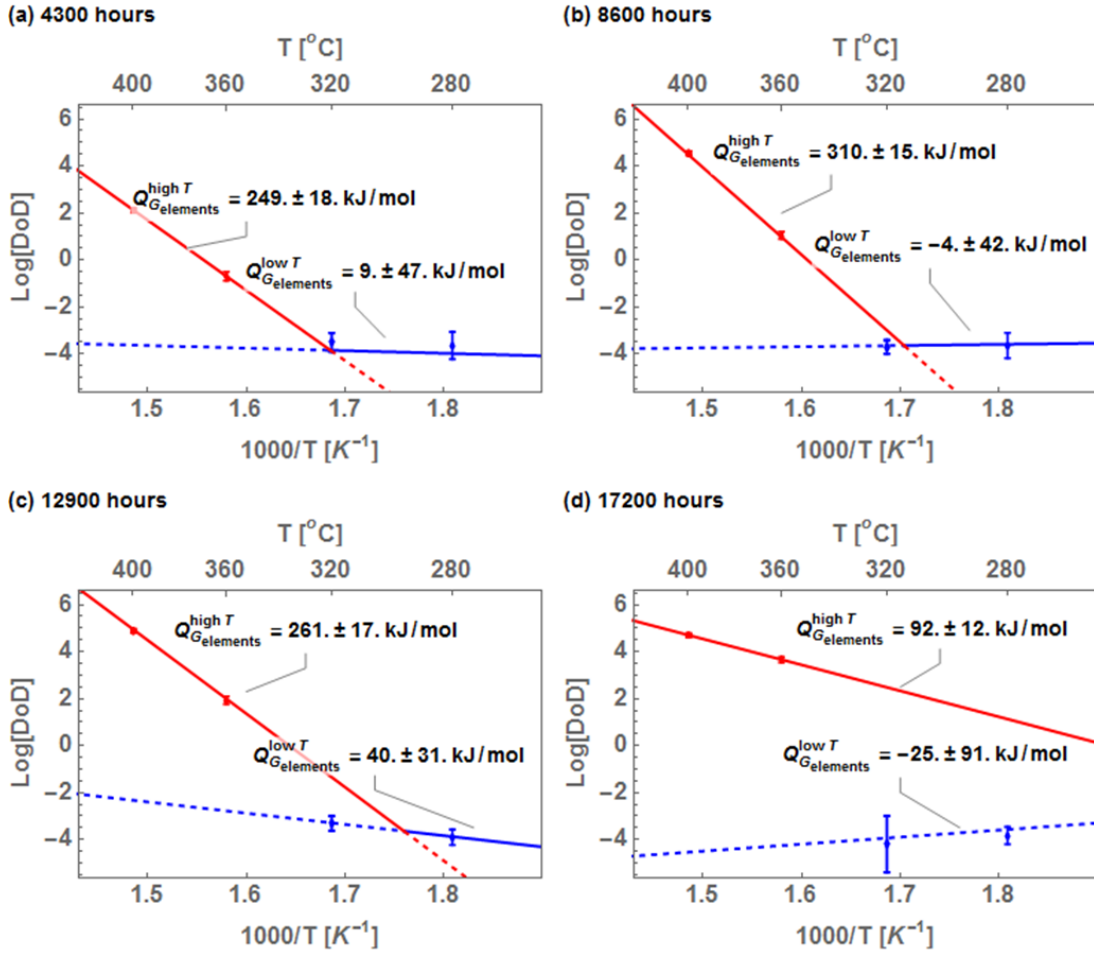


**Figure 56.** Activation energy of G-phase precipitation derived both amplitude and volume fraction components of D.o.D at low operational (blue) and high accelerated (red) temperatures at (a) 4300 h, (b) 8600 h, (c) 12900 h and (d) 17200 h.

The kinetics of spinodal decomposition and G-phase precipitation are linked. The activation values of both phase separation types are plotted side by side in Figure 57 for easier comparison. The G-phase precipitates form at the  $\alpha/\alpha'$  interface of spinodal decomposition domains, as shown in Figure 58. The average activation energy at accelerated temperatures for the  $\alpha'$ -domain was 134 kJ/mol at 4300 hours, 187 kJ/mol at 8600 hours, 197 kJ/mol at 12900 hours, and 208 kJ/mol at 17200 hours. The increasing Q values for spinodal decomposition infer that the diffusion mechanism of Cr atoms changes with time. At first, the Cr atoms are diffusing along

the dislocations and other defects usually present in all materials. With time, as the dislocations annihilate, the Cr atoms are diffusing within the Fe lattice. At 17200 hours, the calculated activation energy is within the range of the accepted activation energy for diffusion of Cr in the Fe lattice.

The average activation energy at accelerated temperatures for the G-phase forming zones was 249 kJ/mol at 4300 hours, 310 kJ/mol at 8600 hours, 261 kJ/mol at 12900 hours, and 92 kJ/mol at 17200 hours. As the G-phase is precipitating, the interfaces of the spinodal decomposition domains are still forming, and therefore G-phase elements are diffusing through bulk. As time progresses, the spinodal domains are becoming more distinct and therefore the activation energy of G-phase elements drops as the interdomain interfaces facilitate the diffusion. At 17200 hours, the spinodal domain interfaces are well-defined. The G-phase precipitates coarsen by diffusion through the grain boundaries. The activation energy at lower temperatures had large error values and did not noticeably vary as time progressed. At shorter times of high temperatures and long times of low temperatures, diffusion most likely occurs through dislocation mechanism.

The G-phase is observed to form at the  $\alpha/\alpha'$  interfaces as illustrated in Figure 16. The microstructure of ferrite near the ferrite/austenite interface after the phase separation at 400 °C for 17,200 h can be clearly seen by examining a thin slice of a reconstructed volume, with  $\alpha'$ -phase domains highlighted by Cr atoms (magenta) and G-phase precipitates highlighted by Ni atoms (green), as shown in Figure 58.

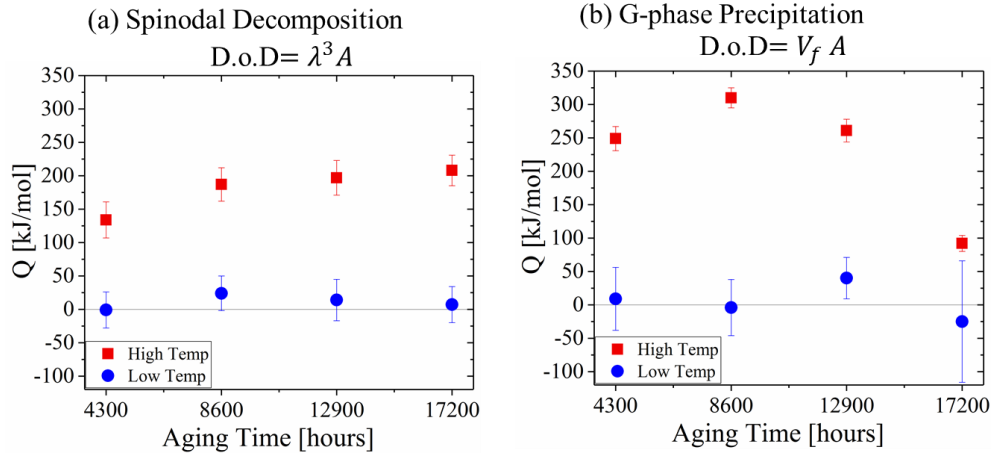


**Figure 57.** Activation energy plot of all values in (a) spinodal decomposition and (b) G-phase precipitation.

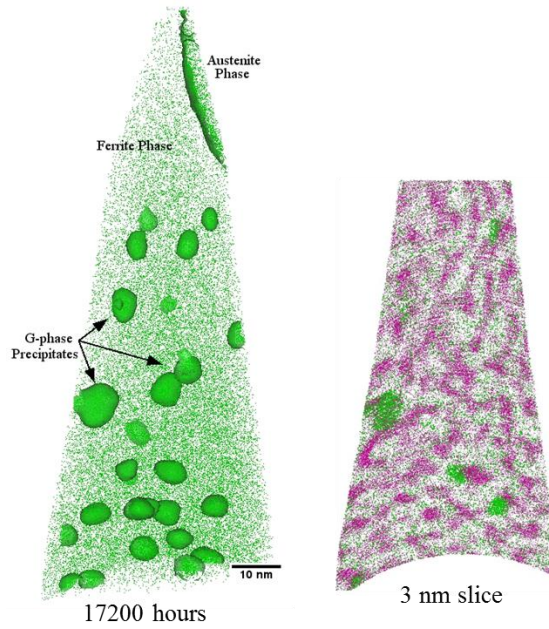


**Figure 58.** CF-3 samples aged for 17200 hours at 400 °C illustrating: (a) APT reconstruction displaying Ni atoms (green) and G-phase precipitates delineated by 6.5 at. % Ni isoncentration surfaces; (b) 3 nm slice of the same APT reconstruction displaying Cr (magenta) and Ni (green) atoms, indicating G-phase precipitates are located within the interface of spinodal decomposition domains (Fe atoms not shown for clarity).

### 6.5.3 Validity of Accelerated Temperatures

The use of accelerated temperatures above the transition is still valid for future prediction models because there are similar thermodynamics or phase transformations in the operational and accelerated temperatures. Even though the kinetics is different, the contribution of the each diffusion mechanism can be accounted for by the time factor within the diffusion distance equation. Prediction models can be formulated in the short term provided that no other phase transformations occur.

## 6.6 Predicting D.o.D

### 6.6.1 Spinodal Decomposition

The hyperbolic tangent (Tanh) function was used as a fitting function due to its appropriate shape to the increase of D.o.D. The Tanh function was not based on any scientific explanation. To predict D.o.D, it is necessary to define the range of temperatures in order to make an assumption that no other phase transformations will be precipitating or the steel will not melt. Outside of the given range, there are different thermodynamics taking place that will never be attained at lower temperatures. In addition, it is also necessary to define the diffusion mechanism that will occur in order to factor the time and temperatures to achieve the same diffusion distance. The Figure 59 fits the spinodal D.o.D to the Tanh function. At shorter times of accelerated temperatures, the diffusion mechanism through dislocations can be assumed because from Figure 53 (a), the diffusion mechanism of high temperatures at 4300 hours was suggested to be through dislocations.

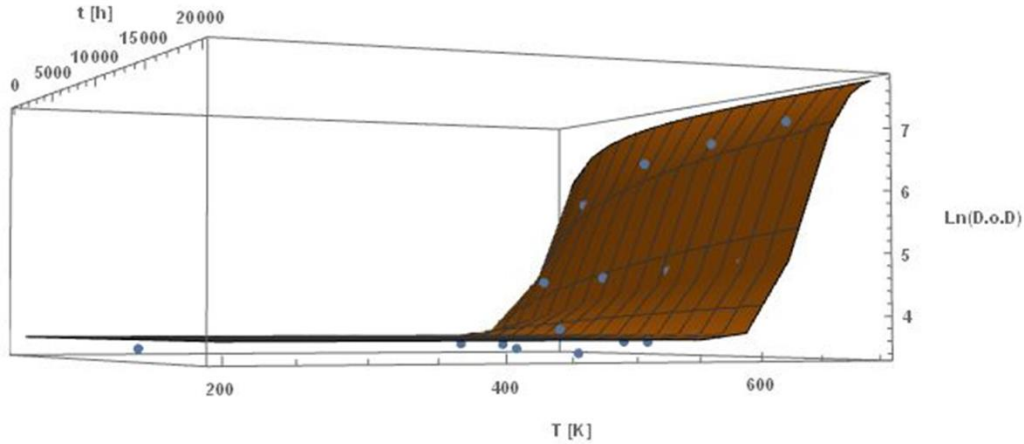


**Figure 59.** Hyperbolic tangent fitting of D.o.D at all unaged and aged samples of the CF-3 alloy.

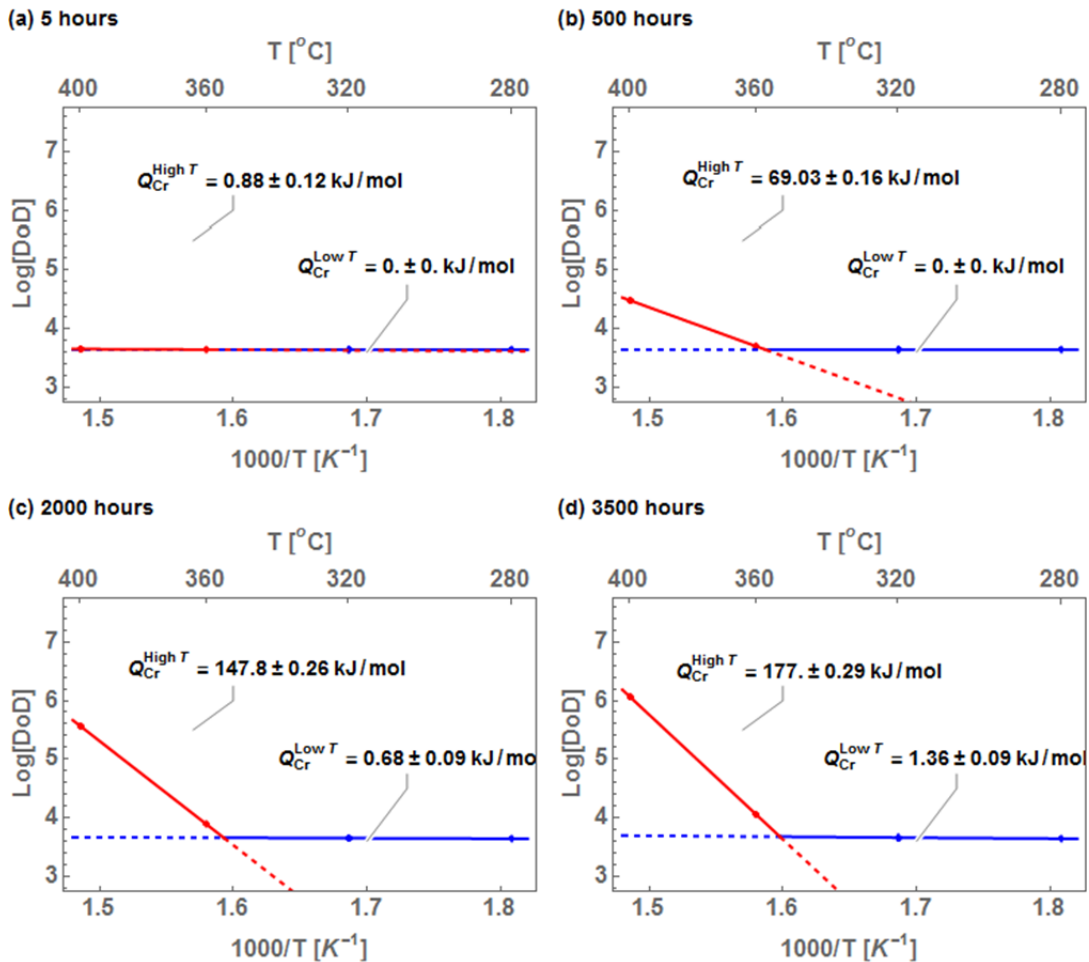


**Figure 60.** Activation energy of interpolated spinodal decomposition data that were derived from both amplitude and wavelength components of D.o.D at low operational (blue) and high accelerated (red) temperatures at (a) 5 h, (b) 500 h, (c) 2000 h and (d) 3500 h.

The Tanh function did not fit well at 280 °C at all times, as shown in Figure 59. However, the activation energies at high temperatures of the interpolated data at 5 h, 500 h, 2000 h, and 3500 h, as shown in Figure 60 were reasonable to suggest dislocation diffusion mechanism.

#### 6.6.2 G-phase Forming Zones

Pareige et al [3] studied thermal aging of CF-8M alloy up to 200,000 hours. From the results, in particular two laboratory-aged samples with the aging conditions 10,000 hours at 350 °C and 72,000 at 325 °C stand out. The spinodal decomposition wavelength and amplitude variation were similar. The G-phase precipitate radius and volume fraction of the 350 °C sample were slightly larger than the 325 °C sample, but the number density was similar for both samples. The microhardness of the ferrite phase was slightly higher for the 350 °C sample. Comparing Pareige's results to the CF-3 samples at two aging conditions 12,900 hours at 360 °C (C3) and 4,300 hours at 400 °C (A4), draws a distinction between the two alloys. There is miscibility gap in the Fe-Mo phase diagram, which may be accelerating spinodal decomposition in the CF-8M alloy more than the CF-3 alloy.

Assuming that the methodology of measuring the extent of phase separation is neutral in comparing two aging condition, the kinetics of spinodal decomposition, G-phase precipitation, and the corresponding mechanical properties are different in the two alloys. In the CF-3 alloy, the spinodal amplitude and wavelength, and therefore the spinodal D.o.D, are much higher in the A4 sample than the C3 sample and the quantities of the latter are higher than in samples aged at 320 °C. However, for G-phase precipitation, the radius is bigger for the A4 sample, but the number density is

larger for the C3 sample. The volume percentage is a balance between the radius and number density. Between the two samples, the volume percentage of G-phase precipitation for C3 is slightly larger. The G-phase forming elements composition is slightly higher for the A4 sample. Thus, the G-phase D.o.D, calculated by multiplying the volume percentage by the composition, is roughly equal for both A4 and C3 samples. The interaction between spinodal decomposition and G-phase precipitation can explain why the kinetics of spinodal decomposition is slower than that of G-phase in the C3 sample. There is a large number density of small G-phase forming zones at 360 °C compared to 400 °C. These large number of precipitates are pinning the spinodal decomposition domains, thus preventing the  $\alpha'$ -domain from growing. At 400 °C, as the G-phase precipitates were coarsening, they were losing their pinning effect on the spinodal domain, allowing them to grow simultaneously.

From these two samples, the kinetics of spinodal decomposition is much faster at higher temperatures, while the kinetics of G-phase precipitation is more complex because it involves the size, number density, and concentration. From D.o.D calculations, the G-phase kinetics of A4 and C3 are similar. The D.o.D represents the total volume of atoms that have diffused. Since A4 and C3 samples have the same diffusional distance, an Arrhenius relationship with an activation value of 112 kJ/mol, can predict similar diffusional distances at other times and temperatures—at 320 °C, it will take 64,000 hours (7.3 years) and at 280 °C, it will take 332,000 hours (37.8 years). Only the D.o.D is assumed to be similar. Factors of the D.o.D such as the radius, number density, and concentration of the G-phase precipitates at the lower

temperatures will be different and therefore the diffusion mechanism may also be different.

The mechanical properties of the two samples, C3 and A4, are also similar, based on their HV and CVN values, 185 HV500g and 100 Ft-Lbs, respectively. However, not enough data were collected to predict the material properties. There is a large variability with the data because of testing only 2 to 4 specimens per sample. Therefore, the HV and CVN data are only useful for showing trends to discuss the microstructural evolution but not to predict future values.

### 6.7 Influence of Carbide

#### 6.7.1 Spinodal Decomposition

The occurrence of the Cr SDZ in the ferrite phase of CF-8 steel near a carbide and not of CF-3 suggests that the Cr-rich carbides locally influence the phases' local composition. Additionally, the SDZ formation in the ferrite phase and not the austenite phase suggests that differences in Cr diffusivity in each phase also influence its formation. Since Cr is the predominant metallic element in the  $M_{23}C_6$  carbide [46], its nonstoichiometric composition in the unaged CF-8 suggests that Cr diffuses into the carbide during aging while Fe, Mo, Ni, Mn, and Si most likely diffuse out of the carbide, thereby permitting its composition to approach equilibrium. In addition, since the  $M_{23}C_6$  carbide is located at the heterophase interface, enhanced or short circuit diffusion of Cr from the ferrite phase into the carbide phase along the interface may occur. The diffusion of solute elements at grain boundaries and heterophase interfaces can be several orders of magnitude greater than in the bulk volume [95], [96], and the formation of the SDZ in the ferrite phase of the unaged CF-8 suggests

that the kinetics of diffusion are fastest at the heterophase interface. The influence of the  $M_{23}C_6$  carbide on the local Cr concentration at the heterophase interface and formation of an SDZ in the ferrite phase of CF-8 but not CF-3 is supported by APT observations where we measure a mean Cr concentration of 24.9 at. % for CF-8, Figure 26(b), and 28.7 at.% in the ferrite phase for CF-3, Figure 25(b). The mean Cr concentration is 22.3 at.% in the austenite phase of both steels. Hence, formation of the carbide locally depletes the Cr concentration in the ferrite phase of CF-8. A similar SDZ was observed at a grain boundary (GB) in a multicomponent Fe-Cu steel due to the presence of an  $Fe_3C$  carbide at the interface and was also attributed to more rapid kinetics [97].

There is a difference in diffusivity of Cr between the two phases. Williams and Faulkner studied Cr diffusion in ferritic and austenitic steels [98] and found that Cr in b.c.c. ferrite had a diffusion constant of  $D_o = 0.15 \left( \begin{smallmatrix} +0.54 \\ -0.12 \end{smallmatrix} \right) cm^2s^{-1}$  and activation energy of  $Q = 210(\pm 15) kJ mol^{-1}$ , whereas Cr in f.c.c. austenite had a diffusion constant of  $D_o = 0.27 \left( \begin{smallmatrix} +1.04 \\ -0.22 \end{smallmatrix} \right) cm^2s^{-1}$  and  $Q = 264(\pm 16) kJ mol^{-1}$ . The Arrhenius diffusion equation of Cr is  $\bar{D}_{Cr} = D_o e^{-Q/RT}$ , where R is the gas constant  $8.31 J (mol K)^{-1}$  and T is the absolute temperature. The diffusion distance during solution treatment can be determined to a first order approximation using the solution treatment temperature of 1338 K (1065 °C). The 3D root-mean-square (RMS) diffusion distance of Cr,  $\langle x_{Cr} \rangle = \sqrt{6 \times \bar{D}_{Cr} \times t}$ , is 64.1  $\mu m$  in ferrite, and 7.6  $\mu m$  in austenite where t is the solution treatment time of 7200 s. Thus, Cr has a diffusion distance in the ferrite phase an order of magnitude greater than in the austenite phase

for the same time interval indicating that the Cr diffusion kinetics are more rapid in ferrite thereby promoting the formation of a Cr SDZ at the interface.

In order to account for the measured differences in local mean Cr concentration in the b.c.c.  $\delta$ -ferrite phase on the Cr spinodal decomposition amplitudes between the CF-3 and CF-8 steels, a ratio of normalized spinodal decomposition amplitudes,  $A_j^*$ , was calculated for an element  $j$ ,  $A_j^* = |A_i^{CF-8}|/|A_i^{CF-3}| = \{(A_j^{CF-8} / \bar{C}_j^{CF-8})\}/\{A_j^{CF-3} / \bar{C}_j^{CF-3}\}$ . The mean concentrations used in the equation for the quantity  $A_j^*$  are from the proxigrams in Figure 25(b) and Figure 26(b) for CF-3 and CF-8, respectively. The quantity  $A_j^*$  for Cr is 1.15, which indicates the normalized Cr amplitude is greater in the CF-8 steel. A decrease of the local mean Cr concentration in the ferrite phase may affect the Cr atomic mobility due to the concentration dependence of the interdiffusion coefficient [99], [100] in the Cahn-Hilliard equations and thus lead to different spinodal decomposition amplitudes in the steels.

The small differences in nominal composition between the two steels suggest that incipient spinodal decomposition should be similar since the two steels would have a similar position in the miscibility gap of the phase diagram and hence the driving force for phase separation would be similar. The APT results demonstrate, however, that the normalized Cr amplitude in the unaged CF-8 steel is greater than in the CF-3 steel. This is possibly due to the presence of the Cr-rich  $M_{23}C_6$  carbide phase in CF-8 and not CF-3 that locally influences the Cr concentration in the ferrite phase by formation of the SDZ, as discussed above.

### 6.7.2 G-phase Forming Zones

At locations away from the carbides, there is a Ni SDZ in the ferrite phase caused by segregation of Ni to the interface. The ferrite phase in the vicinity of the carbide has a Cr SDZ. Since the carbide is depleted in Ni and Si, these elements did not have a SDZ in the ferrite phase. In fact, the ferrite phase next to the carbide is enriched in Ni and Si that were ejected from the carbide. The result is more nucleation and growth of G-phase in the ferrite phase directly adjacent to the carbide. TEM studies found that there was even G-phase precipitating at the ferrite/carbide interface of a 17200 h aged sample at 400 °C [87]. The G-phase precipitates in ferrite were viewed in TEM with kinematic bright-field and centered dark-field using G-phase diffraction spots. Because of the small G-phase precipitate volume fraction, the reflection of G-phase could not be identified readily at the major zone orientation of ferrite. However, strong G-phase reflections could be identified when the ferrite was tilted on a minor zone of ferrite, and could be used to produce the dark-field images of the G-phase precipitates.

The concentration of C affects the kinetics of G-phase formation as seen in Figure 61, where CF-3 alloys formed G-phase particles after aging for 4300 h at 360 °C and 400 °C while CF-8 alloys only formed them at 400 °C. The interaction of C with austenite stabilizers Ni and Mn in the ferrite phase may account for the high C alloys having less G-phase precipitation than the low C alloys [29, 30]. Comparing the kinetics of spinodal decomposition and G-phase precipitation in the CF-8 alloy near a carbide and far away from a carbide, Figure 62 shows that the spinodal decomposition amplitude is similar but the G-phase clustering is different. The

spinodal amplitude had comparable values, even if the Cr concentration of the  $\alpha$ -domain and  $\alpha'$ -domain for the near to carbide and far from carbide samples were different. In the near to carbide sample, the max and min Cr concentrations were  $33.2 \pm 0.3 \%$  and  $17.3 \pm 0.1 \%$ , respectively, and the calculated amplitude is  $15.9 \pm 0.3 \%$ . In the far from carbide sample, the max and min Cr concentrations were  $38.1 \pm 0.9 \%$  and  $22.9 \pm 0.3 \%$ , respectively, and the calculated amplitude is  $15.2 \pm 1.0 \%$ . In the near to carbide ferrite, the G-phase concentration of elements Ni, Si, Mn, Mo, Cu, and C, was  $26.8 \pm 3.5 \%$ , while that of far from carbide ferrite was  $10.5 \pm 1.3 \%$ . With a 6.5 at. % Ni isosurface, no G-phase precipitate was found in the ferrite far from carbide, while the G-phase forming zones in the ferrite near the carbide has a  $\langle R \rangle$  of  $1.22 \pm 0.05$  nm,  $N_v$  of  $5.23 \times 10^{23} \pm 3.76 \times 10^{22}$  ppts./m<sup>3</sup>, and  $V_p$  of  $0.57 \pm 0.00 \%$ . The complex interaction of the solute elements with each other is prominent, especially in the G-phase precipitation behavior near the phase boundary [30]. The degree of G-phase precipitation is mostly dependent on C composition.

The carbides influence the acceleration of phase separation because the Cr-rich, Ni-Si-poor carbides deplete the neighboring ferrite phase of Cr and eject Ni and Si into it. The ratios of Cr amplitude to the ferrite Cr concentration were equal in both alloys. This indicates that the normalized increase in amplitude were similar in the samples regardless of the variation in chemical composition. In agreement with literature, the ferrite phase in the CF-8 alloy near the carbides had more G-phase forming zones than the ferrite phase in the CF-8 alloy away from the carbides. The

size and number density of the G-phase forming zones in the ferrite phase of the CF-3 alloy was between that of the CF-8 alloy near and far from carbide.

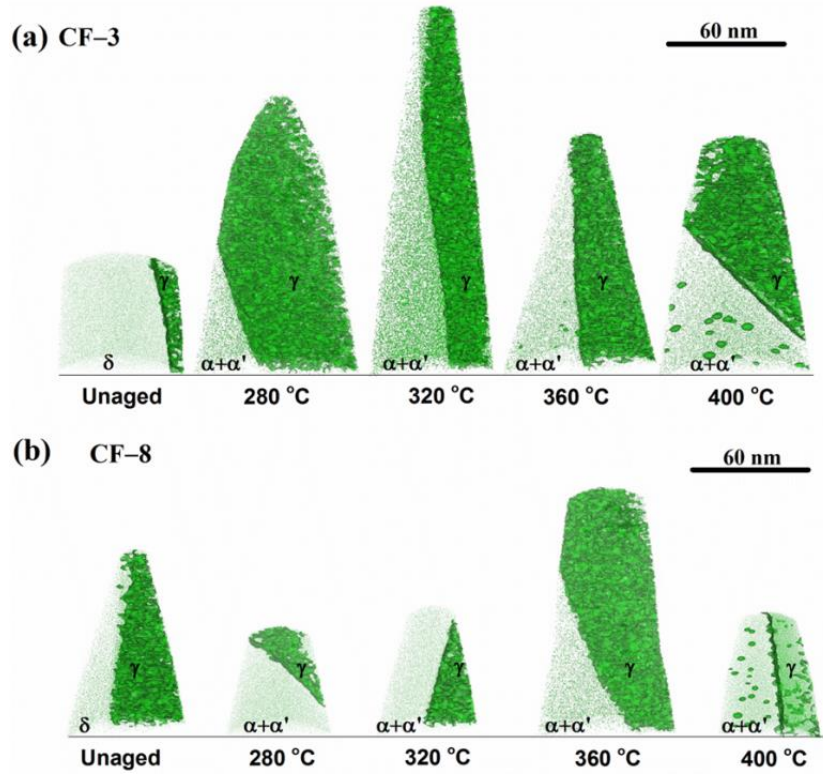


**Figure 61.** G-phase forming zones as delineated by 6.5 at. % Ni in unaged and all 4300 hours aged steels for both (a) CF-3 and (b) CF-8 alloys.

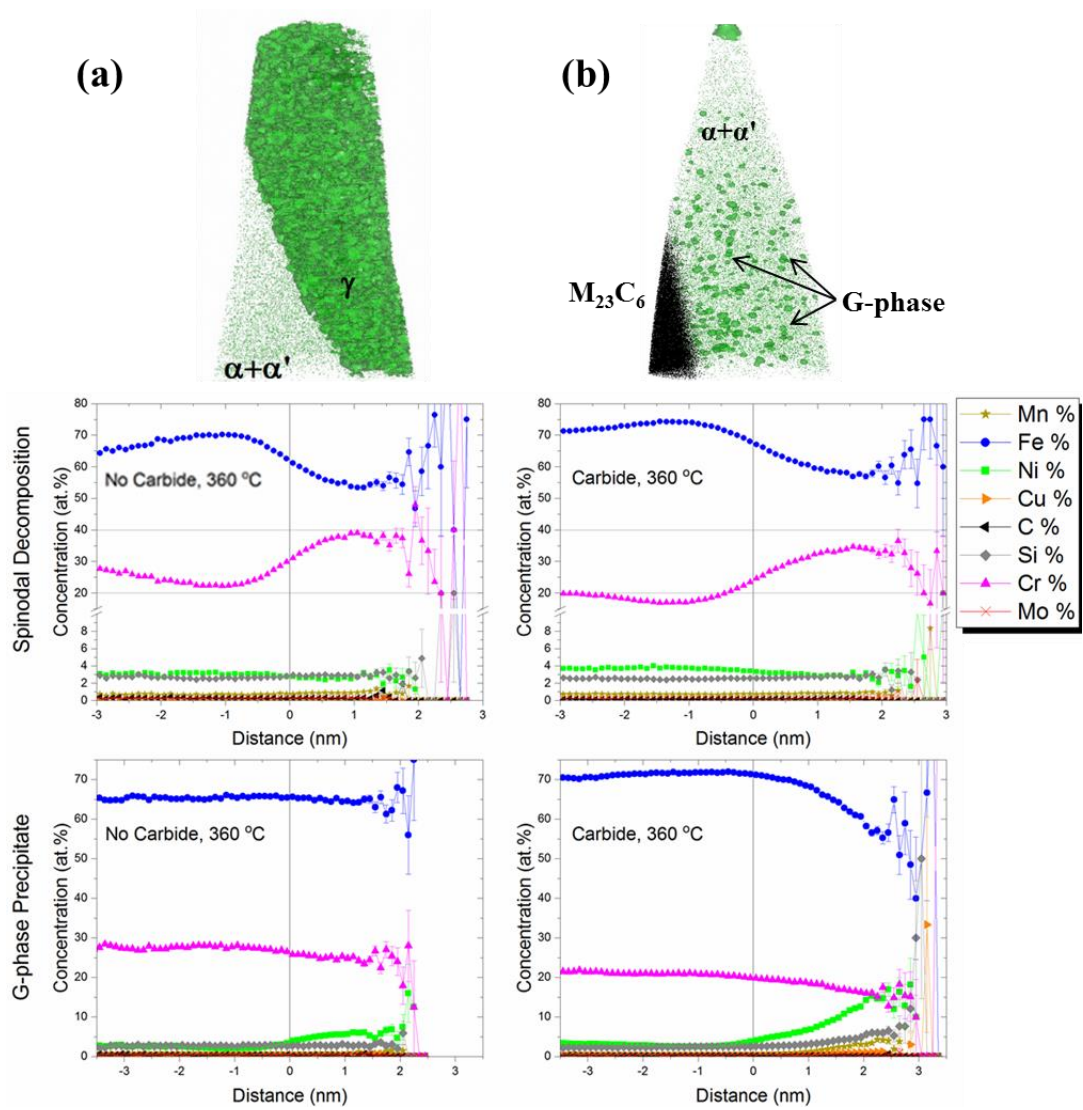


**Figure 62.** Comparing the effect of distance from carbide on spinodal decomposition and G-phase precipitation on the ferrite phase of two CF-8 samples both aged for 4300 hours at 360 °C: (a) far from carbide, (b) near carbide

## Chapter 7: Conclusions

The model cast alloys of grades CF-3 and CF-8 were selected to represent the vast majority of CDSS alloys used in LWR power plants. The alloys were aged at 280 °C, 320 °C, 360 °C, and 400 °C for 4300 h, 8600 h, 12900 h, and 17200 h. The mechanical and microstructural characterization data obtained for the unaged and aged samples were presented in this report. Vickers Microhardness and Charpy impact tests comprise the key datasets used to discuss the effects of thermal aging embrittlement. The analytical tools available from atom probe tomography (APT) were successfully employed in this investigation to characterize the morphology and extent of phase separation. The results and discussion focused on the kinetics of thermal aging degradation and possible influential factors. The outcomes are summarized below.

1. In this study, the volume fraction calculation of the ferrite content was about 12 vol.% in the CF-3 alloy and 10 vol.% in the CF-8 alloy. This was attributed to the initial composition. The ferrite phase decomposes during thermal aging and therefore higher ferrite content will result in drastic changes in mechanical properties.
2. Both alloys in this study experienced a ductile to brittle transition in the fracture mode. The Vickers microhardness increased as the Charpy impact toughness decreased as a function of aging time and temperature. At low temperatures, the phase separation kinetics is slow; therefore, the effects of the carbide dominate. At higher temperatures, the kinetics of phase separation is fast; therefore the effects of phase separation dominate. These results agree

with literature that there is a positive correlation between hardness and spinodal decomposition.

3. There is disagreement in literature about the nature of reaction in the ferrite phase near the carbide. In this study, the Cr-rich, Ni-Si-poor  $M_{23}C_6$  carbides found only at the ferrite/austenite interface of the CF-8 alloy depleted the Cr from the ferrite phase and ejected Ni and Si into it. The high Ni concentration in the ferrite phase precipitated into G-phase precipitates rather than a new austenite phase. The APT results illustrated large G-phase precipitates in the vicinity of the carbide that were confirmed by TEM studies.
4. A new method was developed in this study to measure the wavelength and amplitude values simultaneously in the unaged and aged samples. The values were comparable to accepted traditional methods, such as Auto-correlation Function (ACF) and Larson-Bar-on-Miller (LBM) that separately measured the wavelength and amplitude, respectively. This study found incipient phase separation in the unaged samples of both alloys. In concurrence with literature, the distribution of the Cr elements had a slight deviation from a random distribution in the as-received condition.
5. There is a difference of opinion in literature on whether the G-phase precipitates have an effect on the mechanical properties because the change in mechanical properties saturates due to spinodal decomposition before the G-phase precipitates were detected. Based on this study, it is believed that the G-phase precipitates influence the mechanical properties because the lattice mismatch between the f.c.c G-phase precipitates and b.c.c spinodal

decomposition domains contributes to the strain hardening. The increase in strength and hardness and concomitant decrease in impact toughness is greater in both CF-3 and CF-8 alloys than Fe-Cr-Ni alloys, which undergo spinodal decomposition but do not form the Ni-silicide G-phase precipitate due to lack of Si.

6. In this study, the G-phase forming zones were delineated by a 6.5 at. % Ni isoconcentration surface, which is a concentration beyond the random Ni fluctuation in the ferrite phase. The surfaces were used to quantify the radius, number density, and volume fraction. The G-phase forming zones were found only in the ferrite phases of the steels aged at accelerated temperatures at all aging times. The radii of the G-phase forming zones were larger at 400 °C and the number densities were higher at 360 °C. The volume fraction calculation had competing factors from both the radius and number density. There is a progression of G-phase elemental segregation at lower temperatures resulting in zones of increasing Ni concentration; however, the Ni concentration did not reach the 6.5 at.% threshold within two years. Nevertheless, the trend suggests that the G-phase will form beyond 2 years at low temperatures.
7. In this work, a new method to measure total diffusion was developed to account for the concomitant increase in size and concentration of spinodal decomposition and G-phase precipitation during thermal aging. Past literature studied the kinetics of the increase in wavelength and amplitude separately and therefore did not capture the total diffusion. They also used time

exponents based on the LSW theory, which does not apply to such complex systems. In a method termed the Degree of Decomposition (D.o.D), the volume of the  $\alpha'$ -phase was multiplied by the amplitude,  $\lambda^3 A$ . For the G-phase forming zones, the D.o.D was calculated by multiplying the volume fraction by the amplitude,  $V_f A$ , because the number density of G-phase is increasing unlike the constant volume fraction in spinodal decomposition.

8. In this study, the activation energy of diffusion was calculated from the slope in the plot of the natural log of D.o.D versus inverse temperature. The activation energy values changed with time, indicating that the rate-limiting diffusion mechanism changes with time. As expected, the contribution of diffusion through dislocations, grain boundaries, and the lattice varied by temperature. However, the use of accelerated temperatures, above the temperature where the diffusion mechanism transitions, is still valid for future prediction models because there are similar thermodynamics or phase transformations in the operational and accelerated temperatures used in this study. Even though the kinetics is different, the contribution of the each diffusion mechanism can still be accounted for by the time factor within the diffusion distance equation. Prediction models can be formulated in the short term provided that no other phase transformations occur.
9. The kinetics of spinodal decomposition and G-phase precipitation are linked. G-phase precipitates form at the  $\alpha/\alpha'$  interface of spinodal decomposition domains. The increasing Q values for spinodal decomposition calculated in this study infer that the diffusion mechanism of Cr atoms changes with time.

At first, the Cr atoms are diffusing along the dislocations and other defects usually present in all materials. With time, as the dislocations annihilate, the Cr atoms are diffusing within the Fe lattice. At 17200 hours, the calculated activation energy value of 208 kJ/mol is within the range of the accepted activation energy for diffusion of Cr in the Fe lattice. As the G-phase is precipitating, the interfaces of the spinodal decomposition domains have not yet fully formed. Therefore, the G-phase forming elements start by diffusing through bulk. As time progresses, the spinodal domains are becoming more distinct and therefore the activation energy of G-phase elements decreases because the interdomain interfaces facilitate the diffusion. The G-phase precipitates start coarsening by diffusing through the spinodal grain boundaries. The activation energy at lower temperatures had large error values and did not noticeably vary as time progressed. At shorter times of high temperatures and long times of low temperatures, diffusion most likely occurs through dislocation mechanism.

## Chapter 8: Suggestions for future work

There are several challenges that need to be addressed in studying the thermal embrittlement of CDSS at low temperatures.

1. There is an urgent need for the improvement of thermodynamics and kinetics databases in the ternary and multi-component systems.
2. For data acquisition, the primary focus of this thesis was on the ferrite phase near the heterophase interface. Most literature studies do not state the precise location of the extracted ferrite phase sample, and is therefore assumed to be at the center of the phase. Due to the differences in kinetics based on the local chemical variation and proximity to high diffusion paths at the phase boundary, a careful study of correlating the distance to the interface will be useful for proper comparisons. There is a depletion of solute atoms due to segregation to the boundary. Therefore, other than in the case of carbide at the heterophase interface, the G-phase precipitates are generally bigger and more abundant towards the interior of the ferrite phase. This correlation study will be helpful in determining where a fracture initiates and propagates.
3. An experimental suggestion for analyzing sufficient data in APT is employing laser pulsing. Voltage pulsing applies high stresses on the tip, leading to premature fractures. Laser pulsing would ensure longer acquisitions, especially at heterophase interfaces and large precipitates, where there is an abrupt change in evaporation fields.
4. Another experimental proposal is to carry out thermal aging at shorter times for samples at higher temperatures. As discussed above in the prediction of spinodal

decomposition D.o.D, the negative extrapolations presumed that the D.o.D for 1 month at 360 °C was similar to 2 years at 320 °C and 1 month at 400 °C was similar to 6 months at 360 °C. Running experiments of higher temperatures at shorter times will be the first step in attempting to validate a positive extrapolation in the future.

5. As a follow up of (#4), choosing the times and temperatures should be decided scientifically. In this dissertation, the four times in six month increments and four temperatures with forty degrees differences were chosen for convenience of reporting. If the aging times and temperature were chosen in a scientific way, employing the diffusion distance equation, the microstructural evolution quantification and mechanical property values would provide deeper insight into the thermal aging phenomena.
6. Perform radiation and stress studies to determine their interactions with thermal effects. Currently, decommissioned samples cannot be compared to those aged in this work because the former also experience thermal and fatigue effects that are not present in the lab setting.

## Appendices

### Code for In-lab method

```
' Find regional alternating maxima for each set of data above the
weighted mean+err
Public Sub inLab()
    ' Variables with a 1 at the end are for the first data set (Fe),
    2 for the second (Cr)
    Dim R As Long ' row to read data
    Dim OutR1 As Long, OutR2 As Long, outRow As Long ' output row
    Dim MaxRow1 As Long, MaxRow2 As Long
    Dim SeriesFlag As Integer ' which series are we checking now? =1
    or 2

    Range(Cells(2, "AX"), Cells(ActiveSheet.UsedRange.Rows.Count,
"BE")).ClearContents

    R = 2 ' starting row

    outRow = 2

    Do Until Cells(R, "AP") = ""

        MaxRow1 = NextMaximumRow(R:=R, DataCol:=Range("AR1").Column,
WMean:=Range("AT2"), WSErr:=Range("AU2"))

        If MaxRow1 > 0 Then

            Cells(outRow, Range("AX1").Column) = Cells(MaxRow1, "AP") ' x
            Cells(outRow, Range("AY1").Column) = Cells(MaxRow1,
Range("AR1").Column) ' y

            Cells(outRow, Range("AZ1").Column) = Cells(MaxRow1, "AP") ' x
            Cells(outRow, Range("BA1").Column) = 0 ' y

            R = R + 1

            outRow = outRow + 1
        End If

        If MaxRow1 = 0 Then
            R = R + 1
        End If

        R = R + 1

    Loop

    R = 2

    Do Until Cells(R, "AP") = ""

        MaxRow2 = NextMaximumRow(R:=R, DataCol:=Range("AS1").Column,
WMean:=Range("AV2"), WSErr:=Range("AW2"))
```

```

If MaxRow2 > 0 Then

    Cells(outRow, Range("AZ1").Column) = Cells(MaxRow2, "AP") ' x
    Cells(outRow, Range("BA1").Column) = Cells(MaxRow2,
Range("AS1").Column) ' y
    Cells(outRow, Range("AX1").Column) = Cells(MaxRow2, "AP") ' x
    Cells(outRow, Range("AY1").Column) = 0 ' y

    R = R + 1

    outRow = outRow + 1
End If

If MaxRow2 = 0 Then
R = R + 1
End If

R = R + 1

Loop

Call Range("AX:BA").Sort(Key1:=Range("AX1"), Order1:=xlAscending,
Header:=xlYes)

R = 2
OutR1 = 2
OutR2 = 2

Dim PeakRow1 As Long, PeakRow2 As Long

' Which series has the first Peak?

' Get first maximum for Fe
PeakRow1 = NextPeakRow(R:=2, DataCol:=Range("AY1").Column)
' Get first maximum for Cr
PeakRow2 = NextPeakRow(R:=2, DataCol:=Range("BA1").Column)

If PeakRow1 < PeakRow2 And PeakRow1 > 0 Then
    Cells(OutR1, Range("BB1").Column) = Cells(PeakRow1, "AX") ' x
    Cells(OutR1, Range("BC1").Column) = Cells(PeakRow1,
Range("AY1").Column) ' y
    OutR1 = OutR1 + 1
    SeriesFlag = 2 ' next series to check
    R = PeakRow1

ElseIf PeakRow2 > 0 Then
    Cells(OutR2, Range("BD1").Column) = Cells(PeakRow2, "AX") ' x
    Cells(OutR2, Range("BE1").Column) = Cells(PeakRow2,
Range("BA1").Column) ' y
    OutR2 = OutR2 + 1
    SeriesFlag = 1 ' next series to check
    R = PeakRow2

ElseIf PeakRow2 = 0 Then
SeriesFlag = 1
R = PeakRow2 + 1

```

```

ElseIf PeakRow1 = 0 Then
SeriesFlag = 2
R = PeakRow1 + 1

Else
MsgBox "There is no Peak"
Exit Sub
End If

R = R + 1

Do Until Cells(R, "AP") = ""

Select Case SeriesFlag

Case 1
' Get next maximum for Fe
PeakRow1 = NextPeakRow(R:=R,
DataCol:=Range("AY1").Column)
If PeakRow1 > 0 Then
Cells(OutR1, Range("BB1").Column) = Cells(PeakRow1, "AX") ' x
Cells(OutR1, Range("BC1").Column) = Cells(PeakRow1,
Range("AY1").Column) ' y
OutR1 = OutR1 + 1
SeriesFlag = 2 ' next series to check
R = PeakRow1

End If

Case 2
' Get next maximum for Cr
PeakRow2 = NextPeakRow(R:=R,
DataCol:=Range("BA1").Column)
If PeakRow2 > 0 Then
Cells(OutR2, Range("BD1").Column) = Cells(PeakRow2, "AX") ' x
Cells(OutR2, Range("BE1").Column) = Cells(PeakRow2,
Range("BA1").Column) ' y
OutR2 = OutR2 + 1
SeriesFlag = 1 ' next series to check
R = PeakRow2
End If

Case Else
Stop

End Select

R = R + 1

Loop
End Sub

Private Function NextMaximumRow(R As Long, DataCol As Long, WMean As
Double, WSErr As Double) As Long

Dim MaxX As Double

```

```

Dim MaxY As Double

NextMaximumRow = 0
' Find next set of data above the mean. Upgrades R even when
we are at region of negative fluctuation.
Do While Cells(R, DataCol) <= WMean And Cells(R, "AP") <> ""
    R = R + 1
Loop
' loop through dataset above the mean
' get the maximum in this region of positive fluctuation
MaxX = 0
MaxY = WMean + WSErr
Do While Cells(R, DataCol) > WMean And Cells(R, "AP") <> ""
    If Cells(R, DataCol) > MaxY Then
        ' Update max
        NextMaximumRow = R
        MaxX = Cells(R, "AP")
        MaxY = Cells(R, DataCol)
    End If
    R = R + 1
Loop
End Function

```

```

Private Function NextPeakRow(R As Long, DataCol As Long) As Long

```

```

    Dim MaxPeak As Double
    Dim MaxX As Double
    Dim MaxY As Double

    NextPeakRow = 0
    ' Find next set of data above the mean. Upgrades R even when
    we are at region of negative fluctuation.
    Do While Cells(R, DataCol) = 0 And Cells(R, "AX") <> ""
        R = R + 1
    Loop
    ' loop through dataset above the mean
    ' get the maximum in this region of positive fluctuation
    MaxX = 0
    MaxY = 0
    Do While Cells(R, DataCol) > 0 And Cells(R, "AX") <> ""
        If Cells(R, DataCol) > MaxY Then
            ' Update max
            NextPeakRow = R
            MaxX = Cells(R, "AX")
            MaxY = Cells(R, DataCol)
        End If
        R = R + 1
    Loop
End Function

```

## Bibliography

- [1] J. K. L. Lai, C. H. Shek, and K. H. Lo, *Stainless Steels: An Introduction and Their Recent Developments*. Bentham Science Publishers, 2012.
- [2] O. K. Chopra, *Initial assessment of the mechanisms and significance of low-temperature embrittlement of cast stainless steels in LWR systems*. Division of Engineering, Office of Nuclear Regulatory Research, U.S. Nuclear Regulatory Commission, 1990.
- [3] C. Pareige, S. Novy, S. SAILLET, and P. Pareige, “Study of phase transformation and mechanical properties evolution of duplex stainless steels after long term thermal ageing (>20 years),” *Journal of Nuclear Materials*, vol. 411, no. 1–3, pp. 90–96, Apr. 2011.
- [4] F. Danoix and P. Auger, “Atom Probe Studies of the Fe–Cr System and Stainless Steels Aged at Intermediate Temperature: A Review,” *Materials Characterization*, vol. 44, no. 1–2, pp. 177–201, Jan. 2000.
- [5] T. Hamaoka, A. Nomoto, K. Nishida, K. Dohi, and N. Soneda, “Effects of aging temperature on G-phase precipitation and ferrite-phase decomposition in duplex stainless steel,” *Philosophical Magazine*, vol. 92, no. 34, pp. 4354–4375, Dec. 2012.
- [6] E.-Y. Guo, H.-X. Xie, S. S. Singh, A. Kirubanandham, T. Jing, and N. Chawla, “Mechanical characterization of microconstituents in a cast duplex stainless steel by micropillar compression,” *Materials Science and Engineering: A*, vol. 598, pp. 98–105, Mar. 2014.
- [7] S. Bonnet, J. Bourgoïn, J. Champredonde, D. Guttman, and M. Guttman, “Relationship between evolution of mechanical properties of various cast duplex stainless steels and metallurgical and aging parameters: outline of current EDF programmes,” *Materials Science and Technology*, vol. 6, no. 3, pp. 221–229, Mar. 1990.
- [8] F. Danoix, P. Auger, and D. Blavette, “Hardening of Aged Duplex Stainless Steels by Spinodal Decomposition,” *Microscopy and Microanalysis*, vol. null, no. 03, pp. 349–354, Jun. 2004.
- [9] Z.-X. Wang, F. Xue, W.-H. Guo, H.-J. Shi, G.-D. Zhang, and G. Shu, “Investigation of thermal aging damage mechanism of the Cast Duplex Stainless Steel,” *Nuclear Engineering and Design*, vol. 240, no. 10, pp. 2538–2543, Oct. 2010.
- [10] H. C. Wu *et al.*, “Effect of thermal aging on corrosion fatigue of Z3CN20.09M duplex stainless steel in high temperature water,” *Materials Science and Engineering: A*, vol. 655, pp. 183–192, Feb. 2016.
- [11] C. Capdevila, M. K. Miller, I. Toda, and J. Chao, “Influence of the  $\alpha$ - $\alpha'$  phase separation on the tensile properties of Fe-base ODS PM 2000 alloy,” *Materials Science and Engineering: A*, vol. 527, no. 29–30, pp. 7931–7938, Nov. 2010.
- [12] P. McConnell, W. Sheckherd, and D. Norris, “Properties of thermally embrittled cast duplex stainless steel,” *Journal of Materials Engineering*, vol. 11, no. 3, pp. 227–236, Dec. 1989.

- [13] P. Hedström, F. Huyan, J. Zhou, S. Wessman, M. Thuvander, and J. Odqvist, "The 475 °C embrittlement in Fe–20Cr and Fe–20Cr–X (X=Ni, Cu, Mn) alloys studied by mechanical testing and atom probe tomography," *Materials Science and Engineering: A*, vol. 574, pp. 123–129, Jul. 2013.
- [14] P. H. Pumphrey and K. N. Akhurst, "Aging kinetics of CF3 cast stainless steel in temperature range 300–400°C," *Materials Science and Technology*, vol. 6, no. 3, pp. 211–220, Mar. 1990.
- [15] S. L. Li *et al.*, "Microstructure evolution and impact fracture behaviors of Z3CN20-09M stainless steels after long-term thermal aging," *Journal of Nuclear Materials*, vol. 433, no. 1–3, pp. 41–49, Feb. 2013.
- [16] Y. H. Yao, J. F. Wei, and Z. P. Wang, "Effect of long-term thermal aging on the mechanical properties of casting duplex stainless steels," *Materials Science and Engineering: A*, vol. 551, pp. 116–121, Aug. 2012.
- [17] J. E. Brown, A. Cerezo, T. J. Godfrey, M. G. Hetherington, and G. D. W. Smith, "Quantitative atom probe analysis of spinodal reaction in ferrite phase of duplex stainless steel," *Materials Science and Technology*, vol. 6, no. 3, pp. 293–300, Mar. 1990.
- [18] T. S. Byun, Y. Yang, N. R. Overman, and J. T. Busby, "Thermal Aging Phenomena in Cast Duplex Stainless Steels," *Journal of the Minerals, Metals, and Materials Society*, vol. 68, no. 2, pp. 507–516, Nov. 2015.
- [19] F. G. Wasserman, S. S. M. Tavares, J. M. Pardal, F. B. Mainier, R. A. Faria, and C. dos S. Nunes, "Effects of low temperature aging on the mechanical properties and corrosion resistance of duplex and lean duplex stainless steels UNS S32205 and UNS S32304," *Rem: Revista Escola de Minas*, vol. 66, no. 2, pp. 193–200, Jun. 2013.
- [20] X. Lü, S. Li, H. Zhang, Y. Wang, and X. Wang, "Effect of thermal aging on the fatigue crack growth behavior of cast duplex stainless steels," *Int J Miner Metall Mater*, vol. 22, no. 11, pp. 1163–1170, Nov. 2015.
- [21] P. Auger, F. Danoix, A. Menand, S. Bonnet, J. Bourgoin, and M. Guttmann, "Atom probe and transmission electron microscopy study of aging of cast duplex stainless steels," *Materials Science and Technology*, vol. 6, no. 3, pp. 301–313, Mar. 1990.
- [22] N. Meyer, M. Mantel, A. Gauthier, and C. Bourgin, "Long term aging of various duplex stainless steels between 250 °C and 400 °C – relationship between toughness measurements and metallurgical parameters," *Rev. Metall.*, vol. 108, no. 4, pp. 213–223, 2011.
- [23] M. D. Mathew, L. M. Lietzan, K. L. Murty, and V. N. Shah, "Low temperature aging embrittlement of CF-8 stainless steel," *Materials Science and Engineering: A*, vol. 269, no. 1–2, pp. 186–196, Aug. 1999.
- [24] H. M. Chung, "Aging and life prediction of cast duplex stainless steel components," *International Journal of Pressure Vessels and Piping*, vol. 50, no. 1, pp. 179–213, Jan. 1992.
- [25] A. Trautwein and W. Gysel, "Influence of Long-Time Aging of CF8 and CF8M Cast Steel at Temperatures Between 300 and 500°C on Impact Toughness and Structural Properties," in *Stainless Steel Castings*, A. Melilli, Ed. 100 Barr

- Harbor Drive, PO Box C700, West Conshohocken, PA 19428-2959: ASTM International, 1982, pp. 165-165–25.
- [26] J. Simeg Veternikova *et al.*, “Thermal stability study for candidate stainless steels of GEN IV reactors,” *Applied Surface Science*, vol. 387, no. Supplement C, pp. 965–970, Nov. 2016.
- [27] T. Allen, J. Busby, M. Meyer, and D. Petti, “Materials challenges for nuclear systems,” *Materials Today*, vol. 13, no. 12, pp. 14–23, Dec. 2010.
- [28] “NRC: Effect of Thermal Aging and Neutron Irradiation on Crack Growth Rate and Fracture Toughness of Cast Stainless Steels and Austenitic Stainless Steel Welds (NUREG/CR-7185).” [Online]. Available: <https://www.nrc.gov/reading-rm/doc-collections/nuregs/contract/cr7185/>. [Accessed: 27-Nov-2017].
- [29] M. L. Grossbeck, *Effects of Radiation on Materials*. ASTM International, 2004.
- [30] G. S. Was *et al.*, “Assessment of radiation-induced segregation mechanisms in austenitic and ferritic–martensitic alloys,” *Journal of Nuclear Materials*, vol. 411, no. 1, pp. 41–50, Apr. 2011.
- [31] K. Fujii and K. Fukuya, “Effects of radiation on spinodal decomposition of ferrite in duplex stainless steel,” *Journal of Nuclear Materials*, vol. 440, no. 1, pp. 612–616, Sep. 2013.
- [32] J. Y. Xie, N. X. Chen, L. D. Teng, and S. Seetharaman, “Atomistic study on the site preference and thermodynamic properties for Cr<sub>23</sub>–xFexC<sub>6</sub>,” *Acta Materialia*, vol. 53, no. 20, pp. 5305–5312, Dec. 2005.
- [33] W. Xiong, M. Selleby, Q. Chen, J. Odqvist, and Y. Du, “Phase Equilibria and Thermodynamic Properties in the Fe-Cr System,” *Critical Reviews in Solid State and Materials Sciences*, vol. 35, no. 2, pp. 125–152, May 2010.
- [34] “Phase Transformations in Metals and Alloys: David A. Porter, K. E. Easterling: 9780412450303: Amazon.com: Books.” [Online]. Available: <https://www.amazon.com/Phase-Transformations-Metals-Alloys-Porter/dp/0412450305>. [Accessed: 23-Aug-2016].
- [35] R. Silva, L. F. S. Baroni, C. L. Kugelmeier, M. B. R. Silva, S. E. Kuri, and C. A. D. Rovere, “Thermal aging at 475°C of newly developed lean duplex stainless steel 2404: Mechanical properties and corrosion behavior,” *Corrosion Science*, vol. 116, no. Supplement C, pp. 66–73, Feb. 2017.
- [36] Y. Q. Wang, J. Han, H. C. Wu, B. Yang, and X. T. Wang, “Effect of sigma phase precipitation on the mechanical and wear properties of Z3CN20.09M cast duplex stainless steel,” *Nuclear Engineering and Design*, vol. 259, no. Supplement C, pp. 1–7, Jun. 2013.
- [37] S. K. Ghosh and S. Mondal, “High temperature ageing behaviour of a duplex stainless steel,” *Materials Characterization*, vol. 59, no. 12, pp. 1776–1783, Dec. 2008.
- [38] J. D. Tucker, M. K. Miller, and G. A. Young, “Assessment of thermal embrittlement in duplex stainless steels 2003 and 2205 for nuclear power applications,” *Acta Materialia*, vol. 87, pp. 15–24, Apr. 2015.
- [39] W. F. Gale and T. C. Totemeier, Eds., “13 - Diffusion in metals,” in *Smithells Metals Reference Book (Eighth Edition)*, Oxford: Butterworth-Heinemann, 2004, pp. 13–1.

- [40] C. Pareige, J. Emo, S. SAILLET, C. Domain, and P. Pareige, “Kinetics of G-phase precipitation and spinodal decomposition in very long aged ferrite of a Mo-free duplex stainless steel,” *Journal of Nuclear Materials*, vol. 465, pp. 383–389, Oct. 2015.
- [41] J. Emo, C. Pareige, S. SAILLET, C. Domain, and P. Pareige, “Kinetics of secondary phase precipitation during spinodal decomposition in duplex stainless steels: A kinetic Monte Carlo model – Comparison with atom probe tomography experiments,” *Journal of Nuclear Materials*, vol. 451, no. 1–3, pp. 361–365, Aug. 2014.
- [42] J. P. Massoud, P. Auger, F. Danoix, R. Rezakhanlou, and J. C. Van Duysen, “Evaluation of the thermal ageing of duplex stainless steels,” Electricite de France (EDF), EDF--93-NB-00113, 1993.
- [43] “Iron-Molybdenum (Fe-Mo) Phase Diagram.” [Online]. Available: <http://www.calphad.com/iron-molybdenum.html>. [Accessed: 27-Nov-2017].
- [44] F. C. Campbell, *Elements of Metallurgy and Engineering Alloys*. ASM International, 2008.
- [45] “Developments in fusion welding of stainless steels (January 1994).” [Online]. Available: <http://www.twi-global.com/technical-knowledge/published-papers/developments-in-fusion-welding-of-stainless-steels-january-1994/>. [Accessed: 27-Nov-2017].
- [46] T. S. Byun, Y. Yang, N. R. Overman, and J. T. Busby, “Thermal Aging Phenomena in Cast Duplex Stainless Steels,” *Journal of the Minerals, Metals, and Materials Society*, vol. 68, no. 2, pp. 507–516, Feb. 2016.
- [47] “A new constitution diagram for predicting ferrite content of stainless steel weld metals,” *Materials & Design*, vol. 14, no. 6, pp. 345–348, Jan. 1993.
- [48] S. L. Li *et al.*, “Annealing induced recovery of long-term thermal aging embrittlement in a duplex stainless steel,” *Materials Science and Engineering: A*, vol. 564, pp. 85–91, Mar. 2013.
- [49] Y. Matsukawa *et al.*, “The two-step nucleation of G-phase in ferrite,” *Acta Materialia*, vol. 116, pp. 104–113, Sep. 2016.
- [50] W. Guo, D. A. Garfinkel, J. D. Tucker, D. Haley, G. A. Young, and J. D. Poplawsky, “An atom probe perspective on phase separation and precipitation in duplex stainless steels,” *Nanotechnology*, vol. 27, no. 25, p. 254004, 2016.
- [51] P. D. Southwick and R. W. K. Honeycombe, “Precipitation of M23C6 at austenite/ferrite interfaces in duplex stainless steel,” *Metal Science*, vol. 16, no. 10, pp. 475–482, Oct. 1982.
- [52] J.-Y. Maetz, S. Cazottes, C. Verdu, F. Danoix, and X. Kléber, “Microstructural Evolution in 2101 Lean Duplex Stainless Steel During Low- and Intermediate-Temperature Aging,” *Microscopy and Microanalysis*, vol. 22, no. 2, pp. 463–473, Apr. 2016.
- [53] Y. Chen, B. Alexandreanu, K. Natesan, and A. S. Rao, “Environmentally assisted cracking and irradiation embrittlement of CF-8 and CF-8M cast austenitic stainless steels in high-purity water,” *Nuclear Energy Agency of the OECD (NEA)*, 2015.

- [54] T. A. Hall and A. A. Johnson, "The solidus and liquidus lines in the Au-Ni phase diagram," *Journal of the Less Common Metals*, vol. 141, no. 1, pp. L19–L22, Jul. 1988.
- [55] M. H. Hillert, "A theory of nucleation for solid metallic solutions," Thesis, Massachusetts Institute of Technology, 1956.
- [56] M. Hillert, "A solid-solution model for inhomogeneous systems," *Acta Metallurgica*, vol. 9, no. 6, pp. 525–535, Jun. 1961.
- [57] J. W. Cahn, "On spinodal decomposition," *Acta Metallurgica*, vol. 9, no. 9, pp. 795–801, Sep. 1961.
- [58] J. W. Cahn, "Magnetic Aging of Spinodal Alloys," *Journal of Applied Physics*, vol. 34, no. 12, pp. 3581–3586, Dec. 1963.
- [59] J. W. Cahn and J. E. Hilliard, "Free Energy of a Nonuniform System. I. Interfacial Free Energy," *The Journal of Chemical Physics*, vol. 28, no. 2, pp. 258–267, Feb. 1958.
- [60] D. Chandra and L. H. Schwartz, "Mössbauer effect study of the 475°C decomposition of Fe-Cr," *MT*, vol. 2, no. 2, pp. 511–519.
- [61] K. Chandra, R. Singhal, V. Kain, and V. S. Raja, "Low temperature embrittlement of duplex stainless steel: Correlation between mechanical and electrochemical behavior," *Materials Science and Engineering: A*, vol. 527, no. 16–17, pp. 3904–3912, Jun. 2010.
- [62] I. M. Lifshitz and V. V. Slyozov, "The kinetics of precipitation from supersaturated solid solutions," *Journal of Physics and Chemistry of Solids*, vol. 19, no. 1, pp. 35–50, Apr. 1961.
- [63] "Theorie der Alterung von Niederschlägen durch Umlösen (Ostwald-Reifung) - Wagner - 1961 - Berichte der Bunsengesellschaft für physikalische Chemie - Wiley Online Library." [Online]. Available: <http://onlinelibrary.wiley.com/doi/10.1002/bbpc.19610650704/abstract>. [Accessed: 27-Nov-2017].
- [64] G. Grewal and S. Ankem, "Particle Coarsening Behavior of Alpha-Beta-Titanium Alloys," *Metallurgical Transactions a-Physical Metallurgy and Materials Science*, vol. 21, no. 6, pp. 1645–1654, Jun. 1990.
- [65] G. Grewal and S. Ankem, "Isothermal Particle Growth in 2-Phase Titanium-Alloys," *Metallurgical Transactions a-Physical Metallurgy and Materials Science*, vol. 20, no. 1, pp. 39–54, Jan. 1989.
- [66] A. Vignes, "Diffusion in Binary Solutions. Variation of Diffusion Coefficient with Composition," *Ind. Eng. Chem. Fund.*, vol. 5, no. 2, pp. 189–199, May 1966.
- [67] *TRANSACTIONS OF THE AMERICAN INSTITUTE OF MINING AND METALLURGICAL ENGINEERS VOLUME 128. THE AMERICAN INSTITUTE OF MINING AND METALLURGICAL ENGINEERS*, 1938.
- [68] R. M. Fisher, E. J. Dulis, and K. G. Carroll, "Identification of the precipitate accompanying 885 F embrittlement in chromium steels," *Trans. AIME*, vol. 197, no. 5, pp. 690–695, 1953.
- [69] R. O. Williams and H. W. Paxton, "The nature of aging of binary iron-chromium alloys around 500 C," *J. Iron Steel Inst.*, vol. 185, pp. 358–374, 1957.

- [70] M. Okada, G. Thomas, M. Homma, and H. Kaneko, "Microstructure and magnetic properties of Fe-Cr-Co alloys," *IEEE Transactions on Magnetics*, vol. 14, no. 4, pp. 245–252, Jul. 1978.
- [71] M. K. Miller and J. Bentley, "Characterization of fine-scale microstructures in aged primary coolant pipe steels," 1988.
- [72] M. K. Miller, J. M. Hyde, M. G. Hetherington, A. Cerezo, G. D. W. Smith, and C. M. Elliott, "Spinodal decomposition in Fe-Cr alloys: Experimental study at the atomic level and comparison with computer models—I. Introduction and methodology," *Acta Metallurgica et Materialia*, vol. 43, no. 9, pp. 3385–3401, Sep. 1995.
- [73] M. K. Miller, A. Cerezo, M. G. Hetherington, and J. M. Hyde, "Estimation of composition amplitude: Pa and LBM versus V," *Surface Science*, vol. 266, no. 1, pp. 446–452, Apr. 1992.
- [74] S. S. Brenner, M. K. Miller, and W. A. Soffa, "Spinodal decomposition of iron-32 at.% chromium at 470°C," *Scripta Metallurgica*, vol. 16, no. 7, pp. 831–836, Jul. 1982.
- [75] S. S. Brenner, P. P. Camus, M. K. Miller, and W. A. Soffa, "Phase separation and coarsening in Fe-Cr-Co alloys," *Acta Metallurgica*, vol. 32, no. 8, pp. 1217–1227, Aug. 1984.
- [76] T. Hamaoka, A. Nomoto, K. Nishida, K. Dohi, and N. Soneda, "Accurate determination of the number density of G-phase precipitates in thermally aged duplex stainless steel," *Philosophical Magazine*, vol. 92, no. 22, pp. 2716–2732, Aug. 2012.
- [77] "Innovative manufacturing technology enabling light weighting with steel in commercial vehicles." [Online]. Available: <http://html.rhhz.net/AIM/html/118.htm>. [Accessed: 27-Nov-2017].
- [78] J. E. Brown and G. D. W. Smith, "Atom probe studies of spinodal processes in duplex stainless steels and single- and dual-phase Fe-Cr-Ni alloys," *Surface Science*, vol. 246, no. 1, pp. 285–291, Apr. 1991.
- [79] T. R. Leax, S. S. Brenner, and J. A. Spitznagel, "Atom probe examination of thermally aged CF8M cast stainless steel," *Metallurgical Transactions A*, vol. 23, no. 10, pp. 2725–2736, 1992.
- [80] B. Zhang *et al.*, "Non-uniform phase separation in ferrite of a duplex stainless steel," *Acta Materialia*, vol. 140, no. Supplement C, pp. 388–397, Nov. 2017.
- [81] B. Gault, M. P. Moody, J. M. Cairney, and S. P. Ringer, *Atom Probe Microscopy*, vol. 160. New York, NY: Springer New York, 2012.
- [82] *Local Electrode Atom Probe Tomography - A User's Guide* | David J. Larson | Springer. .
- [83] S. Mburu *et al.*, "Effect of aging temperature on phase decomposition and mechanical properties in cast duplex stainless steels," *Mater. Sci. Eng. A-Struct. Mater. Prop. Microstruct. Process.*, vol. 690, pp. 365–377, Apr. 2017.
- [84] R. P. Kolli and D. N. Seidman, "Comparison of compositional and morphological atom-probe tomography analyses for a multicomponent Fe-Cu steel," *Microscopy and Microanalysis*, vol. 13, no. 4, pp. 272–284, Aug. 2007.

- [85] O. K. Chopra and H. M. Chung, "Effect of Low-Temperature Aging on the Mechanical Properties of Cast Stainless Steels," Argonne National Lab., IL (USA), CONF-871232-2, Jul. 1987.
- [86] W. F. Michaud, P. T. Toben, W. K. Soppet, and O. K. Chopra, *Tensile-property characterization of thermally aged cast stainless steels*. Washington, DC: Division of Engineering, Office of Nuclear Regulatory Research, U.S. Nuclear Regulatory Commission, 1994.
- [87] S. C. Schwarm, R. P. Kolli, E. Aydogan, S. Mburu, and S. Ankem, "Characterization of phase properties and deformation in ferritic-austenitic duplex stainless steels by nanoindentation and finite element method," *Materials Science and Engineering: A*, vol. 680, pp. 359–367, 2017.
- [88] S. C. Schwarm, S. Mburu, R. P. Kolli, D. E. Perea, J. Liu, and S. Ankem, "Mechanical and Microstructural Effects of Thermal Aging on Cast Duplex Stainless Steels by Experiment and Finite Element Method," in *Mechanical and Creep Behavior of Advanced Materials*, I. Charit, Y. T. Zhu, S. A. Maloy, and P. K. Liaw, Eds. Springer International Publishing, 2017, pp. 253–262.
- [89] J. J. Han, C. P. Wang, X. J. Liu, Y. Wang, and Z.-K. Liu, "First-principles calculation of structural, mechanical, magnetic and thermodynamic properties for  $\gamma$ -M 23 C 6 (M = Fe, Cr) compounds," *Journal of Physics: Condensed Matter*, vol. 24, no. 50, p. 505503, 2012.
- [90] J. Zhou, J. Odqvist, M. Thuvander, and P. Hedström, "Quantitative evaluation of spinodal decomposition in Fe-Cr by atom probe tomography and radial distribution function analysis," *Microscopy and Microanalysis*, vol. 19, no. 3, pp. 665–675, Jun. 2013.
- [91] K. H. Lo, C. H. Shek, and J. K. L. Lai, "Recent developments in stainless steels," *Materials Science and Engineering: R: Reports*, vol. 65, no. 4–6, pp. 39–104, May 2009.
- [92] F. Vurpillot, A. Bostel, and D. Blavette, "Trajectory overlaps and local magnification in three-dimensional atom probe," *Applied Physics Letters*, vol. 76, no. 21, pp. 3127–3129, May 2000.
- [93] J. Zhou, "An Atom-Probe Tomography Study of Phase Separation in Fe-Cr Based Steels," 2014.
- [94] J. Zhou *et al.*, "Effect of solution treatment on spinodal decomposition during aging of an Fe-46.5 at.% Cr alloy," *J Mater Sci*, vol. 52, no. 1, pp. 326–335, Jan. 2017.
- [95] *Phase Transformations in Metals and Alloys, Third Edition*, 3 edition. Boca Raton, FL: CRC Press, 2009.
- [96] R. W. Balluffi, S. Allen, and W. C. Carter, *Kinetics of Materials*. John Wiley & Sons, 2005.
- [97] R. P. Kolli and D. N. Seidman, "Co-Precipitated and Collocated Carbides and Cu-Rich Precipitates in a Fe-Cu Steel Characterized by Atom-Probe Tomography," *Microscopy and Microanalysis*, vol. 20, no. 06, pp. 1727–1739, Dec. 2014.
- [98] P. I. Williams and R. G. Faulkner, "Chemical volume diffusion coefficients for stainless steel corrosion studies," *Journal of Materials Science*, vol. 22, no. 10, pp. 3537–3542, Oct. 1987.

- [99] T. Kuwajima, Y. Saito, and Y. Suwa, "Kinetics of phase separation in iron-based ternary alloys. II. Numerical simulation of phase separation in Fe–Cr–X(X=Mo, Cu) ternary alloys," *Intermetallics*, vol. 11, no. 11–12, pp. 1279–1285, 2003.
- [100] Y. S. Yoshihiro Suwa, "Kinetics of Phase Separation in Fe-Cr-Mo Ternary Alloys," *Materials Transactions A*, vol. 43, no. 2, pp. 271–276, 2002.